Alma Mater Studiorum · Università di Bologna

SCUOLA DI SCIENZE
Corso di Laurea Magistrale in Fisica del Sistema Terra

Characterization of atmospheric aerosol absorption properties at different sites in the Po Valley during ACTRIS-2 experiment

Relatore:
Prof. Vincenzo Levizzani
Correlatore:
Dott. Angela Marinoni
Correlatore:
Dott. Angelo Lupi

Presentata da:
Laura Renzi

Sessione I
2019 - 2020

Abstract

Aerosol optical properties are one of the major sources of uncertainty in radiative forcing and cliamate models. During a field campaign performed within ACTRIS-2, optical properties and concentration of absorbing particles have been measured with optical and thermo-optical techniques, at three sites in the Po Valley: Bologna, Monte Cimone and San Pietro Capofiume.

The attenuation values, obtained from two Aethalometers (AE31, AE33) were compared with those of Multi Angle Absorption Photometer (MAAP), to derive the C_0 factor, necessary to convert the attenuation coefficients into absorption. Obtained values ranged between 2.8 and 4.3 in accordance with previous observations and the 3.5 recommended by GAW/WMO.

Comparing equivalent black carbon (BC) and elemental carbon (EC by thermo-optical technique), we derived the mass absorption cross-section (MAC), closely linked with aging and mixing state of the aerosol population. We found a values of 9.2 ± 1.4 m^2/g in San Pietro and 9.4 ± 1.4 m^2/g in Bologna, higher than that considered by default in the instrument.

Among the three sites, the highest concentrations were found in Bologna, the lowest at the mountain site, while intermediate ones at San Pietro. The diurnal variability is in accordance with the location: the urban and rural sites show a close dependence on anthropogenic emissions, while Monte Cimone shows a concentration enhancement during the afternoon, when the boundary layer is higher and the valley breezes can favor the transport of pollution. Low values of single scattering albedo (SSA) in the low sites reflects the influence of freshly generated particles from combustion sources, while the higher values at Monte Cimone indicate that aerosols reaching the mountain site are mixed with non absorbing components and more aged.

A comparison between the Absorption and Scattering Angstrom Exponent reveals that the main absorbing components are BC and BrC for all the three sites, with few episodes of dust transport.

Sommario

Le proprietà ottiche delle particelle di aerosol atmosferico sono una delle maggiori fonti di incertezza tra le forzanti radiative e nei modelli climatici. Durante la campagna di misura ACTRIS-2, abbiamo studiato le proprietà ottiche e le concentrazioni della frazione assorbente con tecniche ottiche e termo-ottiche, in tre siti della Pianura Padana: Bologna, Monte Cimone e San Pietro Capofiume.

I valori misurati da due Aehalometri(AE31, AE33) sono stati confrontati con quelli di un Multi Angle Absorption Photometer (MAAP), per derivare il fattore C_0 necessario a convertire i coefficienti di attenuazione in assorbimento. I valori ottenuti variano tra 2.8 e 4.3 in accordo con precedenti osservazioni e il valore di 3.5 raccomandato da GAW/WMO.

Confrontando il black carbon equivalente (BC) e il carbonio elementare (EC, da tecnica termo-ottica), abbiamo derivato la mass absorption cross section (MAC), prevalentemente influenzata dallo stato di invecchiamento e mescolamento della popolazione di aerosol. A San Pietro abbiamo ottenuto un valore di 9.2 ± 1.4 m^2/g, a Bologna di 9.4 ± 1.4 m^2/g, valori leggermente superiori a quelli impostati per default nello strumento.

Tra i tre siti, le concentrazioni maggiori sono state misurate a Bologna, quelle inferiori nel sito in quota, intermedie in quello rurale in pianura. La variabilità diurna è in accordo con la posizione: i siti urbano e rurale, mostrano una forte dipendenza dalle sorgenti di emissione antropiche, mentre a Monte Cimone le concentrazioni si alzano nel pomeriggio quando lo strato limite è più alto e le brezze di valle favoriscono il trasporto di inquinanti in quota.

Bassi valori di single scattering albedo nei siti di pianura riflettono la forte presenza di particelle emesse da sorgenti di combustione, mentre i valori più alti al Monte Cimone indicano che gli aerosols che raggiungono queste quote sono maggiormente mescolati con componenti non assorbenti e più invecchiati. Un confronto tra Angstrom exponent di assorbimento e scattering rivela che le componenti assorbenti principali sono BC e BrC in tutti e tre i siti, con pochi episodi di trasporto di dust.

Contents

Introduction **10**

1 Aerosols and impacts **11**
- 1.1 Properties of the atmospheric aerosols 12
  - 1.1.1 Aerosol sources and size distribution 12
  - 1.1.2 Formation, evolution and removal from the atmosphere 14
  - 1.1.3 Main constituents 15
- 1.2 Impacts 18
  - 1.2.1 Impacts on climate 18
  - 1.2.2 Impacts on human health 22

2 Black Carbon **25**
- 2.1 Black Carbon definition and properties 25
  - 2.1.1 Formation process 26
  - 2.1.2 Sources 27
  - 2.1.3 Evolution processes, sinks and distribution 29
  - 2.1.4 Optical properties 30
- 2.2 Black Carbon impacts 31
  - 2.2.1 Human health effects 31
  - 2.2.2 Climate effects 31
- 2.3 Techniques for measuring the mass and optical properties of BC 32
  - 2.3.1 Optical techniques 33
  - 2.3.2 Thermo-optical techniques 34
  - 2.3.3 Laser-induced incandescence 34

3 Experimental **35**
- 3.1 Measurement sites 35
  - 3.1.1 Monte Cimone 36
  - 3.1.2 St. Pietro Capofiume 37
  - 3.1.3 Bologna 38
- 3.2 Flexpart lagrangian simulations 39
- 3.3 Instruments 40
  - 3.3.1 Nephelometer (TSI 3563) 40
  - 3.3.2 Multi Angle Absorption Photometer (Thermo Scientific 5012) . . 42
  - 3.3.3 Aethalometer (MAGEE Scientific model AE31) 44
  - 3.3.4 Aethalometer (MAGEE Scientific model AE33) 46
  - 3.3.5 Variability of filter based instruments 47
  - 3.3.6 Thermo-optical analysis 47
- 3.4 Data analysis 49
  - 3.4.1 Absorption and scattering coefficients 49
  - 3.4.2 EC mass concentration (m_{EC}) and MAC derivation 51

4 Results and discussion **53**
4.1 Meteorological characterization 53
4.2 BC mass concentrations 58
4.3 Comparison between attenuation and absorption 61
4.4 Aerosol optical properties 74
4.4.1 Absorption and scattering coefficients in July 2017 74
4.4.2 Diurnal and weekly variations 86
4.5 EC mass concentrations and mass absorption cross section 89
4.6 Absorption and scattering Angstrom exponents 92

5 Conclusions **101**

Bibliography **105**

Introduction

The increasing of gas and particles anthropogenic emissions since the industrial revolution to date have a deep impact on the climate of our planet and on the health of human beings. This has been widely recognized by the scientific community in recent decades with many publications summarized by the Intergovernmental Panel on Climate Change (IPCC) and the World Health Organization (WHO) reports that seek to urge policy makers to act to drastically reduce them.

The aerosols have a relative short lifetime in the atmosphere (days to weeks) and therefore they are subject to great spatial and temporal variability. For that reason their role in climate system is still subject to large uncertainties, especially with regard to the highly absorbing component, mainly due to black carbon (BC). Aerosols affect atmospheric processes in many ways, mainly through absorption and scattering of solar radiation, causing changes in energy balance (cool effect on climate) and atmospheric stability. Moreover, interacting with clouds, aerosol particles impact on precipitation, cloud lifetime, reflectance or albedo and other related phenomena. Despite many years of active research, aerosols are still the least certain of all known climate forcings. This seriously hinders our ability to separate the roles of aerosols and greenhouse gases in driving the past climate change, thereby precluding one from reliably projecting the future climate.

However, a drastic reduction is necessary because of the serious negative effects they have on human health and ecosystems. In particular, it has been recognized that a large fraction of aerosol particles cause reduced lung function and cardiovascular diseases in humans if subject to prolonged exposure. BC is an important element in the search for strategic solutions to both problems, as due to its strongly absorbing properties, a large decrease in the particularly rich sources of this aerosol would probably have positive effects in both directions, reducing the concentration of substances harmful to health and at the same time subtracting a climatic forcer with an heating effect. In particular black carbon fraction of particulate matter (PM), mainly emitted during non-complete combustion, seems to be associated with cardiopulmonary morbidity and mortality (Janssen et al., 2012). BC may not be a major directly toxic component of fine PM but it may operate as a universal carrier of a wide variety of chemicals of varying toxicity.

However, a great deal of research work is still needed to investigate all potential impacts and monitor BC sources and concentrations on different spatial and temporal scales, given its great variability. Measuring its concentrations in the atmosphere is still a challenge today due to the absence of an effective method that can be used as a reference, and its optical properties are also still uncertain due to their variability when pure BC particles mixed internally or externally with other particulate components.

ACTRIS is the European Research Infrastructure for the observation of Aerosol, Clouds and Trace Gases; it is composed of observing stations, exploratory platforms, instrument calibration centers and a data center. One of the objectives of the ACTRIS-2 project (WP11) was the reduction of the uncertainty in the determination of the aerosol light absorption by optimizing the advanced remote sensing and in-situ methods adapted in the frame of the Research Infrastructure. Several specific campaigns were conducted to provide a monitoring of aerosols and their properties in a large number of sites throughout Europe, comparing and harmonizing different measurement techniques. This thesis focuses on the analysis of the aerosol scattering and absorption coefficients and their dependence on wavelength expressed by the absorption and scattering Angstrom exponent, during the month of July 2017 in three different sites of the heavy polluted region of the Po Valley (Bologna, San Pietro Capofiume and Monte Cimone). The locations are reached by different sources of particulate matter: industrial and energy related activities, traffic and other human agricultural and domestic activities in rural areas and large urban centers. In addition, it aims to compare different measurement techniques of the BC and to derive the mass absorption coefficient (MAC) characteristic of the area, during summer.

Chapter one contains a description of the main properties and types of tropospheric aerosols. It describes the various types of sources and the main evolutionary processes to which it is subject in the atmosphere. This Chapter depicts the current knowledge about its interactions with radiation and clouds, and the impact it has on climate and health.

Chapter two goes into more detail on the characteristics of aerosol absorbing fraction and the BC, defining it and listing the main sources and evolutionary processes. It describes its chemical and optical properties and how these may change as a result of aging processes. It summarizes current knowledge on its specific impact on climate and health and describes the techniques most commonly used to measure its mass and absorption coefficient, highlighting the difficulty of harmonizing them and finding an effective technique that can be used as a reference.

Chapter three describes the three measurement sites where the measurements were carried out, with general information on possible sources of pollutants and climatic characteristics. It describes in detail each measurement technique with which the studied data were measured, deepening the sources of uncertainty and describing the way in which they can be harmonized with each other through corrective procedures. It describes how the data was processed before it was analyzed and the uncertainties associated with it.

In *Chapter four* we discussed results from the analysis of field campaign data, together with the conclusions that can be drawn on the sites considered. First of all the global weather situation of the sites in July 2017, from data of weather stations and general synoptic situation is described. Then BC mass concentration and absorption coefficient values measured by MAAP and Aethalometers (models AE31 and AE33) are compared with each other in order to obtain correction factors for Aethalometers, compared to the results of other ACTRIS campaigns and WMO/GAW recommendations. Elemental carbon (EC) mass concentrations measured by a thermal-optical analysis are presented and used together with MAAP absorption coefficients for MAC derivation at 637 nm for all sites. In the end a description of the variability of absorption and scattering coefficients and absorption and scattering Angstrom exponent on different time scales in all the three sites, are presented, also in relation to the backtrajectories obtained from the FLEXPART transport model.

Chapter 1

Aerosols and impacts

An aerosol is defined as a suspension of liquid or solid particles in a volume of gas (Seinfeld and Pandis, 2006). Although this atmospheric particles, also named with the acronym PM (particulate matter), represent a minority component of the atmospheric constituent's mass, they have a significant role in the climate and biogeochemical systems, influencing phenomena that have an impact on well-being of humans and ecosystems.

They can interact with radiation, act as cloud condensation (CCN) and ice (IN) nuclei, changing cloud formation, lifetime and precipitation rate and also offer a surface for heterogeneous reactions, such as condensation and evaporation of semi-volatile vapours from their surface or other reactions with trace gases. Through these processes they alter visibility, affect climate change directly and indirectly, acidify rainfall and cause ozone depletion. The finest particles can affect human health penetrating deep into the lungs and causing or aggravating pulmonary and cardiovascular diseases. In addiction the dry and wet deposition of some of them on lakes, rivers, grasslands, farmlands and forests, can cause both beneficial and extremely harmful effects depending on the characteristics of the environment and their composition.

They already had a significant role during the pre-industrial era but over the anthropocene have undergone great changes as a result of human activities such as industrial and energy production, transportation's emissions and land-use management. Although the importance of these particles has long been known, research on this subject has developed mainly since the last decades of the 90s, after the definition of their role in atmospheric phenomena that pose a risk to ecosystems and human health, such as acid rain, ozone depletion and photochemical smog.

Although much progress has been made in recent years, knowledge of the impact of aerosols on the atmosphere remains limited compared to that of the gaseous component. The main sources of uncertainty in their characterization, derives from the inability to separate the different chemical components that tend to mix in the atmosphere. The current efforts in the study of aerosols are therefore largely concentrated in an attempt to develop measurement methods and models, capable of quantifying and effectively representing the properties and effects of individual components.

This chapter summarizes the present knowledge on aerosol's properties and their interactions in the atmosphere. The main references used are: The Physical Science Basis of IPCC reports (2007, 2013), the book "ATMOSPHERIC CHEMISTRY AND PHYSICS, From Air Pollution to Climate Change" (Seinfeld and Pandis, 2006), Mahowald et al. (2011), WHO (2016), Shiraiwa et al. (2017).

1.1 Properties of the atmospheric aerosols

1.1.1 Aerosol sources and size distribution

Aerosols have different origins, characteristics and lifetime in the atmosphere which determine their different role within the atmospheric processes. They can be classified in different ways based on the type of source, the formation mechanism and the size. Figure 1.1 shows main sources ad processes for the most abundant species in the atmosphere.

Aerosols can derive from both anthropogenic and natural sources. Anthropogenic sources are fuel combustion, industrial processes, nonindustrial fugitive sources (roadway dust from paved and unpaved roads, wind erosion of cropland, construction, etc.), and transportation sources; natural ones include soil and rock debris, volcanic action, sea spray, biomass burning and reactions between natural gaseous emissions.

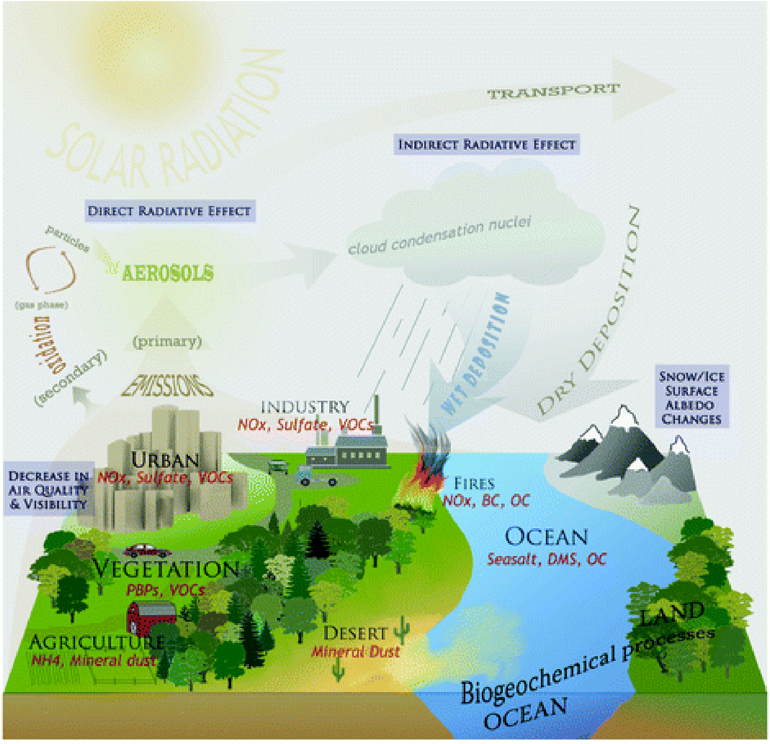

Figure 1.1: Composition diagram showing the evolution/cycles of various elements in Earth's atmosphere (Mahowald et al., 2011).

They can originate from two different pathways: primary particles are directly emitted into the atmosphere by combustion sources (e.g., coal combustion, biomass burning, and vehicle emissions) or other wind-driven processes such as the resuspension of dust and sea salt; secondary particles are instead formed when vapors nucleate into stable molecular clusters, which can grow rapidly to produce nanometre-sized particles. They typically come from photochemical reactions of gas-phase species that are emitted directly into the atmosphere. Primary emissions, apart those from aircraft, occur typically near the ground, while secondary particles can be created everywhere in the atmosphere, both high near a cloud or even at the top of the troposphere, and near the ground surface.

Aerosols can vary in size from few nanometers to tens of micrometers depending on the source and the production mechanism. Their size variability is usually described mathematically using the mass (n_M), volume (n_V), surface (n_S) and number (n_N) distributions. These functions of the diameter are defined as the fraction of mass, volume, surface or number of particles that have a diameter raging from D_p to $(D_p + dD_p)$ in one cm^3 of air. Integrating them on all the possible diameters, the total mass, volume, surface and number of particles in one cm^3 are achieved. The aerosol population presents generally log-normal distributions of the form:

$$n_N(D) = \sum \frac{1}{\sqrt{2\pi} D \ln \sigma_g} exp[-\frac{\ln(D/\tilde{D})^2}{2 \ln^2 \sigma_g}], \tag{1.1}$$

where σ_g is the geometric standard deviation and $\tilde{D}$ the geometric mean, characterized by distinct modes. The mass and volume distributions are dominated by: the accumulation mode (0.1 μm < D$_p$ < 1 μm) and the coarse mode (D$_p$ > 1 μm). The accumulation mode derives from primary emission processes, condensation from the gas phase and coagulation of smaller particles. In some cases it can consists of two overlapping submodes: the condensation submode, which is the result of primary particle emission and growth of smaller particles by coagulation and water vapor condensation; and the droplet submode that is created when accumulation mode particles are processed in clouds.

The coarse mode is composed of particles transported in atmosphere by mechanical processes such as wind or erosion. Most of the material is primary but there are also secondary sulfates and nitrates.

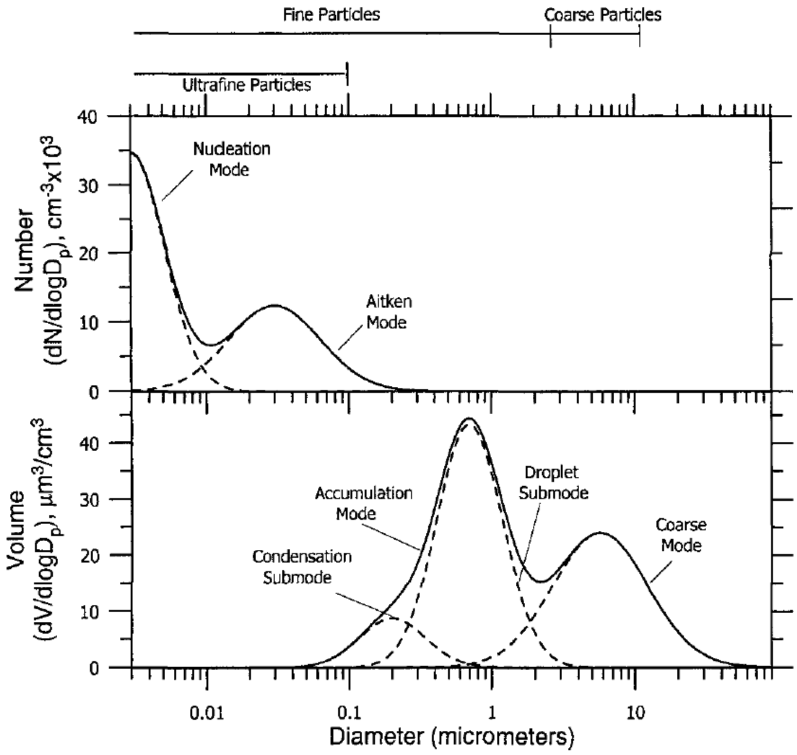

Figure 1.2: Typical number and volume distribution of atmospheric particles (John Seinfeld and Spyros Pandis, 2006).

Even if the particles of these two mass distribution modes contributes to almost all the aerosols mass, they are negligible in number with respect to the particles with diameters smaller than 0.1 μm. The number distribution is in fact dominated by two modes: the Nucleation mode (particles smaller than 0.01 μm) and the Aitken nucleus mode (particles with diameters between 0.01 μm and 0.1 μm). The first is composed of particles created in-situ from the gas phase by nucleation and has negligible mass; the second is the result of condensation of secondary material on primary particles and constitutes the accumulation mode of mass distribution.

Particles with diameters larger than 1 μm are operationally identified as coarse particles while those with diameters less than 1 μm are called fine particles. The fine-particle category typically includes most of the total number of particles and a large fraction of the mass. Fine particles with diameters smaller than 0.1 μm are often called ultrafine particles.

1.1.2 Formation, evolution and removal from the atmosphere

Aerosol's impact on climate and ecosystems is related to their chemical composition, mixing state with other components, size and morphology. These properties are determined and modified after emission by a complex interplay between their sources, atmospheric transformation processes and their removal from the atmosphere.

As we have seen aerosols can be produced through primary emission or secondary formation process. The latter is known as nucleation and can be divided in two types: homogeneous nucleation occurs when molecules of the same type aggregates through collisions to form a solid particle; heterogeneous nucleation, which is the most common, occurs when molecules in the gas phase aggregates on a preexisting surface.

Once emitted aerosols can remain in the atmosphere for hours or days depending on meteorological conditions and properties affecting their removal. During this time they move from sources, transported by local currents, and undergo changes in their size, mass, morphology and composition, that in turn affect other properties such as hygroscopicity and ability to interact with radiation of different wavelengths. The main processes acting on them are coagulation, condensation, photochemical and heterogeneous reactions on their surface. Coagulation occur after collisions through Brownian processes, if particles stick to each other forming larger ones, with different composition. It contributes to aerosol internal mixing, increases the mass of particles while depleting smaller ones. Condensation is instead the process by which vapours of different compositions such as H_2SO_4, organics, HNO_3 , and NH_3, condense on pre-existing particles increasing their sizes and transferring material from the gas phase. During their lifetime aerosols can also diminishing in number or mass if part of the material returns to the gas-phase.

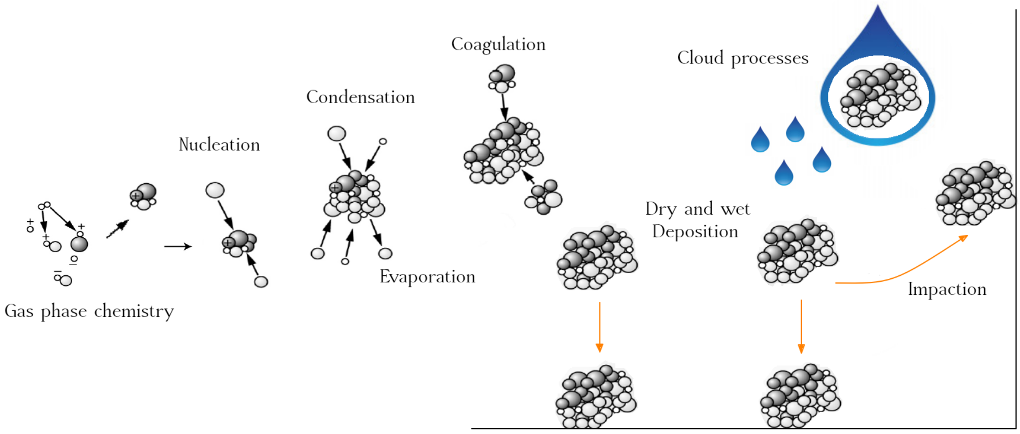

Figure 1.3: Schematic representation of aerosol processes in the atmosphere.

Depending on relative humidity of the environment and particles composition, water vapour can condense on their surface leading to an increase in mass, and possibly, in supersaturation condition, to cloud droplets formation. The mass can also decrease if they dry out as a result of a decrease in humidity conditions. Inside the clouds they undergo further changes, and then be released after evaporation. Cloud processing affects the number concentration, composition, size and mixing state of aerosol particles in different manner: via aqueous-phase chemistry taking place inside them, altering aerosol precursor chemistry around and below clouds, and via different aerosol-hydrometeor interaction.

Typically aerosols are transported over long distances by the atmospheric circulation as the above described physicochemical processes occur. At an average wind speed of a few meters per second, they can travel a few hundred kilometers horizontally, and several kilometers vertically, in a period of one day. Particles are in the end removed from the atmosphere following two main path: wet and dry deposition.

Dry deposition is the transport of particulate species from the atmosphere onto surfaces, in the absence of precipitation. It is influenced by particles properties such as size, density, shape, composition and by the nature of the surface. Small particles (0.001-0.1 μm) are mainly removed by coagulation processes: few small particles stick together to form a new particle with a larger diameter. Moreover, the brownian diffusion is very efficient for these particle sizes and allows both dry and wet deposition. Particles in the range (0.1 - 5 μm) usually have the longest life-time in atmosphere: they are too large for brownian diffusion and too small for gravitational settling. They are mainly removed by rain out (in-cloud removal) or wash out (particles are intercepted by rain drops and are consequently removed), big particles ($>$ 5 μm) are mainly removed by gravitational settling.

Wet deposition is than the process by which a particle is transported on the surface by precipitation. It involves first the transformation of the particle to a new hydrometeor by condensation of water, droplet formation or its collision and capture by a pre-existing one, and then its delivery to the earth's surface. Both processes take place inside a cloud, while raindrops collect and remove particles below a raining cloud. For particles with diameters in the range between 0.5-2.5 μm the most effective way for incorporation in clouds and rain droplet is to be involved in droplet nucleation during cloud formation stage. This depends on their chemical composition and hygroscopicity. Larger particles are collected and removed by rain droplets both in and below the cloud.

1.1.3 Main constituents

The main constituents of atmospheric aerosol are inorganic species such as sulphate, nitrate, ammonium, sea salt; organic species (OA), which can be divided in primary (POA) and secondary (SOA) ; Black Carbon (BC); mineral species including desert dust; primary biological aerosol particles (PBAPs) such as pollen, spores, bacteria, plant and animal fragments.

Sulphate can be primary emitted or derive from oxidation of SO_2 and other S gases from natural and anthropogenic sources. They can vary in size spanning all the four modes of the size distributions, from nucleation to coarse mode. The main natural sources are volcanic eruptions, that can emit it directly in the stratosphere, and dimethyl sulfide (DMS) produced by phytoplankton in the ocean which is oxidized to SO_2, then converted in aerosol particles after other reactions and nucleation (Andreae and Crutzen, 1997). Athropogenic sources are linked with power production or industrial processes in which SO_2 is emitted as a by-product of the burning of fossil fuels contaminated with sulfur compounds.
Nitrogen is present in two main forms nitrates and ammonium both derived by secondary processes from NO_x or NH_3 emissions respectively. Anthropogenic sources are combustion of fuel, such as hydrocarbon, for example in car engine or industrial processes. But they can also come from soils, where NO_x is generated by bacterial activity and its concentration is regulated by soil conditions, application mode and rate of artificial fertilizer (Bouwman, Boumans and Batjes, 2002; Bouwman et al., 1997). The nitrogen loss is dependent on the type of fertilizer, properties of the soil, meteorological conditions, and agricultural management practices (Adams, Seinfeld and Koch, 1999). These compounds span a broad diameter range from nucleation to coarse particle mode.

Mineral dust, sea spray and PBAPs are predominantly of natural origin and are introduced in the atmosphere as primary particles. Mineral dust is the most abundant aerosol species in the atmosphere and is composed of particles created by disintegration and erosion of aggregates, than transported over long distances from region with little vegetation cover, dry soil and strong winds. Africa dominates its emission providing about the 50 % of global dust (Tegen and Fung, 1994). It typically presents large diameters, with size distribution dominated by coarse and super-coarse modes and a small accumulation mode. It shows concentration very sensitive to climate shifts and regional changes. Human activities can affect its sources by land use (road dust) or fertilizing terrestrial plants. Recent estimates from paleoclimate observations and modeling suggest a doubling of dust over the twentieth century but more studies are required.

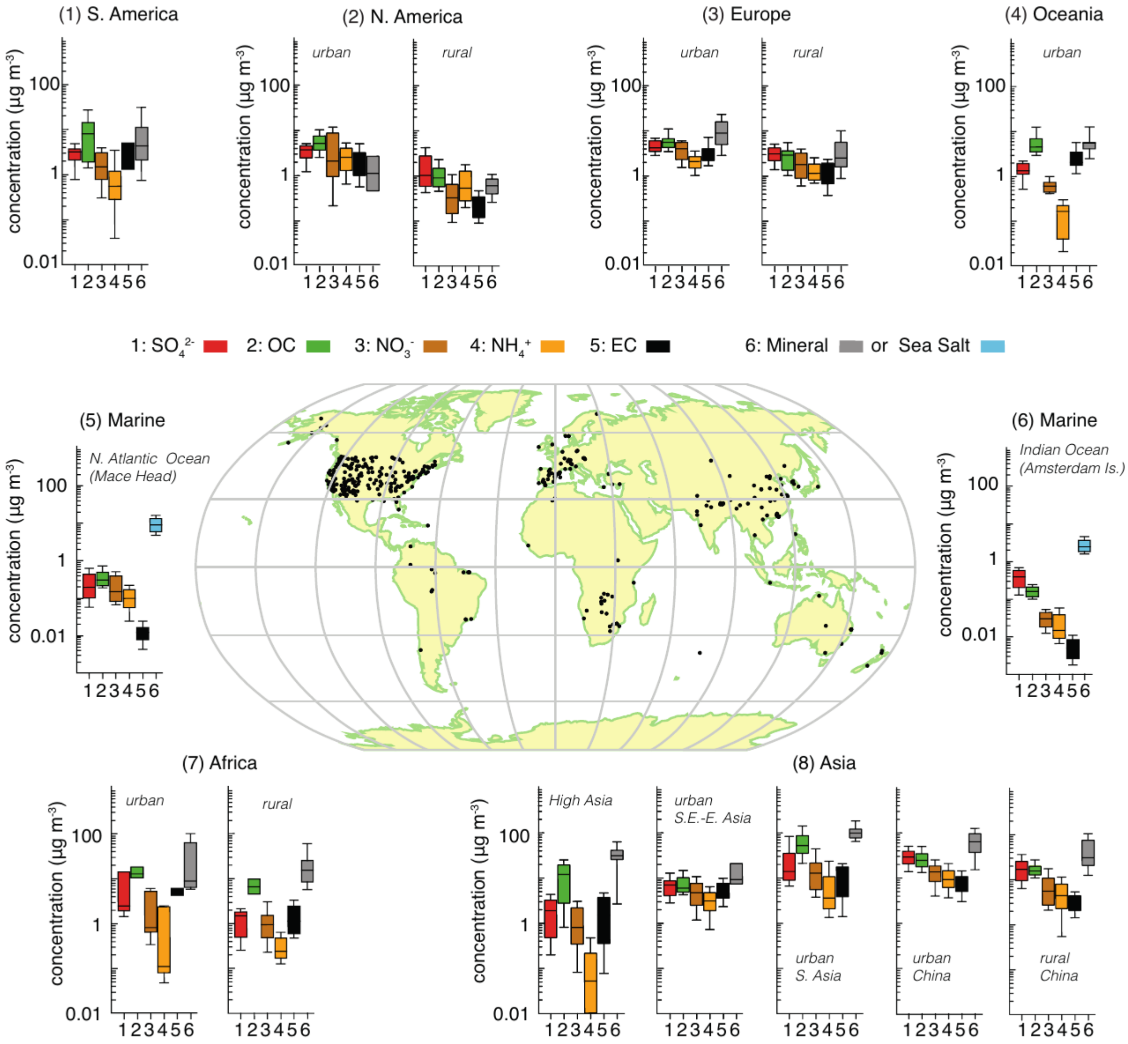

Figure 1.4: Concentration in mass of the main aerosol species in many regions of the world (IPCC report, 2013).

See spray refers to the combination of organic and inorganic species emitted by the ocean through mechanical processes due to the wind stress or thermal instabilities at the surface. It presents large variability in size modes with diameters spanning a range from 20 nm up to 100 μm, with a greater number of super-micrometer particles relative to other species. Mass and number emission flux depends on wind speed, temperature of the ocean surface and atmospheric stability. Although aerosols in marine air masses are typically lower in number compared to that of continental air masses, they tend to have greater total mass and volume. The main inorganic specie, that is also the largest one, is sodium chloride or sea salt, but you can find a wide variety of compounds. Organic species are produced by biological activity and together with phosphorus emissions are related to phytoplankton concentration in the ocean surface layer. There are still large uncertainties about see spray concentration and composition. Some measurements (references in aerosol impacts on climate) suggest a sea spray aerosol distribution in which the smaller particles (with diameter $< 0.5\ \mu$m) consisted mainly of organic matter, and the large (especially super-micrometer) particles were almost entirely sea salt. The latter is one of the most important natural aerosols affecting directly and indirectly radiative transfer, thus all these uncertainties are important to resolve.

Organic aerosols (OA) are a complex mixture of chemical compounds containing carbon-carbon bonds which constitutes a large fraction of the sub-micrometer particulate mass, up to 90% in some areas. They can be emitted as primary aerosol particles (POA) or formed as secondary aerosol particles (SOA). The main sources of POA particles are: natural and anthropogenic biomass burning (forest fires, slashing and burning, domestic heating), fossil-fuel combustion (domestic, industrial, traffic), and wind-driven or traffic-related suspension of soil, road dust, biological materials (plant and animal debris, microorganisms, pollen, spores, etc.) also known as PBAPs, sea spray, and spray from other surface waters with dissolved organic compounds. SOA components are formed by chemical reaction and gas-to-particle conversion of volatile organic compounds (VOCs). Formation of VOCs from the gas phase can be both natural and anthropogenic. The main natural compounds are isoprene, monoterpenes and sesquiterpenes while the main anthropogenic are aromatics, alkanes and alkenes. The SOA formation can then be due to nucleation and growth of aerosol particles, adsorption and absorption of VOCs by preexisting aerosols or cloud particles, heterogeneous and multi-phase chemical reaction of VOCs or semi-volatile organic compounds (SVOC), at the surface or in the bulk of aerosol or cloud particles. There are still many uncertainties in emission and processes involving POA and SOA, which reflects in a lack of knowledge about their concentration and role in the climate system.

BC is then a distinct type of carbonaceous material, formed from the incomplete combustion of fossil fuel and biomass based fuels under particular conditions. Freshly emitted particles have diameters < 100 nm but after aging processes they grow and reach typical dimension of accumulation mode. This aerosol is the main component measured in this thesis, so it will be described in more details in the next chapter.

Each species, depending on properties affecting its lifetime and environmental conditions including location of main sources, experiences a great variability both in the vertical and horizontal direction, and also in time on different scales. Aerosols can be transported over long distances or be removed in a brief time after emission, depending on their sizes and interaction with other substances or water vapour and cloud droplets. The modeling of this variability in climate models for each species individually is one of the main sources of uncertainties in the evaluation of their impacts both on local and global scale. It is thus important to improve the quality of models and resolution of measurements both remotely and on site. The data and models available to date provide the results shown in the figure 1.4 on the spatial distribution of the main components all over the world.

Mineral dust is the most abundant species over most continental regions, reaching 35% of the total mass concentration in Southern Asia and China. Organic Carbon is dominant in the urban North and South America where it cover the 20% of the total, while it is less abundant in other regions of the world with a mean of 16%. Sulphate normally vary between 10 and 30 % except in rural Africa and urban Oceania where it is less abundant than 10%. The mass fraction of nitrate and ammonium are around 6% and 4% respectively. The mass concentration of EC depends on the presence of combustion sources. It represent about the 5% of the total mass in many regions but it can reach 12% in South America, urban Africa, urban Europe, South Asia and urban Oceania. Sea salt is negligible in all continental regions but is dominant in oceanic remote sites where it represents the 50 - 70 % of the total mass concentration (IPCC report, 2013).

1.2 Impacts

Among all the aerosol's impacts on the Earth system we now deepen their influence on climate and human health, which are the driving reason for the analysis provided in this thesis, deriving parameters useful to evaluate the aerosol-radiation interaction and the information required to pick up epidemiological studies. The main information reported in this chapter come from IPCC reports (2013, 2007) and from the World Health Organization (2016).

1.2.1 Impacts on climate

Aerosols, such as greenhouse gases, can be defined as *forcing agents*, which are elements of the climate system with the ability to influence the global mean surface temperature by acting on the Earth's energy balance. This action can be direct or driven by *rapid adjustaments*, which are all those phenomena through which a forcing agent influences other components of the climate system, thus altering the global balance indirectly. In the case of aerosols the known adjustments are: regional temperature variation and atmospheric stability, changes in vapour content and clouds, various effects on the biosphere. These adjustments are generally very quick and do not operate through changes in surface temperature, that are slowed by the ocean's heat capacity. The effect on climate of forcing agents can then be amplified or decreased through *feedback mechanisms* or changes in climatic variables mediated by a variation in the global mean surface temperature which impact on radiative budget.

Currently, the climate effects of aerosols are divided by the IPCC report (2013), into two large macro-areas containing both direct radiation effects and rapid adjustments. One set concerns all those changes that are generated by the interaction of aerosols with radiation, whose global impact on climate is defined Effective Radiative Forcing from aerosol-radiation interaction (ERFari). The other are those generated by the interaction of aerosols with clouds, defined as Effective Radiative Forcing from aerosol-cloud interaction (ERFaci). Both these components of the change are in turn divided into Radiative Forcing and adjustments as in figure 1.5.

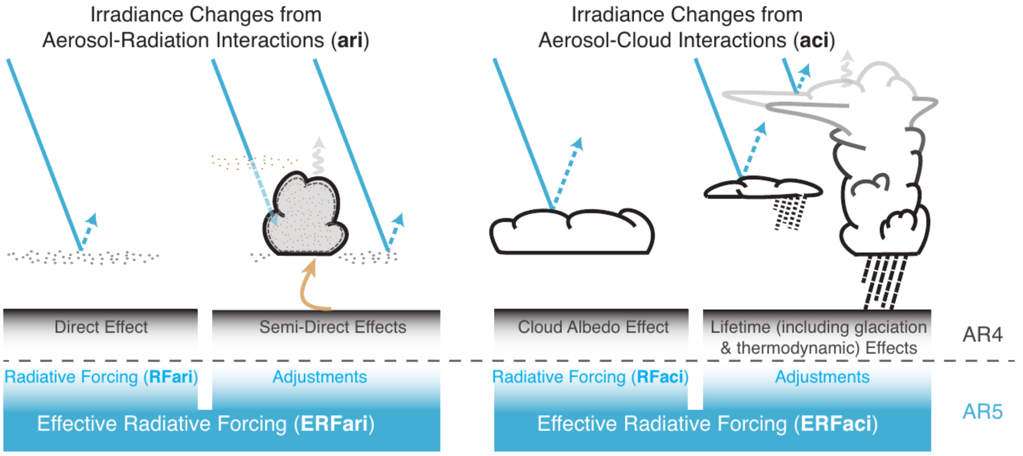

Figure 1.5: Schematic of the new terminology used in fifth Assessment Report (AR5) for aerosol–radiation and aerosol–cloud interactions and how they relate to the terminology used in AR4. The blue arrows depict solar radiation, the grey arrows terrestrial radiation and the brown arrow symbolizes the importance of couplings between the surface and the cloud layer for rapid adjustments (IPCC report, 2013).

In the following paragraphs, the mechanisms of interaction with radiation and clouds will be explored and the main sources of uncertainty in providing accurate estimates of these effects will be identified.

Aerosol-Radiation interaction

When an aerosol particle interact with radiation, its charges are excited and can then re-emit the energy in all direction (scattering) or convert it into other forms such as heat (absorption). The ability of a given particle to scatter and absorb radiation depends on its composition, mixing state, size and shape, and varies in relation to the wavelength of incident radiation.

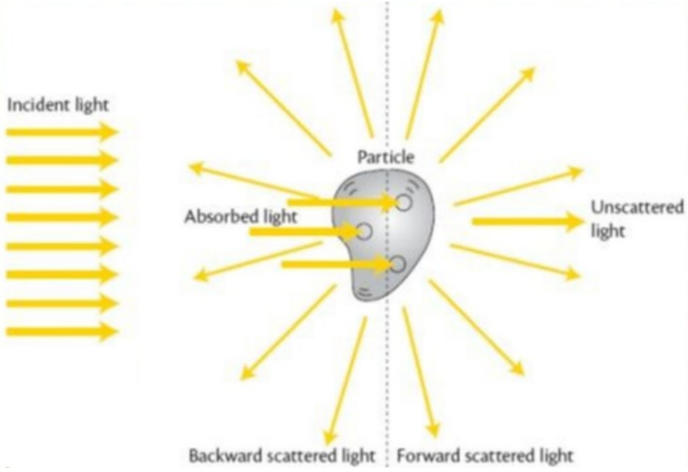

Figure 1.6: Schematic representation of scattering and absorption by a single particle.

All atmospheric aerosols can scatter solar radiation while only a small fraction of them, such as BC, mineral dust and some OC can absorb it. To a lesser extent they are also able to interact with terrestrial radiation through scattering, absorption and emission. Absorbing component of aerosols warms the atmosphere, while the scattering component cools it. However, the overall effect on the energy budget also depends on the surface characteristics and the cloud cover. To quantify the effect of each chemical species on the energy balance it is therefore necessary to provide an estimate of these two effects.

A complete mathematical treatment of the relation between particle properties and electromagnetic field has been developed by the Mie theory in Bohren and Huffman (1983), which provide some information on scattered and absorbed radiation for any types of particles and a complete solution to the problem for a single spherical particle. The most useful outcomes and parameters developed in this theory are summarized below.

If we consider a single particle which interacts with a beam af intensity I_0 the intensities of energy scattered and absorbed by it are respectively:

$$I_{sca} = C_{sca} F_0 \qquad I_{abs} = C_{abs} F_0; \tag{1.2}$$

where C_{sca} and C_{abs} in units of m^2, are the single particle scattering and absorption cross sections, which provide a measure of the particle's ability to attenuate the light beam that hits it, by scattering and absorption respectively. The combined effect is referred to as extinction and for the conservation of energy, it must be equal to the intensity removed from the incident beam. An extinction cross section can be defined as:

$$C_{ext} = C_{sca} + C_{abs}, \tag{1.3}$$

and dividing it for the cross sectional area A, the dimensionless extinction efficiency is obtained:

$$Q_{ext} = Q_{sca} + Q_{abs}. \tag{1.4}$$

Mie theory provides some equations which relate Q_{sca} and Q_{abs} to some key parameters, for a spherical particle: the wavelength of the incident radiation λ, the size of the particle usually expressed as $\alpha = \frac{\pi D_p}{\lambda}$, the particle complex refractive index normalized by that of medium $m = n + ik$.

When the particles are more than one, as is the case in the atmosphere, if the average distance between them is large compared to their sizes, it can be assumed that the total scattered intensity is the sum of those scattered by individual particles. This assumption is easily obeyed in the atmosphere. In this situation the fractional reduction in intensity produced by a layer of particles of depth dz is expressed by the Lambert Beer law:

$$dF = -b_{ext} F(z) dz \tag{1.5}$$

where b_{ext} is defined as extinction coefficient and for a population of mono-disperse particles, with number concentration N, is related to the extinction efficiency by:

$$b_{ext} = N \cdot Q_{ext} \cdot \frac{\pi D_p^2}{4}, \tag{1.6}$$

while for a population of different particles, with a mass distribution function $n_M(D_p)$ and mean refractive index m, is given by:

$$b_{ext}(\lambda) = \int_0^{D_p^{max}} \frac{3}{2\rho D_p} Q_{ext}(m, \alpha) n_M(D_p) dD_p, \tag{1.7}$$

that can be divided into scattering and absorption component:

$$b_{ext} = b_{abs} + b_{sca}. \tag{1.8}$$

All these coefficients depends on the radiation wavelength. This dependence is described by the Angstrom formula:

$$\frac{b_{ext}(\lambda)}{b_{ext}(\lambda_0)} = (\frac{\lambda}{\lambda_0})^{-EAE}, \tag{1.9}$$

where EAE is defined as Extinction Angstrom exponent. The Angstrom exponents describing the dependence of scattering and absorption coefficients known as Scattering Angstrom exponent (SAE) and Absorption Angstrom exponent (AAE) are useful parameters in inferring aerosol properties from optical measurement. The AAE is related to the particle's colour and can therefore be used to distinguish between the three main absorbing components (BC, dust and OA). Several studies (Rosen et al., 1978; Bergstrom et al., 2002, 2007; Kirchstetter et al., 2004; Clarke et al., 2007) confirm values very close to the unit for BC, which can vary between 1.9 and 0.8 when coated (Lack and Cappa, 2010). Observed OA AAE range from 3.5 to 7 (e.g., Kirchstetter et al., 2004; Sun et al., 2007; Lewis et al., 2008; Yang et al., 2009), while that of dust is typically about 2 to 3 but can be higher for very red dust (e.g. Alfaro et al., 2004; Bergstrom et al., 2007). On the other end, SAE depends primary on the dominant size mode in a mixture of aerosols, with larger numbers associated with smallest particles of the fine mode and lower ones suggesting the dominance of larger particles.

Another important parameter in the definition of optical properties of an aerosol is the single scattering albedo (SSA) which is the ratio between scattering and extinction coefficients:

$$SSA(\lambda) = \frac{b_{sca}(\lambda)}{b_{ext}(\lambda)}, \tag{1.10}$$

and describes the dominance of one effect on the other. Values near unity indicate that the aerosol is mainly scattering, while values below 0.8 indicate that the particles could have a net warming effect (Haywood and Shine, 1995). The value that divides warming from cooling also depends on the albedo of the underlying surface or clouds and the fraction of light that is scattered upward by the particles (Chylek and Wong, 1995).

Knowledge of the impact of an aerosol species on climate change therefore depends on the ability to quantify the scattering and absorption coefficients and the single scattering albedo or to determine the properties from which they can be derived through some mathematical model such as the Mie theory. These coefficients depends on the aerosol size distribution, aerosol refractive index and mixing state and are also subject to further influences due to humidification through changes in particle shape, size and refractive index.

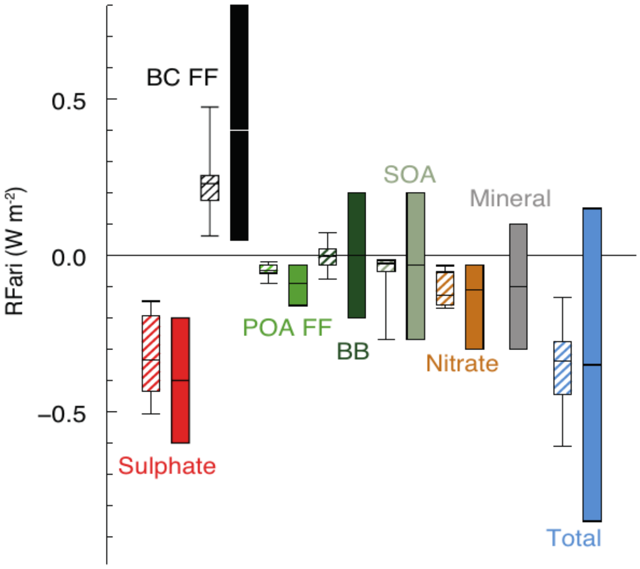

Figure 1.7: Annual mean top of the atmosphere radiative forcing due to aerosol– radiation interactions (RFari, in W m–2) due to different anthropogenic aerosol types, for the 1750–2010 period. Hatched whisker boxes show median (line), 5th to 95th percentile ranges (box) and min/max values (whiskers) from AeroCom II models (Myhre et al., 2013) corrected for the 1750–2010 period. Solid coloured boxes show the AR5 best estimates and 90% uncertainty ranges. BC FF is for black carbon from fossil fuel and biofuel, POA FF is for primary organic aerosol from fossil fuel and biofuel, BB is for biomass burning aerosols and SOA is for secondary organic aerosols (IPCC report, 2013).

The current estimate of the overall radiative effect of aerosols is that of Forster et al. (2007) and is given as –0.5 ± 0.4 W m^{-2}, with a low level of scientific understanding. The main sources of uncertainties are related to the absorbing component, largely consisting of BC. The values estimated for every single component is reported in figure 1.7 even if reading these estimates it must be remembered that, due to aerosol mixing, it is not easy to isolate the impact of individual components. The total value may therefore not necessarily be the sum of the others. Moreover, these estimates concern the global effect of the aerosol but because of their great spatial variability, the individual species can heavily influence the local climate even if they have a very small effect on the global one. In addiction to the direct effect just described, absorbing aerosols also have the potential to indirectly modify clouds properties. This can happen in two ways: heating the air surrounding them, while reducing the amount of solar radiation reaching the ground, that result in a stabilization of the atmosphere and diminishing of the convection and thus of the potential for cloud formation; increasing the atmospheric temperature, which reduces the relative humidity, inhibiting cloud formation, and enhancing evaporation of existing clouds. All these processes are collectively termed as semi-direct aerosol effect (Hansen, Sato and Ruedy, 1997). Quantification of this effect is uncertain and highly depends on the vertical profile of the absorbing component (Koch and Del Genio, 2010).

BC and other absorbing aerosols deposited on snow or ice surfaces may also reduce the surface albedo, leading to reduced reflectance of solar radiation, and hence an heating effect (Hansen and Nazarenko, 2004).

Aerosol-cloud interaction

The other mechanisms by which atmospheric aerosols influence the climate, derive from their ability to act as cloud (CCN) and ice (IN) condensation nuclei. A significant change in their concentration can indeed affects the formation and evolution of clouds, as well as their ability to produce precipitation.

The ability of an aerosol to act as cloud condensation nuclei at a certain supersaturation is related to its size and composition. It is usually quantified by the bulk hygroscopicity parameter k (Rissler et al., 2004; Petters and Kreidenweis, 2007) or by the theory of adsorption for insoluble particles. The ability of inorganics is relatively well understood, between which the most effective are sea salt, sulphates and sulphuric acid, nitrates and nitric acid, while that of organic and organic-inorganic mixtures needs to be further investigated.

There are four ways reported in the literature in which heterogeneous ice-nucleation can occur: freezing of prexisting droplets, freezing during drop formation, freezing by contact with an IN and nucleation due to direct deposition of vapour on an IN. Aerosols that are known to act as IN are: mineral dust, volcanic ash and primary bioaerosols such as bacteria, fungal spores and pollen. While conflicting evidence has been presented for the ability of BC, organic and biomass burning particles.

The main effect of a significant increase in the number of CCNs, recognised by several studies summarized in the IPCC report (2007), is to generate more but smaller cloud droplets for fixed liquid water content. The non-linear relationship derived in Feingold and Graham (2003) between the concentrations in number of aerosols and raindrops is as follows:

$$N_d \approx (N_a)^b \tag{1.11}$$

Where b can vary widely, with values ranging from 0.06 to 0.48 (low values of b correspond to low hygroscopicity), because of the great sensitivity to the characteristics of the aerosol.

This increase in the number of drops has the main consequence of increasing the albedo of the cloud, which produces a greater reflection of the radiation and therefore a cooling of the atmosphere. This effect called cloud albedo effect (Twomey, 1977), is referred to as Radiation forcing from aerosol-cloud interaction (RFaci) in the IPCC report (2013). Quantification for this is –0.9 ± 0.5 $\mathrm{Wm}^{-}2$ (Forster et al., 2007), with a very low level of scientific understanding.

Smaller droplets require also longer growth times to reach sizes at which they easily fall as precipitation. This effect can influences the lifetime of the cloud and therefore its interaction with radiation. However, the life cycles of clouds are controlled by a number of different factors including meteorology and aerosol-cloud microphysics, so this other processes related to aerosol-cloud interactions remain highly uncertain. Interactions between aerosols and clouds are therefore one of the major sources of uncertainty in quantifying the impact of aerosols on climate.

1.2.2 Impacts on human health

Air pollution, both in urban and rural areas, is recognized by the World Health Organization as a major environmental health problem, affecting the population of the whole world. The most recent estimates (Cohen et al. 2017; Lelieveld, 2015), attribute to air pollution about 4.3 million of premature deaths per year, of which 4.04 million due to $\mathrm{PM}_{2.5}$ (particulate matter with diameter lower than 2.5 μm). The uncertainty on this estimate is ± 25 % (95 % confidence interval).

This mortality, however, is not equally distributed throughout the globe; people who live in low and middle income countries disproportionately experience the burden of pollution with 91 % of premature deaths occurring there, in particular in South-East Asia and Western Pacific regions. The 70 % occurs in Asia, and more than 50 % in

China and India alone. Although the majority of deaths occur in these countries, per capita mortality is higher in Eastern Europe, as can be seen in the figure 1.8.

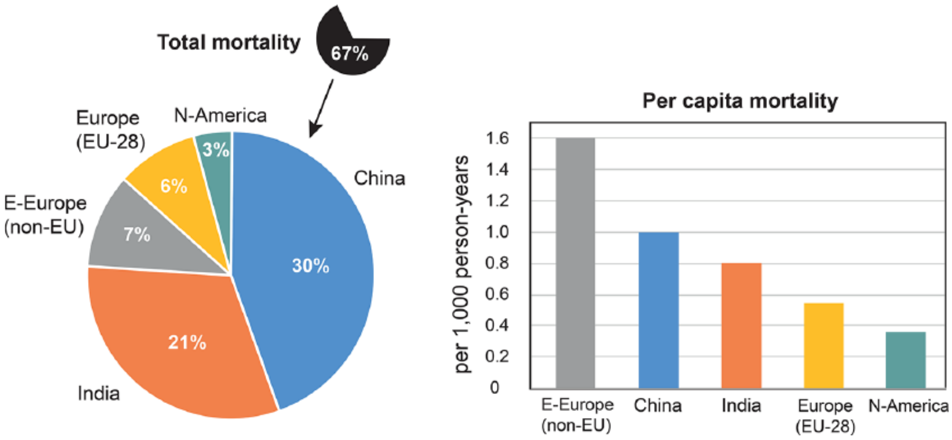

Figure 1.8: About two-thirds of the global mortality attributable to air pollution of 4.3 million/year occur in China, India, Europe and N-America (left). Though China and India lead in terms of total mortality, the per capita mortality is highest in Eastern Europe (right) (Shiraiwa et al., 2017).

To better understand the impact of pollution on health, be aware that the 4.3 million per year are nearly 4 times the annual number by HIV/AIDS and about 15 times the number of deaths through violence. According to the Global Burden of Disease Study 2016 GBD (2016), particulate air pollution is among the seven largest health risk factors, together with high blood pressure, tobacco smoking, diabetes, childhood undernutrition, high body mass index and high cholesterol.

The pollutants most related to health effects are ozone (O_3), sulphur dioxide (SO_2), nitrogen dioxide (NO_2) and particulate matter (PM) which can be divided in PM_{10} (particles with diameters lower than 10 μm) and $PM_{2.5}$.

We now concentrate to PM which is the object of this thesis and for which many studies are available. Today we now that PM_{10} can penetrate deep into the lungs and $PM_{2.5}$ are more harmful since they can cross the lung barrier reaching the blood system. WHO reports that short and long-term exposure to these particles can lead to reduced lung function, respiratory infection and aggravated asthma and in the worst cases can cause lung cancer, acute lower respiratory infection, stroke, ischaemic heart disease and chronic obstructive pulmonary disease. In addiction maternal exposure to ambient air pollution is associated with adverse birth outcomes, such as low birth weight, pre-term birth and small gestational age births. Emerging evidence also suggests ambient air pollution may affect diabetes and neurological development in children.

Cellular studies and chemical analysis of interaction between pollutants and respiratory system reveal that the most harmful properties of atmospheric aerosols are carcinogenicity, mutagenicity, allergenicity. Polycyclic aromatic compounds are known to be carcinogenic and mutagenic, with an increasing damaging potential when nitrated. The substance with the highest mutagenicity found in ambient air is oxygenated nitro-PAH, 3-nitrobenzanthrone, which seems to be emitted from diesel exhausts. Bioaerosols, on the other hand, are the cause of infections, allergy and toxic effects on living organism. After inhalation the effects of these particles range from mild nasal or ocular symptoms to asthmatic shock, depending on their size and the corresponding depths of respiratory tract they reach. Also the oxidation potential, linked to the activity of oxidation-reduction and the formation of reactive oxygen species (ROS) is an extremely important parameter in the definition of the harmfulness of PM. It has been estimated that exposures to traffic-related air pollutants with high oxidative potential are found to be major components contributing to microvascular dysfunction.

	United States		European Union		Japan	China	
(μg / m^3)	PM$_{10}$	PM$_{2.5}$	PM$_{10}$	PM$_{2.5}$	PM$_{2.5}$	PM$_{10}$	PM$_{2.5}$
Daily	150	35	50		35	150	75
Annual		12	40	25	15	70	35

Table 1.1: National environmental standards for different size ranges of particulate matter (PM$_{2.5}$, PM$_{10}$) (Shiraiwa et al., 2017).

The integrated exposure-response (IER) functions are the main mathematical tools for the definition of population response to variation in PM concentration. They are defined through epidemiological cohort studies and require extended measure of PM concentration on different time scale and locations, and also the knowledge of the health effect of each aerosol component. IER is defined as:

$$IER = y_0 \cdot AF \cdot Pop \tag{1.12}$$

where y0 is the baseline mortality rate (BMR) for a given population; AF is the attributable fraction of mortality due to PM$_{2.5}$ and Pop is the population within the age range of interest. The AF is calculated as:

$$AF = (RR - 1)/RR \tag{1.13}$$

Several studies have investigated the relative risk RR for PM$_{2.5}$, deriving different formulations. The last is that obtained by Burnett et al. (2014) and Cohen et al. (2017) which take into account also observations of very high PM$_{2.5}$ from tobacco smoking and indoor air pollution:

$$RR = 1 + \alpha[1 - exp(-\gamma(x - x_0)\delta)] \tag{1.14}$$

Unknown parameters (α, γ, δ) were estimated by nonlinear regression methods based on a collection of epidemiological studies. Estimation of PM concentration needed for epidemiological studies, is performed using a variety of method merging ground measure, satellite and transport models. The main sources of uncertainties are related to the measurement technique and the lack of spatial and temporal coverage, because satellite measures which cover the entire globe suffer of time resolution, while ground measures which can be performed at different time resolutions are concentrated in North America and Europe, and Asian countries.

Improving the ability to measure the concentrations of these particles, separating each species and improving the resolution in space and time, is therefore essential to improve epidemiological studies and consequently the ability to model and predict health effects as emissions vary. A good modeling of these then allows to establish guidelines and limit values of concentration to protect the people's health.

The most recent models show that the annual mean "safe" threshold, below which PM$_{2.5}$ does not contribute to mortality is 2.4 μg m^3. Table shows the National Environmental Standards for Different Size Ranges of PM. It is evident that current standards, based on the knowledge available to date, do not guarantee the health of people and certainly need to be improved if the risk of mortality due to these particles is to be reduced.

Chapter 2

Black Carbon

The previous chapter briefly summarizes the importance of aerosols in atmospheric processes, including their effects on the climate system and human health. One of these has received increasing attention from scholars in recent years, as its particular properties give it a unique role within the climate system. Black Carbon, because of its ability to strongly absorb solar radiation, is in fact the only component of atmospheric aerosol to have a strong heating effect, as well as being one of the main responsible for the high level of pollutants in the urban environment.

This chapter describes BC main properties, sources and effects together with the main methods currently available to measure its concentration in the atmosphere. Information reported has been obtained mainly from the assessment of Bond et al. (2013), Bond and Bergstrom (2006), IPCC report (2013), Moosmüller, Chakrabarty and Arnott (2009).

2.1 Black Carbon definition and properties

The aerosol component known to date in the climate science as "Black Carbon", has had a wide variety of names in the scientific literature. Among these, the first was that of "soot", historically used in describing the black substance in smoke from wood and coal fires, cause of atmospheric pollution (Brimblecombe and Ogden).

Since the end of the 20th century, when the focus on soot has shifted from its role in pollution to that in the climate system, many new methods for measuring its concentration and properties have become widespread. Each of these, however, was based on a different property and was affected differently by its interactions with other atmospheric particles. This has generated over the years confusion and ambiguity in scientific literature. In this research we will use the nomenclature summarized by Petzold et al. (2013) as follows:

- Soot is a useful qualitative description when referring to carbonaceous particles formed from incomplete combustion.
- Black carbon (BC) is a useful qualitative description when referring to light-absorbing carbonaceous substances in atmospheric aerosol; however, for quantitative applications the term requires clarification of the underlying determination.
- Mixed particles containing a BC fraction should be termed BC-containing particles.
- Elemental carbon (EC) should be used for data derived from methods that are specific to the carbon content of carbonaceous matter, such as thermo-optical one.
- Equivalent black carbon (eBC) should be used for data derived from optical absorption methods.

- Refractory black carbon (rBC) should be used for measurements derived from incandescence methods.

The most recent and complete definition is then that of Bond et al. (2013). They define it as a distinct type of carbonaceous material, formed only in flames during combustion of carbon based fuels, distinguishable from other forms of carbon and carbon compounds contained in atmospheric aerosol, because it has a unique combination of the following physical properties: (i) it strongly absorbs visible light; (ii) it is refractory; (iii) it is insoluble in water, in organic solvents including methanol and acetone, and in other components of atmospheric aerosol; (iv) it exists as an aggregate of small carbon spherules.

2.1.1 Formation process

Soot particles are agglomerates of small roughly spherical elementary carbonaceous particles, which form by the incomplete combustion of liquid or gaseous fuels. Its formation therefore occurs when the oxygen content is low compared to the carbon content, with C/O ratios close to 0.5 Wagner (1981). The reaction stoichiometry when C_mH_n is the fuel and there is not sufficient oxygen to form CO_2 as product, is:

$$C_mH_n + aO_2 \longrightarrow 2aCO + \frac{1}{2}nH_2 + (m-2a)C_s, \tag{2.1}$$

where C_s is the soot formed.

The exact formation mechanism is not fully understood yet but it involves the following steps (Masiello, 2004; Moosmüller et al., 2009; Bond et al., 2013): i) pyrolysis of fuel and thermal degradation; ii) formation of polycyclic aromatic hydrocarbons; iii) growth of polycyclic aromatic hydrocarbon structures; iv) gas to particles conversion; v) surface growth and coagulation to form the new particles.

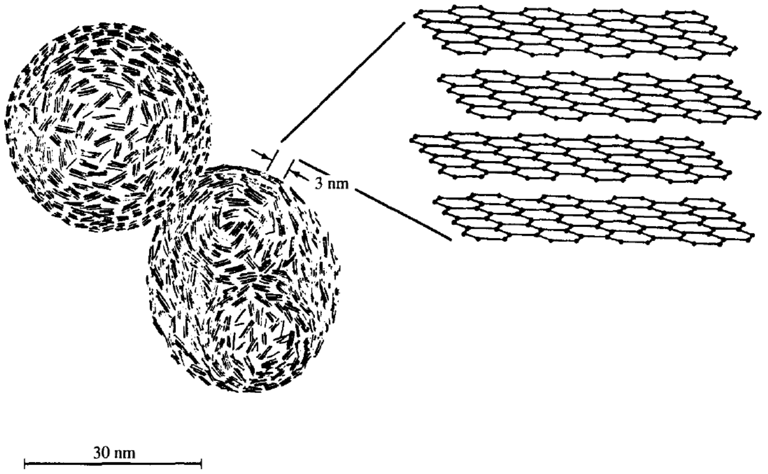

Figure 2.1: Schematic of soot microstructure (John Seinfeld and Spyros Pandis, 2006).

At the end of all these processes spherical elementary particles with diameters of tens of nm are formed. They have a complex chemical structure without a long-range crystalline order, in which graphite layers are mixed with sp^3 bonds and also non carbon constituents. Most models for its internal structure assumes that nanocrystalline graphite regions, called basic structural units (BSUs), are embedded into the short range order of the carbon network. The presence of aromatic bonds provides stability to the particles, making them insoluble and resistant to oxidation even at high temperatures (C. Bond and W. Bergstrom 2007). The optical properties are instead linked to the band gap between the electronic states of the material, which in turn depends on the characteristics of the BSUs and the way in which they are modified in the presence of atoms other than carbon (M. Schnaiter et al. 2003).

Soon after formation spherules coagulate to form aggregates or fractal chain-like structures consisting of hundreds or thousands of them. The morphology acquired in this way, further complicates the modeling of its optical properties, because Mie theory, described in the previous chapter, is strictly defined for spherical particles.

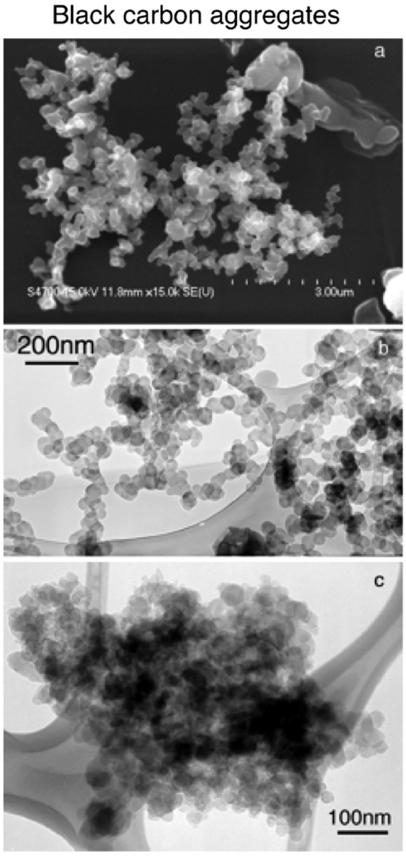

Figure 2.2: (a) Scanning electron microscope image of BC aggregates in young smoke from the Madikwe Game Reserve fire, South Africa, on 20 August 2000; (b) transmission electron microscope (TEM) image of chain-like BC aggregates in flaming smoke from the dambo fire near Kaoma, Zambia, on 5 September 2000; (c) TEM image of a compact BC aggregate in regional haze near Skukuza, South Africa, on 22 August 2000 (Li et al., 2003).

2.1.2 Sources

BC emissions are now mainly associated with energy-related activities and open burning of forests, grasslands and agricultural residues. The 90% of the emissions are due to four major contributors: open burning, diesel engines, industrial coal and residential solid fuels.

- **Open burning** is probably the largest contributor accounting for the 40% of the total. Every day thousands of open fires burn in the world, in particular in Africa and Latin America, mainly in tropical regions and with a very large inter-annual variability. They can develop in forest, grasses and woodland, mainly caused by humans either purposefully or involuntarily. They can also be burned in agricultural fields to clean after harvest or for waste disposal. This source can produce also large quantities of organic matter emitted together with BC which influence its evolution. Despite uncertainties the most recent estimates (Bond et al. 2013) for this source range from 740 Gg yr^{-1} to 12800 Gg yr^{-1}.

- **Diesel engines** is responsible for the 20% of the total and have the lowest co-emission of other species compared to other sources, in particular in regions with high quality control. They can be divided in on road engines such as cars and trucks and off-road engines used in agriculture, construction and other heavy equipment. Most of the emissions occur in Europe, Latin America and North America.
- **Industrial coal** is another major source, to which about 9% of BC emissions are estimated. Although combustors can be designed to have low emissions, there are still simple one highly pollutant, especially in developing countries and small industries. Together with BC they also emit large quantity of SO_2.
- **Residential solid fuels** including wood, agricultural waste, dung and coal used to cook or heat in homes, provide 25 % of BC emissions in particular in Asia, Africa, Latin America and Europe. Most of emissions come from regions in which there is not access to low emission residential energy sources such as electricity and natural gas.

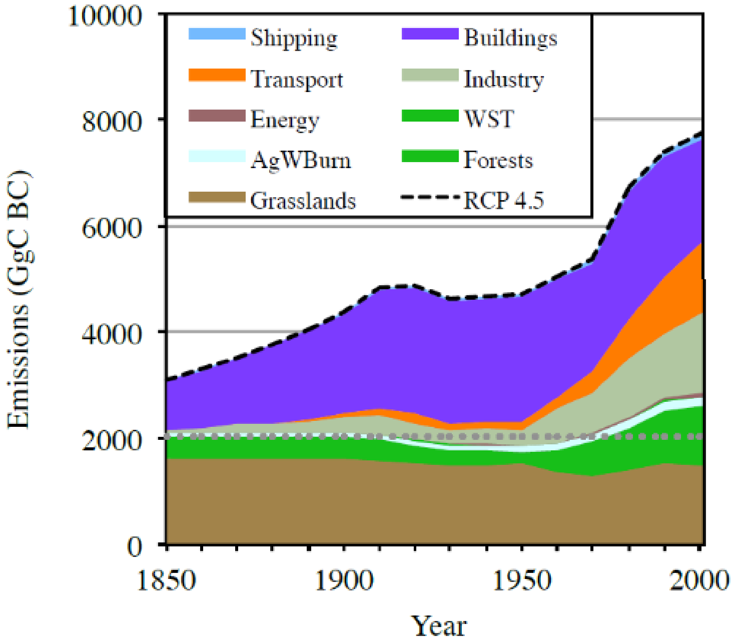

Figure 2.3: Historical black carbon emissions under the global climate atmospheric model and climate policy scenarios. The grey dotted line shows the assumed preindustrial BC open burning emissions (Smith and Bond, 2014).

Other miscellaneous black-carbon-rich sources, including emissions from aviation, shipping, and flaring, account for another 9%, with the remaining 1% attributable to sources with very low black carbon emissions.

Global black carbon emissions have steadily increased over the period 1850-2000 (Lamarque et al., 2010) with a change in the type of sources. In the preindustrial time, BC emissions were dominated by biomass burning for heating and cooking (Bond et al., 2007). Starting in 1850 the global emission of BC have shown a general increase due to coal and biomass consumption in the residential sector. Within the 1950ies the emission rate of BC accelerated under the input of transportation, industrial sectors and forest fires intensity (Smith and Bond, 2014). The increase in emissions and the evolution of sources is displayed in figure 2.3 . Compared to the past, the total emission in the year 2000 was around 5 times higher due to greater energy consumption than in 1750 background, which was 1400 Gg yr-1.

2.1.3 Evolution processes, sinks and distribution

Soon after emission BC aggregates undergo chemical and physical transformations changing their morphology, optical properties and hygroscopicity. Such processing is called atmospheric aging and includes condensation of water vapour or other gaseous species and coagulation with particles present in the surroundings.

The products of these processes can be both external mixture, in which each species reside in different particles, or internal mixture in which different aerosol components exist within the same particle. The latter are no longer pure BC but contain sulphate and organic material. It is commonly accepted that internal mixing of BC takes place, nevertheless a debate on the geometry of the BC-containing particles is still going on.

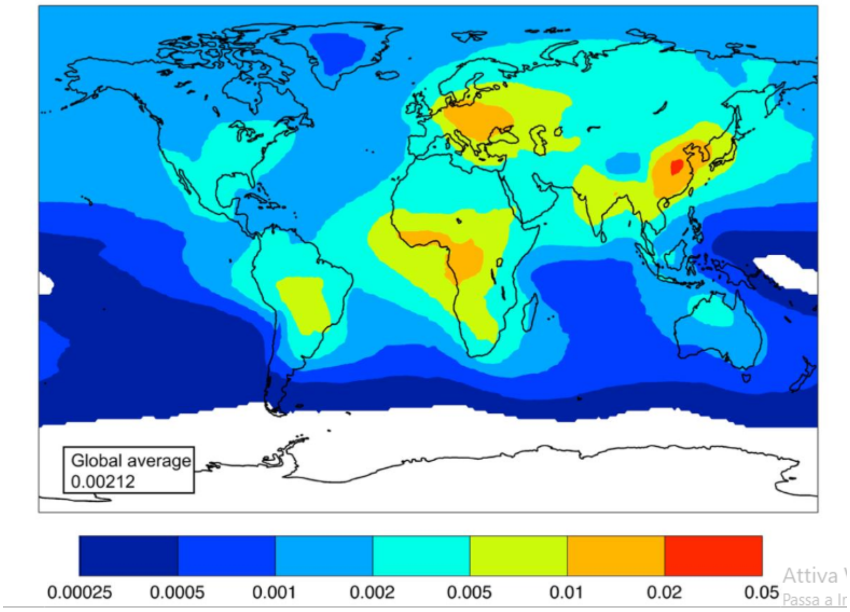

Figure 2.4: Aerosol absorption optical depth associated to black carbon from AeroCom simulations (Bond et al. (2013)).

It is often assumed that non-BC material surrounds the BC completely and symmetrically, such configuration is called core-shell geometry; but mixing geometries with partial and non-concentric shell may also exist (Sedlacek et al., 2012; Adachi et al., 2010; Dahlkötter et al., 2014) as well as BC cores attached to other non-BC particles (Moteki et al., 2014). Optical properties, hygroscopic properties, and thus the cloud-formation potential, and atmospheric lifetime by wet deposition, which can affect transport of these particles to remote locations, such as the Arctic, and feedback on the direct radiative effects (e.g.,Weingartner et al., 1997; Jacobson, 2006; Stier et al., 2006), depends on the mixing state. The definition of the latter is thus crucial in defining BC role for future climate change (Cubison et al.,2008). Most models which simulate the aging processes predict that most BC is mixed after 1 to 5 days.

Due to its small size (submicron diameters) BC has the longest residence time among the atmospheric particles, this allows great horizontal and vertical transport from the source region to high altitude mountains (Lavanchy et al.,1999; Ming et al., 2009), and polar regions (McConnell et al., 2007; Bourgeois and Bey, 2011; Bisiaux et al., 2012a, 2012b). Therefore, BC is ubiquitous in the atmosphere, but the spatial distribution, usually simulated using global chemistry and transport models, shows certain heterogeneity. Due to geographic distribution of continents, and highly industrialized and densely populated countries, the atmospheric concentration of BC in the northern Hemisphere is 10 times higher than the southern Hemisphere (Chung and Seinfeld, 2002; Ramanathan & Carmichael, 2008). Additionally, regional hotspots of atmospheric BC burden include the Indo-Gangetic plains in South Asia, Eastern China, most of South-east Asia and regions of Africa between sub-Sahara and South Africa. Other weaker hotspots are found over Europe, urban North and South America (Chung and Seinfeld, 2005; Ramanathan and Carmichael, 2008) as shown in figure 2.4.

2.1.4 Optical properties

The main intensive optical property describing how BC containing particles interact with radiation, used in radiative transfer models and instruments, to relate the absorption coefficient to mass concentration, is the mass absorption cross section (MAC). Knowing its values at all wavelength and the mass concentration in the atmosphere, the absorption coefficient can be derived by the relation:

$$b_{abs}(\lambda) = MAC_{BC}(\lambda) \cdot [BC], \tag{2.2}$$

where [BC] is the mass concentration in g/ m^3.

The optical properties of BC containing particles and thus their MAC depend on refractive index, density, size distribution, mixing state, and particle shape, so both formation and aging processes can change them. A MAC's variation may introduce a significant change in the single scattering albedo (SSA), which is used to quantify the warming or cooling effect of an aerosol. The influence of aging on MAC is still widely investigated because the SSA is the aerosol property most relevant to the balance between negative and positive forcing.

A wide variety of MAC values determined from measurements is available in the literature. It was found that freshly generated and uncoated BC has a MAC of 7.5 ± 1.2 g^{-1} m^2 at 550 nm (Bond and Bergstrom, 2006). MAC values from atmospheric measurements have a range spanning between 4 and 23 m^2 g^{-1} at 637 nm , depending on emission type (Genberg et al., 2013), distance from source (Cozic et al., 2008; Pandolfi et al., 2014) and instrumental approach (Slowik et al., 2007; Knox et al., 2009). MAC enhancement values from atmospheric measurements show high variability and need to be measured before and after thermal removal of the coating. Laboratory experiment showed that the enhancement is proportional to the coating thickness. A MAC enhancement, with respect to a bare BC core, between 1.2 and 1.6 was observed close to emission (Knox et al., 2009) and 1.4 for biomass burning plumes (Lack et al., 2012). However, not all field observations agree on the enhancement amplitude; for urban plumes a weak absorption enhancement of 6 % was observed (Cappa et al., 2012).

The MAC of BC can also be simulated using optical models. For BC containing particles the geometry of the mixing is a fundamental parameter to account for. Usually, a core-shell configuration is assumed. The assumption of different mixing rules leads to a different absorption and absorption enhancement: Adachi et al. (2010) calculated a MAC at 550 nm for uncoated BC spheres of 6.4 m^2g^{-1}, where the MAC increases for volume mixing, core shell and Maxwell-Garnet effective medium approximation up to 13.6 m^2g^{-1}. A MAC of 9.9 m^2 g^{-1} was attributed to a more realistic BC particle. The absorption enhancement is also sensitive to the chosen geometric configuration; compared to a bare spherical BC the enhancement might vary between 1.5 and 2.1.

Radiative transfer models require the scattering and absorption coefficient. Atmospheric models convert modeled mass concentrations of BC into optical coefficients using the MAC and the mass scattering cross-section (MSC). An accurate estimation of these intensive properties is crucial in order to estimate a proper radiative forcing of aerosol, including BC.

2.2 Black Carbon impacts

2.2.1 Human health effects

Black carbon is one of the main components of pollution linked to combustion emissions and its high concentrations were particularly evident at the beginning of the industrial period, when combustors were still backward and very polluting. The black component of the particulate matter was used as an indicator of air pollution, which negative effects on health have long been recognized and studied for decades. The first guidelines adopted in the European Union to establish exposure limits were based on the monitoring of black smoke (or British smoke). From the 2000s onward, it was understood that adverse health effects could be caused not only to black particles but by a wide variety of chemical species. It was thus decided to use the mass concentration of all respirable and inhalable particles as an indicator of harmful pollution, as described in the previous chapter. However, the individual effect of BC is still being studied in order to understand both its possible interactions with the body at a microscopic level and its possible greater effectiveness as a risk indicator. Unfortunately, the studies carried out so far are still incomplete and sometimes contradictory.

Epidemiological studies in which changes in health (all-cause and cardiovascular mortality, and cardiopulmonary hospital admissions) are related to changes in BC concentration (measured as EC), show a good association both in the short and long term. Short-term studies suggest that BC may be a better indicator of harmful particles from combustion sources than undifferentiated PM mass, while long term studies are inconclusive. Toxicological studies also suggest that it may not be a major direct component of toxic PM, but that it has the capacity to carry a wide variety of chemical compounds of different toxicities within the human body. For these reasons it makes sense to keep the mass of $PM_{2.5}$ as the primary indicator in quantifying human exposure to pollution risks, although BC may be a useful additional factor in indicating the component of this due to combustion processes (Janssen et al., 2012).

2.2.2 Climate effects

Black carbon plays a unique and important role within the climate system. Last report of the IPCC poses it as most likely the second polluting species having a warming effect on the atmosphere. Estimate of the industrial-era total forcing of BC is equal to +1.1 Wm^{-2} with 90 % uncertainty bounds of +0.17 to +2.1 Wm^{-2}. This value is lesser than that derived for carbon dioxide (CO_2) in 2005 which were +1.56 Wm^{-2} but higher than that of methane (CH_4) corresponding to +0.86 Wm^{-2}. This total forcing can be divided in three main processes: BC Direct Radiative Forcing (DRF), BC Cloud Effects (both semi-direct and indirect), BC in snow and sea-ice effects.

- **BC Direct Radiative Forcing** best estimate for the industrial-era is +0.71 Wm^{-2} with 90 % uncertainty bounds of +0.08 to +1.27 Wm^{-2}. It is affected by BC emissions, lifetime in the atmosphere, mainly related to removal processes, optical properties, summarized by MAC_{BC}, and absorption forcing efficiency (AFE). It thus depends on uncertainties in the quantification and parametrisation of these terms in climate models.

- **BC Cloud Effects** best estimate of the industrial-era forcing is positive and equal to +0.23 Wm^{-2} with a -0.47 to +1.0 Wm^{-2} 90 % uncertainty range. The semi-direct effects are those resulting from the ability of BC to heat the atmosphere above, below or inside the clouds, changing its stability and moisture content and leading to evaporation of cloud's droplets. Depending on atmospheric conditions and BC position relative to clouds, these processes enhance or decrease cloud cover leading to both a positive or negative effect on the energy balance. In divergent regions, the presence of BC above clouds, stabilizes the atmosphere increasing stratocumulus clouds (cooling), but decreasing cumulus (heating). In some convergent regions it can induce upper level convection leading to low level convergence of moisture, which enhances cloud formation (cooling). BC below clouds destabilizes the atmosphere increasing convective clouds (cooling). BC in clouds induces evaporation of droplets reducing cloud cover both at high (cooling) and low level (heating). Indirect effects are instead variation induced in cloud albedo or cloud lifetime due to the ability of BC to activate CCN and IN. BC contributes to increase the particle number concentration and can activate both CCN (easily when mixed with soluble species) and IN, but it can also reduce CCN providing a surface upon which volatile inorganic or organic compounds may condense, instead of forming pure particles. The impact of these indirect effect are very difficult to evaluate and it is not clear if they have a cooling or an heating effect on climate.

- **BC in snow and sea-ice**. In addiction when deposited on snow and ice BC induce melting and variations in albedo, that result in a positive climate forcing. The best estimate for the industrial-era climate forcing due to deposition of BC on snow and ice is +0.13 Wm^{-2} with 90 % uncertainty bounds of +0.04 Wm^{-2} to 0.33 Wm^{-2}.

BC therefore has the ability to strongly influence climate on a global scale (particularly in the northern hemisphere) by causing tropospheric warming and inducing climate responses in the form of changes in clouds, circulation, surface temperature and precipitation. In addition to the global effect, due to its great variability, it causes changes in atmospheric stability, cloud cover and precipitation on local and regional scale. Local radiative forcing can also reach a value of +10 Wm^{-2}.

The main sources of uncertainty in the definition of its impact derive from: (i) difficulties in distinguishing between the different absorbent components, i.e. BC, organic carbon and dust; (ii) estimates of emission rates from the different sources; (iii) vertical profile and removal rates; (iv) effects on clouds; (v) accuracy of climatological models in which all the above information are included.

The adverse health effects of particulate matter emitted by combustion sources call for a drastic reduction in emissions. However, most aerosols have a cooling effect on the climate and their reduction could lead to a further rise in surface temperature. BC-rich sources are an interesting prospect as their reduction could combine forced climate change mitigation with PM reduction.

2.3 Techniques for measuring the mass and optical properties of BC

As mentioned at the beginning of the chapter there are different techniques to measure the amount of Black Carbon present in an air sample, each based on a different property of this aerosol. They provide approximately equivalent results when used on pure BC samples, but may differ greatly for samples collected in the atmosphere. The main reason for these differences is that BC is mixed with other substances in the atmosphere and filter deposition may cause further mixing. Each technique is influenced in different ways by the other substances present and it is very difficult in each to isolate the effect of BC alone. The most used ones can be grouped into three categories: optical, thermo-optical and laser-induced incandescence.

2.3.1 Optical techniques

In this technique the directly measured property is the absorption coefficient, from which the mass concentration can be derived by the relation:

$$b_{abs} = BC_{conc} \cdot MAC. \tag{2.3}$$

The quantity thus derived, which is based on the optical properties of the sample, is called equivalent black carbon (eBC) and strongly depends on MAC value used, which is affected by mixing state, coating and presence of other absorbing aerosols. In optical instruments, the sample can be either collected on a filter or measured in its natural suspended state. The most common method for this kind of measure are the photoacustic method and the filter based spectrometer (Moosmüller, Chakrabarty and Arnott, 2009).

Photoacustic method is a method for measuring absorption with in situ detection. Particles are irradiated using light modulated at acoustic frequency, the heat produced is transferred to the surrounding gas creating an increase in pressure sensed by microphones. This techniques is biased by gas phase absorbers (Petzold and Niessner, 1996). The intensity of the sound wave is proportional to the amount of black carbon. The main advantage of the photoacoustic method is the independence of the measurement to the mixing state of BC (Lack et al., 2009). It is therefore commonly accepted as a benchmark for measuring aerosol absorption. However, its use and maintenance is rather demanding and it cannot really be used in long-term measurements.

Filter based photometers measure aerosol absorption after the sample deposition on a fiber filter, which can be made of different materials such as quartz of glass. In these instruments particles are continuously deposited on an area A_f of the filter with a known volume flow F. This results in the deposition of particles from a sample volume F$\cdot\Delta t$ during a time interval Δt with a flow velocity F/A$_f$. If the particles did not scatter the radiation, it would be possible to derive the absorption from a simple transmission measurement, which is carried out by detecting the radiation intensities transmitted by a blank and a loaded filter. These two intensities are linked by the Beer relation as follows:

$$I = I_0 e^{-(b_{abs}+b_{sca})\cdot\frac{\Delta t F}{A_f}} \tag{2.4}$$

If the particles do not scatter or have a known scattering coefficient, the absorption coefficient can then be derived from:

$$b_{abs} = \frac{A_f}{\Delta t \cdot F}\ln(\frac{I_0}{I}) - b_{sca} \tag{2.5}$$

The implicit assumptions in this equation are that: scattering and absorption do not change when particles are concentrated on a very thin layer; filter scattering and its optical interactions with particles may not affect their ability to absorb; morphology does not change after deposition or that this change does not affect optics. In addiction these instruments can be affected by change in MAC due to BC aging processes and by the presence of other absorbers such as dust or organic carbon. However, they are relatively cheap, robust and plug and play instruments and for these reasons they are widely used for long-term measurements.

Principal instruments which use this principle are: Particle Soot Absorption Photometer (PSAP), the Aethalometer and the Multi-Angle Absorption Photometer (MAAP). Characterization and comparability of different absorption photometers and data treatments are under continuous development. In the next chapter specific photometers used in this thesis and the way in which their values has been treated are described in more detail.

2.3.2 Thermo-optical techniques

Thermo-optical analysis is currently considered, by the European standardization body (CEN), as reference for the quantification of organic carbon (OC) and elemental carbon (EC) in ambient air.

Elemental carbon (EC) is described as the carbonaceous fraction of particulate matter that is thermally stable in an inert atmosphere to temperatures near 4000 K and that can only be gasified by oxidation starting at temperatures above 340 °C. It is assumed to be inert and nonvolatile under atmospheric conditions and insoluble in any solvent (Ogren and Charlson, 1983).

OC component is instead that fraction of carbon that evolve during heating cycles in an inert atmosphere. In this method the particles are deposited on a filter, later analyzed under controlled temperature, RH and gaseous composition.

The method is based on the idea that OC and EC can be separated by heating to the point where OC has evaporated away and only EC remains. A variety of protocols have been developed to measure these two component which differ in the temperatures and duration of exposure. While all of them agree in the total carbon estimate, they can differ significantly in the amount of OC and EC, so the research is still ongoing (Schmid et al., 2001; Cavalli et al., 2010) to correct for all possible artifacts.

The main difficulty in distinguishing the two components relies in the pyrolysis of OC in inert atmosphere during heating. The pyrolytic carbon remains on the filter and can be erroneously ascribed as EC causing its overestimation. To correct for this effect, a continuous measure of transmittance or reflectance is performed while heating.

The most widely used methods includes NIOSH-like, IMPROVE_A and EUSAAR_2, that differ in heating cycles and optical method chosen. In the next chapter the protocol EUSAAR_2, used in this research, will be described in more detail.

2.3.3 Laser-induced incandescence

Laser induced incandescence is finally a technique for detecting BC in situ without collecting sample on filter. It is based on the fact that it can be heated, thanks to its ability to absorb radiation, up to very high temperatures (4000 K) without volatilizing. For this reason, the quantity measured with this technique is called refractory BC (rBC).

Soot particles are heated by a high power laser source to temperatures high enough to cause the emission of a measurable amount of black body radiation. The emission is then recorded with different methods, some that integrate over time and provide a measure of spatial distribution or concentration in the volume, others with temporal resolution that allows you to measure even the individual particles.

This technique is made possible by the refractoriness of soot and is therefore highly selective and specific technique for its detection, independently of the amount of non-refractory, internally mixed matter (Moteki and Kondo, 2010; Michelsen et al., 2015). The main instruments used are: the single particle soot photometer (SP2; Stephens et al., 2003) and the soot particles aerosol mass spectrometer (SP-AMS; Onasch et al., 2012).

Chapter 3

Experimental

In the previous chapters the important role played by aerosol particles, in particular by the absorbing component, on climate system on different scales and health, has been assessed. To better quantify this impact, the characterization of their properties and a measure of their concentration in different location and environments are then crucial.

The main objective of this thesis is the characterization of the aerosol optical properties in the Po Valley in July 2017, during a measurement campaign of the ACTRIS (Aerosol, Clouds, and Trace gases Research InfraStructure Network) project, a pan-european initiative with the aim of integrating observations and related research of aerosols, clouds, and trace gases (https://www.actris.eu). In particular, we focused on the absorbing component of the aerosol and the measurement of BC concentration, comparing different techniques currently available but still rich in uncertainties. This chapter contains a description of the three measurement sites, the experimental set up and data analysis procedure.

3.1 Measurement sites

The Po Valley is a region situated between the Alps and the northern Apennines, which extends to the Adriatic Sea. It is the largest industrial, trading and agricultural area in northern Italy with a high population density. Along the course of the Po river you can find large factories, power plants and cities. The ports of Ravenna and Venice are also crossed by big ships, producing high level of SO_2. For all these reasons, it is an heavily

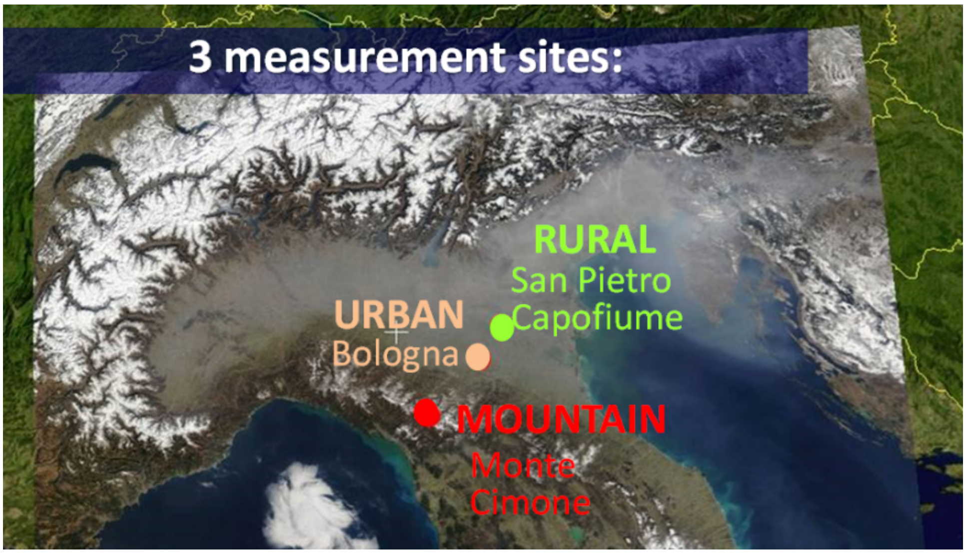

Figure 3.1: Geographic location of the three different sites.

polluted area with one of the highest PM levels in Europe. The blanket of pollution that overlooks it is clearly visible from satellite images (figure 3.1).

The Po Valley includes three super-sites (figure 3.1): Bologna CNR-ARPAE (54m, active from 2010), S.Pietro Capofiume CNR-ARPAE Supersite (11 m, active from 2001), and Mt. Cimone GAW Global Station (2165 m, active from 1996); with elevation spanning from sea level up to the free troposphere, that offer the possibility to analyse the vertical gradient of absorbing aerosol over a 2 km-tick tropospheric layer. Their different locations from urban to mountain background provide also the possibility to gain information on the variability of the aerosol population depending on sources, background and aging time.

3.1.1 Monte Cimone

The Italian Climate Observatory “O. Vittori” (ICO-OV) GAW-WMO Global Station, is located on the top of Mt. Cimone (MC), the highest peak of the northern Italian Apennines, near the borderline between two different climate regions: Continental Europe to the north and the Mediterranean basin to the south. It is also about 50 km far from the Tyrrhenian Sea and 130 km from the Adriatic Sea. The major cities closest to this mountain are Bologna and Florence, located in the plain and at a distance of about 60 km. The nearest industrial areas are at least 40 km away, while the nearest inhabited areas are small towns 15 km away and 1100 m below. The nearest roads are 7 km away and one km lower and the environment surrounding the station is characterized by meadows and rocky areas. The woods, mainly of conifers and beeches stop at an altitude of 1600 m. This site has a completely free horizon at 360 degrees and can therefore be reached freely by air masses from any direction.

Figure 3.2: Monte Cimone site (MC).

Due to the combination of all these characteristics, completely free horizon, high altitude and great distance from major pollution sources, this observatory represents a strategic location to study the chemical-physical characteristics and climatology of the free troposphere in the South Europe and North Mediterranean basin. In the summer and warmer months, however, it is possible that the air of the boundary layer reaches this site due to the increase in convective processes and mountain breeze systems (Marinoni et al., 2008). These months are therefore typically characterized by higher values of pollutants than the winter ones. In addition to the transport of polluted air from the plain, this site may also be affected by other typical phenomena. In particularly hot and dry periods this Mediterranean region is subject to numerous fires, which can develop in the forests of Spain, Italy, Portugal and Greece, significantly influencing the composition of trace gases and the properties of aerosols, both at high altitude and in the low troposphere (Cristofanelli et al., 2009). In addition, Monte Cimone is one of the first peaks that air masses from Africa may encounter during their long-range transport. For this reason the site is affected by significant events of dust transport from the Sahara desert, identified by an increase in the concentration of aerosols in the coarse mode. Previous studies indicate that BC concentrations at this site are subject to an obvious seasonal cycle, with lower values in winter and higher in summer, with an average (calculated from 2005 to 2015 data) of 285.7 ng m^{-3} (Duchi et al., 2015).

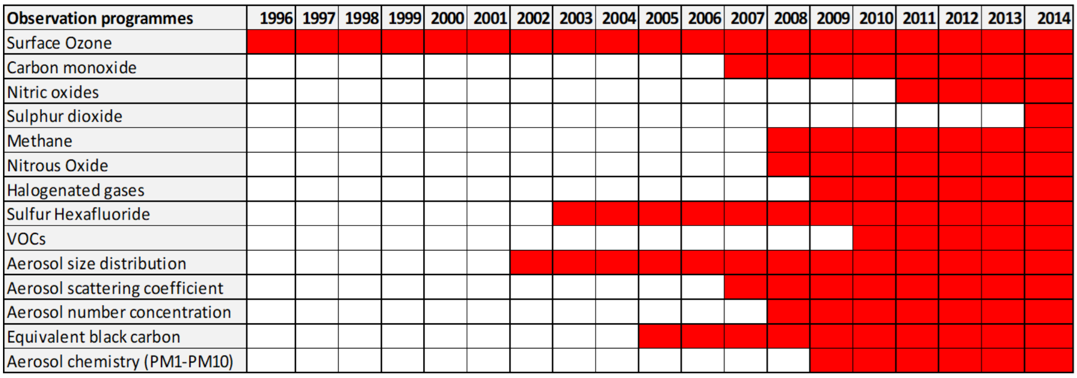

Observation programmes	1996	1997	1998	1999	2000	2001	2002	2003	2004	2005	2006	2007	2008	2009	2010	2011	2012	2013	2014
Surface Ozone	🟥	🟥	🟥	🟥	🟥	🟥	🟥	🟥	🟥	🟥	🟥	🟥	🟥	🟥	🟥	🟥	🟥	🟥	🟥
Carbon monoxide												🟥	🟥	🟥	🟥	🟥	🟥	🟥	🟥
Nitric oxides																🟥	🟥	🟥	🟥
Sulphur dioxide																			🟥
Methane													🟥	🟥	🟥	🟥	🟥	🟥	🟥
Nitrous Oxide													🟥	🟥	🟥	🟥	🟥	🟥	🟥
Halogenated gases														🟥	🟥	🟥	🟥	🟥	🟥
Sulfur Hexafluoride								🟥	🟥	🟥	🟥	🟥	🟥	🟥	🟥	🟥	🟥	🟥	🟥
VOCs															🟥	🟥	🟥	🟥	🟥
Aerosol size distribution							🟥	🟥	🟥	🟥	🟥	🟥	🟥	🟥	🟥	🟥	🟥	🟥	🟥
Aerosol scattering coefficient												🟥	🟥	🟥	🟥	🟥	🟥	🟥	🟥
Aerosol number concentration													🟥	🟥	🟥	🟥	🟥	🟥	🟥
Equivalent black carbon										🟥	🟥	🟥	🟥	🟥	🟥	🟥	🟥	🟥	🟥
Aerosol chemistry (PM1-PM10)														🟥	🟥	🟥	🟥	🟥	🟥

Figure 3.3: General sketch of the main parameters monitored in continuous at Monte Cimone.

Continuous monitoring of climate-altering compounds (trace gases and aerosol), solar radiation as well as meteorological parameters are carried out. The Monte Cimone activity can help to better monitor the changes of atmospheric composition, to investigate the processes influencing climate and to assess the contribution of short and long-range air mass transport to atmospheric variability. Monte Cimone is part of several international networks devoted to the long-term monitoring of atmospheric properties and climate change study (GAW/WMO, ICOS, ACTRIS). Data from MC were also used to calibrate and verify data from satellites and model simulations.

The CNR observatory is hosted by the Italian Air Force on its own Observatory. The scientific activity is mainly supported by cooperative national and international research programs and the wide set of atmospheric measurements has been established thanks to collaboration of several research Institutions and Universities. MC is one of the 29 Global Stations of the GAW-WMO program (the only existing in Italy), it is part of NextData project, ACTRIS-2 , ICOS and AGAGE projects; it contributes to CAMS and WMO SDS-WAS by providing near-real time data of atmospheric composition.

At the time of the measurement campaign in July 2017, the station was equipped for optical and thermo-optical measurements with the following instruments: Multi Angle Absorption Photometer MAAP (Thermo Scientific 5012), Nephelometer (TSI 3563), Aethalometers (MAGEE Scientific model AE31 and AE33) and filters for thermo-optical analysis (Sunset Laboratory, EUSAAR-2 protocol).

3.1.2 St. Pietro Capofiume

In the rural site of St. Pietro Capofiume (SPC), is located the weather station "Giorgio Fea" of ARPA with which the CNR collaborates performing field measurements for 30 years. The original main scientific goal was the study of the processes affecting fog formation and evolution. More recently gas and aerosol measurement programs are conducted here. It is used in a large number of measurement campaigns for national and international projects such as the SUPERSITO project or the ACTRIS network.

It is equipped for online monitoring of gases (sulfur dioxide , ammonia, nitrogen oxides , ozone) , particulate matter sampling for offline atmospheric chemical composition and measurements of size distribution number concentration (by twin - DMPS in collaboration with the University of Kuopio). Radar measurements and radio soundings are also performed here, and during field campaign the characterization of physico-chemical-optical properties of both columnar aerosol population (sun photometry and lidar) and at ground (aerosol scattering and absorption measurements) is performed together with an accurate evaluation of the radiative balance and albedo description.

Figure 3.4: St. Pietro Capofiume site (SPC).

This station is located north-east of Bologna at a distance of about 30 km, in a sparsely populated and rural area, open to the sea on the east side and closed by residential and densely populated areas in other directions (Hamed et al., 2007). Being completely immersed in the Po Valley region, but far from direct sources, it is a good reference point for the evaluation of the background condition of this industrial and highly polluted area.

For this campaign the site was equipped with a Multi Angle Absorption Photometer MAAP (Thermo Scientific 5012), two Aethalometer (MAGEE Scintific model AE31 and AE33), a Nephelometer (TSI 3563) and filters for thermo-optical analysis (Sunset Laboratory, EUSAAR-2 protocol).

3.1.3 Bologna

The site of Bologna (BO) is located inside the research area of CNR, via Gobetti and is classified as urban background station. This site is made up by the two measurement stations in figure 3.5: (a) the CNR-ISAC Air Quality Station sited on the top of the ISAC building, at about 25 meter on the ground; (b) ARPAE Supersite for Air Quality Measurements sited at ground level near the ISAC Institute.

The site on the roof of the CNR is not directly affected by sources of pollution but analyzes the urban background of Bologna. It is a site representative of a highly urbanized and densely populated environment, with large busy roads and an airport.

It was designed specifically to execute aerosol and reactive gases measurements according with WMO/GAW and ACTRIS recommendations and standard operation procedures. A particular attention was dedicated to the stabilization and control of the sampling flow rates and temperatures, as accurately described in Cristofanelli et al. (2018). The container is actually available for field campaigns, the instrumentation for long term monitoring is foreseen in the next future in the framework of ACTRIS Research Infrastructure.

(a) (b)

Figure 3.5: Bologna site (BO) with the two measurement stations: (a) the CNR-ISAC Air Quality Station and (b) ARPAE Supersite for Air Quality Measurements.

During the measurement campaign, the following instruments for the measurement of Elemental Carbon and the optical properties of particulate matter were present: a Multi Angle Absorption Photometer MAAP (Thermo Scientific 5012), an Aethalometer (MAGEE Scintific model AE31), a Nephelometer (TSI 3563) and filters for thermo-optical analysis (Sunset Laboratory, EUSAAR-2 protocol).

3.2 Flexpart lagrangian simulations

In the study of atmospheric transport, the Lagrangian approach allows to characterize the source-receptor relation of atmospheric tracers. In particular, Flexpart (Stohl et al. 2005) can simulate long range and mesoscale transport, reproducing the diffusion and dry and wet deposition. Simulations are based on the release of a cluster of parcels from a three-dimensional box and the estimate of the evolution of their physical properties (as temperature, density, pressure, mass) during the advection.

For the ACTRIS-2 2017 field campaign ISAC researchers run a backtrajectory lagrangian model in order to provide the path of atmospheric air masses reaching the measurement sites. A 1000 back-trajectories cluster, representative of a generic aerosol tracer, is released every 6 hours from a 3D box of 0.5°x 0.5° x 500 m dimensions over each measurement sites, traveling back in time for 4 days.

The main outputs obtained are:

- The footprint (figure 3.6 a): it represents the residence time of the released back-plume over each grid bin. Colors hence indicate the regions where the air masses are spending the most time during the previous 4 days, and therefore highlights which source regions may affect more likely the receptor measurement site. The red circles indicate the position of the center of mass of the cluster each 24 hours back in time. Their dimensions give an indication of the particles dispersion around the barycenter of the cluster

- Time series of concentration of advected species (figure 3.6 b): coupling the footprint (time units) with emissions inventories (mass · time-1 units) and integrating over the geographical domain covered by the plume, is possible to reconstruct the potential contribution of each source region to the concentration of the species that will be observed at the measurements site. We use here EDGAR and RETRO inventories for the CO species and DREAM for Dust.

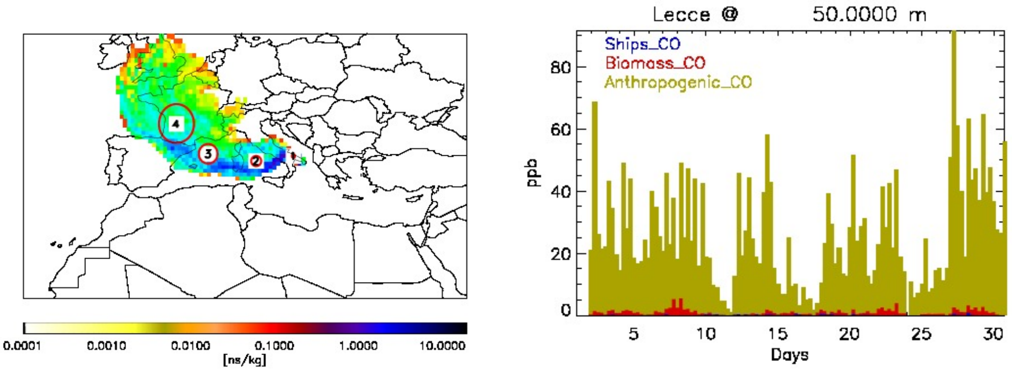

(a) (b)

Figure 3.6: Example of Flexpart results. a) Footprint, Lecce, 04 June 2016 12:00; b) Time series of CO transport on Lecce, June 2016.

3.3 Instruments

3.3.1 Nephelometer (TSI 3563)

The integrating Nephelometer is the most widely used instrument for measuring the scattering coefficient b_{sca} due to aerosol particles in a volume of air.

In its most common configuration, an integrating Nephelometer measures the amount of light scattered by a sample of air at one or more wavelengths, using a small near-Lambertian, diffuse, light source. The sample air is drawn into a blackened sample chamber where it is illuminated by a very bright LED array (light source). The light scattered by the sample of air is detected by a photomultiplier operating in photon-counting mode. The fraction of the scattering due to particles is separated from that due to air. It is scaled in the instrument's controller using stored calibration factors, and then logged in the data memory. The instrument is calibrated by introducing filtered air, to give an aerosol zero, and a gas with a known scattering coefficient, typically CO_2 to give the span. When the instrument performs a zero adjust in particle-free air (that is, where only Rayleigh scattering is present), the b_{scagas} component is measured and subtracted for obtaining the $b_{scaparticle}$ parameter.

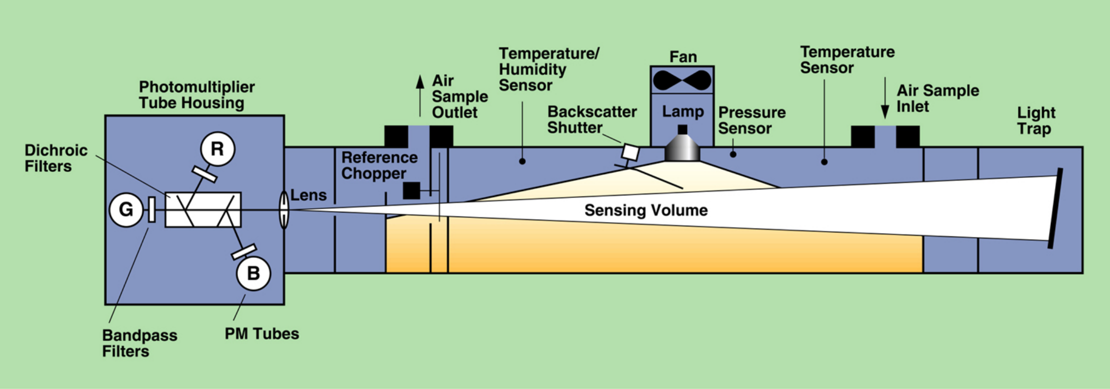

Figure 3.7: Schematic of TSI 3563.

The three-wavelength model (TSI 3563) is also able to split the scattered light into a red (700 nm), a green (550 nm), and a blue (450 nm) component, giving the corresponding scattering coefficient at different wavelength. Figure 3.7 shows a schematic picture of this instrument. The main body consists of a 90 cm long dark aluminium tube with a diameter of 10 cm.

Along its axis are placed aperture plates in a tube with a diameter of 8 cm. The

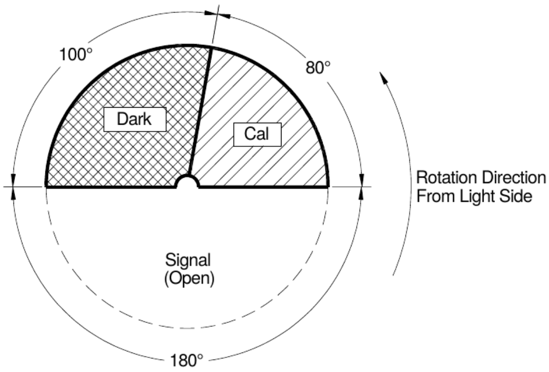

Figure 3.8: Chopper scheme.

aerosol illumination is performed by a 75 Watt quartz halogen lamp (emitting in the visible spectrum) and the plates limit the light integration between 7° and 170°. The backscattered shutter allows to block the light between 7° and 90° to only measure the backscattering. At one end of the tube is placed the receiving optics (3 photomultiplyer, one for each wavelength measured), while at the other end a light trap to provide a very dark reference against which to view the light scattered by particles and gases.

The light coming from the tube passes through a chopper whose scheme is shown in the figure 3.8, which allows to separately measure: the photomultiplier tube (PMT) background noise, a measure of lamp stability over time and the effective signal that comes from the measuring volume. After interacting with particles and gases the light passes through lens and filters that divide it into the three wavelengths of interest before reaching the photomultiplier tubes.

The signal is then converted in the value of the scattering coefficient, using a model based on the Mie theory. The scattering coefficient due to forward scattering is the integral of the scattering function $\beta(\theta)$, that describes the fraction of light scattered at each angle:

$$b_{sca} = 2\pi \int_0^{\pi} \beta_p(\theta) sin(\theta) d\theta. \tag{3.1}$$

From the Mie theory it is known that this function, for a population of particles with number concentration N and size distribution N(D_p), can be written as:

$$\beta_p(\theta) = \int_0^{\infty} \frac{|S(\theta,\alpha,m)|^2}{2\pi\alpha^2} \frac{\pi D_p^2}{4} \frac{dN}{d\log D_p} d\log D_p, \tag{3.2}$$

where α is the size parameter, m is the refractive index and S can be derived from the theory. It can also be proven that, with an isotropic (Lambertian) source of light, the radiation flux (W m^{-2}) that reach the sensor is:

$$F_{sensor} = \frac{I_0 \omega_{sensor}}{y} \int \beta_p(\theta) \sin\theta d\theta, \tag{3.3}$$

where I_0 is the amplitude of the incident radiation, ω_{sensor} is the solid angle whereby the light reach the sensor, y is the distance between the source and the optical axes of the instrument as shown in figure 3.9.

Comparing the two equations it can be observed that the signal of the instrument is theoretically proportional to the scattering coefficient through constants that depend on its constructive characteristics. In this derivation it has been assumed that: the Nephelometer is sensitive to radiation scattered between 0° and 180°, each volume of air acts as a point source of scattering, the lamp represents an isotropic light source. It is also assumed that scattering at every λ is the aerosol's response to a monochromatic light source at that wavelength. The value of F_{sensor} is determined by the sensor electronics using a series of equations and calculations based on parameters derived from a calibration procedure, carried out by means of gases with known optical properties typically CO_2 and particle free air.

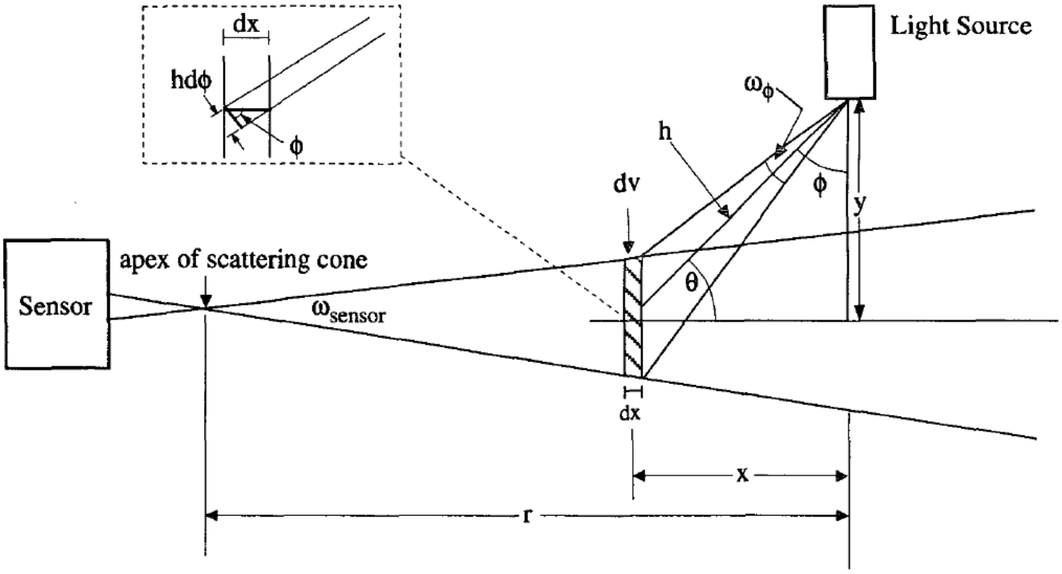

Figure 3.9: Geometry of integration in the Nephelometer.

The values of b_{sca} measured by Nephelometer are subject to uncertainties which derive from this calibration procedures and from systematic errors due to non-idealities in its operations. The uncertainties due to the non-idealities of the instrument, discussed and estimated by Anderson et al. (1996), are related to limitations in the constructive design and mainly concern the wavelength and angular sensitivity. The non-ideality related to wavelength is due to the fact that the scattering coefficient is measured against a narrow but finite wavelength range, not perfectly centered on the nominal wavelength. That in angular sensitivity comes from two main causes: the intensity of the light produced by the source should be perfectly isotropic but that's not it, the angles on which the real integration takes place are between 7 ° and 170 ° instead of between 0 ° and 180 ° (truncation error).

The errors in the Nephelometer scattering coefficient (b_{sca}) due to truncation and wavelength non-idealities are reported to be a few to 10% for submicron particles, signal levels > 10 Mm^{-1} and averaging intervals ≥ 60 s (Anderson et al. 1996). While can be higher for coarse particles. A complete characterization and quantification of uncertainties, due to instrumental noise and calibration drift, can be obtain by routinely characterizing the instrumental response to calibration gases such as air and CO_2. This was not done in this study, where the truncation error correction procedure, developed by Anderson and Ogren 1998, was used. A correction factor C has been defined such as:

$$b_{sca}^{corrected} = b_{sca}^{measured} \cdot C, \tag{3.4}$$

in which:

$$C = a + b \cdot SAE. \tag{3.5}$$

Values of a and b found by Anderson and Ogren 1998 and used for correcting data, are summarized in table 3.1. The uncertainty attributed to corrected data results from the combination of that of uncorrected data and that of the correction factor C evaluated in Anderson and Ogren 1998 and is about 25%.

3.3.2 Multi Angle Absorption Photometer (Thermo Scientific 5012)

The Model 5012 Multi Angle Absorption Photometer (MAAP) is a filter based instrument for the determination of absorption and mass concentration of BC at a single

	450 nm	550 nm	700 nm
a	1.365	1.337	1.297
b	-0.156	-0.138	-0.113

Table 3.1: Anderson and Ogren's a and b parameters for truncation error correction at different wavelengths.

wavelength of 635 nm. It uses a technique that allows to reduce possible biases and uncertainties due to scattering, based on the simultaneous measurement of both scattered and transmitted light. A complete treatment of this method is given in Petzold and Schonlinner (2003). The transmitted intensity through the filter can be parameterized by a $T(\theta) \propto \cos(\theta)$ relationship, with θ being the scattering angle relative to the incident radiation. While the back scattered fraction is a combination of a $B_1(\theta) \propto \cos(\theta - \pi)$ and a Gaussian law $B_2(\theta) \propto \exp[-\frac{1}{2}(\theta-\pi)^2 / \rho^2]$, with ρ being a measure for the surface roughness of the aerosol layer deposited on the filter. The partitioning between these two component depends on the optical properties of particles collected in the fiber filter. Measuring simultaneously the light intensity at three detection angles, one in forward hemisphere ($\theta_0 = 0$) and two in the backward ($\theta_1 = 165°$ and $\theta_2 = 130°$), it is possible to fully determine the irradiances at all angles. The angle choice was made in order to obtain the highest possible resolution. Figure 3.10 provides a representation of MAAP geometry.

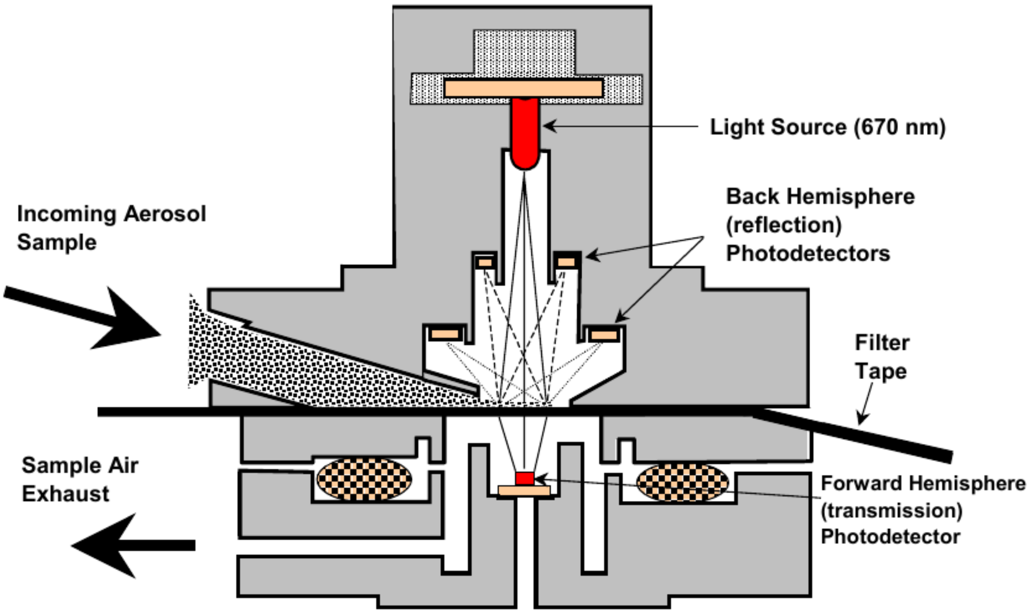

Figure 3.10: Schematic view of the MAAP measurement geometry.

The measured irradiance as a function of θ is then related to particle optical parameters using a radiative transfer method initially developed by Hänel (1994) and then modified for this purpose by Petzold and Schonlinner (2003). It is based on a two-stream approximation in the radiative transfer by Coakley and Chylek (1975). This instrument is expected to provide the absorption coefficient at 637 nm with an accuracy of 15 % (Petzold et al., 2005; Müller et al., 2011), which directly applies to the reported absorption coefficients. This instrument, although not carrying out an analysis on a wide spectrum of wavelengths, is the most accurate among those available for the measurement of the absorption coefficient and has been used in this thesis as a reference for correction the others.

3.3.3 Aethalometer (MAGEE Scientific model AE31)

The Aethalometer is a filter based instrument for measuring the absorption coefficient of aerosol particles and BC mass concentration, at seven different wavelengths spanning infrared to UV range. In this research data from two different models of Aethalometer have been analyzed, AE31 and AE33, both with multiwavelength capability (370nm, 470nm, 520nm, 590nm, 660nm, 880nm, 950nm). The value of the absorption coefficient is obtained by measuring only the attenuation (ATN) produced by particles collected on a quartz filter.

The filter is illuminated by a light source from one side, with the detectors located on the other side, as depicted in figure 3.11. Light is transmitted through a pristine part of the filter with an intensity I_0. The light that traverses the loaded part is instead transmitted with an intensity I. The Aethalometer calculates, and reports, filter attenuation (ATN) as described:

$$ATN = -100 \cdot \ln(I/I_0). \tag{3.6}$$

The attenuation coefficient is then defined as:

$$b_{ATN} = \frac{A}{Q \cdot \Delta t} \frac{\Delta ATN}{100}. \tag{3.7}$$

In equation 3.7, A is the filter spot size area, Q is the sample flow rate, and Δt is the time between the light intensity measurements. The term ΔATN is the change in ATN over the time Δt set to 2 minutes. When the fibre filter is loaded with aerosol, and the transmission of light through the filter has dropped too much, the filter spot needs to be changed. In the Aethalometer, filter changes can be set to occur automatically at an ATN value set by the operator. Alternatively, the filter can be set to change after a given time. The data can then be mediated over a longer period that can be set by the operator. A low collection time results in noisy data in particular for very pristine sites, while a longer averaging time will reduce noise. In this study the averaging time was set to 10 minutes at BO and 5 minutes at SPC and MC. The filter was instead changed every two hours at MC and when ATN reaches a value of 50 and 120 at BO and SPC respectively.

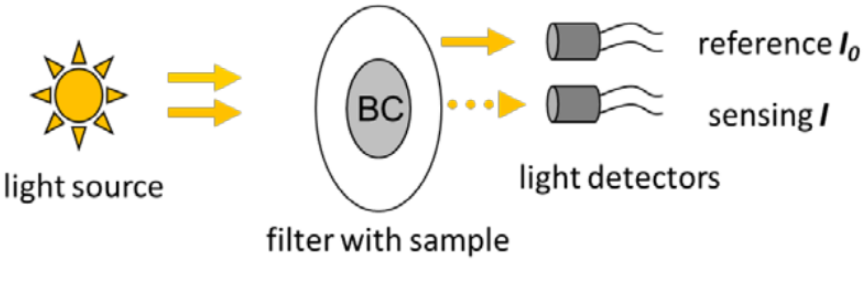

Figure 3.11: Schematic representation of Aethalometer, model AE31, measurement geometry.

The attenuation coefficient measured by the Aethalometer may differ significantly from the true aerosol absorption coefficient of particles in the airborne state. The main sources of uncertainty in this parameter are: the multiple scattering at the filter fibers, that enhances the optical path leading to more light absorption and the so called "loading effect", that is a gradual reduction in the instrumental response while the aerosol deposit density increases.

The filter matrix has its characteristic optical depth, multiple scattering occurs within the filter fibers, so that the intensity of light is consistently attenuated after passing through the pristine filter layer (figure 3.12.b). The light intensity used as reference is not then the intensity of the source, but the already attenuated signal due to filter presence. Moreover, the loading of non-absorbing material leads to an increase of the backscattered light, which induces an apparent greater reflectance of the filter (figure 3.12.c). The percentage of scattering that is interpreted as absorption is anyway negligible and quantified as less than 5 % (Bond et al., 1999; Weingartner et al., 2003). This effect depends on the asymmetry parameter of the deposited particles which is function of particle diameter and wavelength of incident light. Presence of non-absorbing particles became important when absorbing matter is also loaded on the filter and is parametrized in function of the single scattering albedo (Collaud Coen et al., 2010). Scattering due to particles increases the optical path of light leading to higher probability of encountering and embedded absorbing particle (figure 3.12.d). Multiple scattering of the filter matrix leads to similar effect. The increase of optical path leads to overestimation of absorption. This absorption enhancement can be partially compensated by the "shadowing" effect, which is induced by the loading of absorbing aerosol on the filter. The lately loaded particles will absorb light, reducing the optical path for a loaded filter, decreasing the probability of absorption by previously loaded particles. Particle size determines the vertical distribution of particles in the filter; large particles have smaller mobility and are more likely to be embedded in the superficial layer of the filter (Nakayama et al., 2010). Under this condition back scattering and absorption is dominated by superficial non-absorbing and absorbing particles.

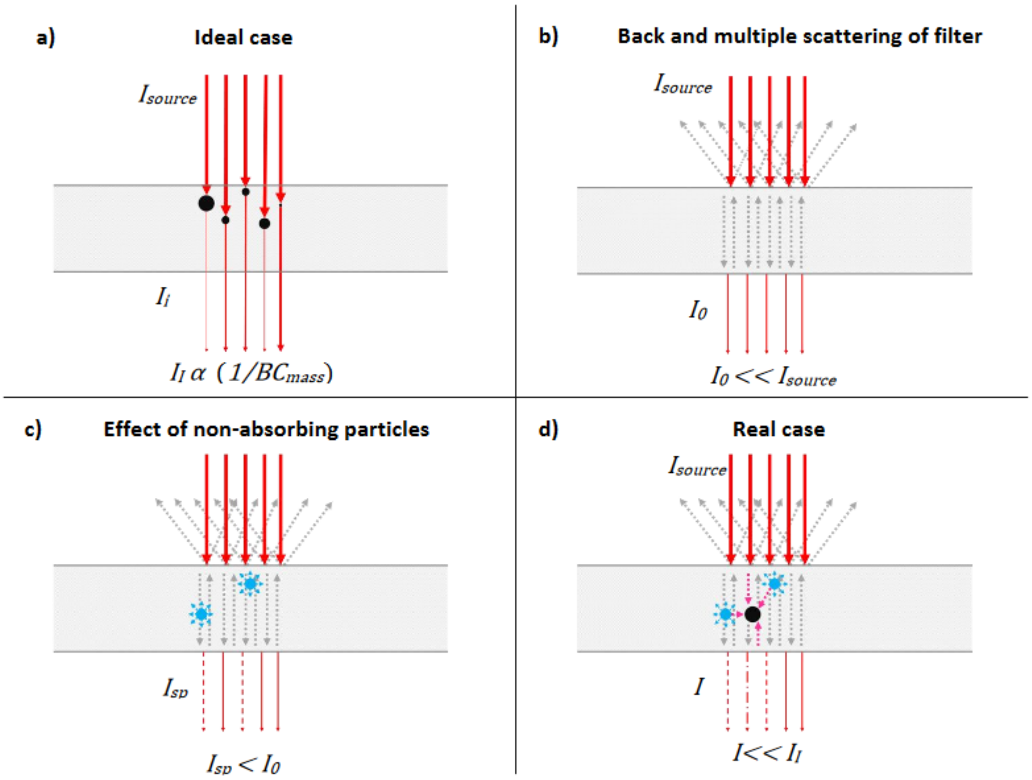

Figure 3.12: Schematic of optical processes occurring in a filter matrix. a) Ideal case where the variation of ATN is proportional only to the amount of absorbing material loaded on the filter. b) Effective back scattering and multiple scattering (greydotted lines) of the filter matrix in absence of loaded aerosol. c) Presence of non-absorbing particles (blue spheres), induce additional scattering (dotted blue lines). Back scattering can be misunderstood as absorption and lead to a decrease in transmitted light. d) Filter loaded with absorbing and scattering aerosol. Multiple scattering induced by filter matrix and non-absorbing particles increases the optical path of light enhancing the probability of light absorption (pink dotted line)by absorbing particles (black spheres).

There are various corrective procedures in the literature. The one used to process the data obtained by the AE31 in this measurement campaign is that described in Weingartner et al., 2003.

In this method two calibration factor C_0 and R(ATN) are used to convert the

Aethalometer attenuation measurements to "real" absorption coefficient with the following relation:

$$b_{abs} = b_{ATN} \frac{1}{C_0 \cdot R(ATN)}. \tag{3.8}$$

The R(ATN) parameter corrects for all effects caused by accumulation of particles on the filter. The curve proposed by Weingartner for R(ATN) is a linear function of ln(ATN):

$$R(ATN) = (\frac{1}{f} - 1)\frac{ln(ATN) - ln(10\%)}{ln(50\%) - ln(10\%)} + 1, \tag{3.9}$$

where the parameter f can be expressed as a function of the single scattering albedo:

$$f = a(1 - SSA) + 1, \tag{3.10}$$

with a = 0.86. $b_{ATN}^{loading\ corrected}$ is then defined as b_{ATN} divided by R(ATN) determined in this way. The C_0 parameter corrects for the enhancement of absorption due to multiple scattering of light at the filter. It does not depend on the aging time of the particles but could be influenced by the presence of volatile compounds that condense on the filter at every filter change. This parameter is not simple to evaluate because it requires the proper knowledge of b_{abs} of particles in the airborne state. Typically a C_0 parameter is estimated comparing Aethalometer data with that obtained through a reference method. In this research the reference instrument chosen is the MAAP.

3.3.4 Aethalometer (MAGEE Scientific model AE33)

The Aethalometer AE33 is based on the same physical principle of AE31. It is a filter base method that measures the attenuation due to particles embedded in fibers of a quartz filter, at the same seven wavelengths of AE31. The difference between the two models is that AE33 provides an automatic correction for the loading effect and a real time determination of correction parameters for all the seven wavelengths, measuring simultaneously the attenuation through two sample spots, with different rates of accumulation. Both spots derive their samples from the same input air stream.

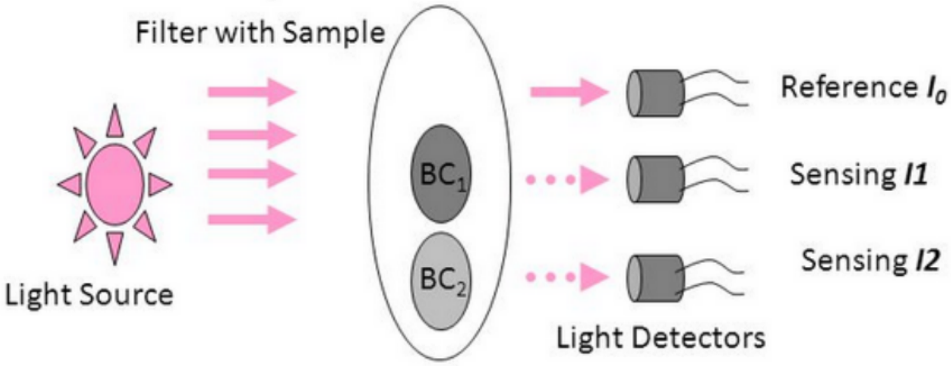

Figure 3.13: Schematic representation of Aethalometer, model AE33, measurement geometry.

The underlying assumption of this method is that the relation between b(ATN) and b(0) at zero loading is linear and can be expressed as a function of a corrective parameter k and ATN as follows:

$$b_{ATN}(ATN) = b_{ATN}(0) \cdot (1 - k \cdot ATN), \tag{3.11}$$

with k dependent on environmental conditions and particle's characteristics. Attenuation and b_{ATN} can be measured through the same processes and with the same equation previously described for AE31, but for two spots rather then one, as depicted in figure 3.13. The parameter k and b$_{ATN}(0)$ can instead be calculated, for each time step, from the following system of equations:

$$b^{1}_{ATN} = b_{ATN}(0) \cdot (1 - k \cdot ATN^{1}) \tag{3.12}$$

$$b^{2}_{ATN} = b_{ATN}(0) \cdot (1 - k \cdot ATN^{2}). \tag{3.13}$$

They are then used to provide b$^{loading\ corrected}_{ATN}$(ATN). This procedure corrects for the loading effect but it doesn't take into account multiple scattering. This effect can be then corrected through a comparison with a reference method as for AE31.

3.3.5 Variability of filter based instruments

The variability of the absorption coefficient derived by seven MAAPs, four Aethalometers (7-wavelengths model) and six PSAPs (3-wavelength model) was investigated by Müller et al (2011), providing an evaluation of their repeatability. The so called unit-to-unit variability is defined by the coefficient of variation, which is the ratio of the standard deviation and the average absorption coefficient. It was calculated as the slope of the fitting line in the scatter plots showed in figure 3.14.

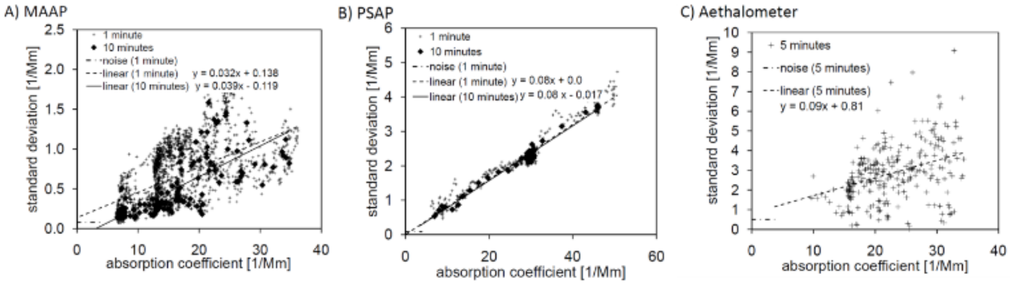

Figure 3.14: Unit-to-unit variability (standard deviation of several instruments) versus absorption coefficient for (a) MAAP at 637 nm;(b) PSAP at 530 nm;(c) Aethalometer at 660 nm. PSAP and MAAP data are shown for the highest time resolution of one minute and for an averaging time of ten minutes. Aethalometer data are shown for an averaging time of 5 min. The noise level is indicated as horizontal line. From Müller et al.(2011).

Considering only simultaneous measurements performed with a set of identical instruments, the most common causes of unit-to-unit variability are systematic errors as inaccuracy in sample flow and in the loading spot area. The unit-to-unit variability of MAAP was of 3%. Despite the fact that the Aethalometer showed a coefficient of variation of 9%, its spread (figure 3.14 c) was considerably larger than PSAP. The high instrumental noise of the Aethalometer partly explains the spread. Noise in the Aethalometer was quantified in 0.3-0.8 1/Mm, while MAAP and PSAP showed noise of 0.22 and 0.08 1/Mm respectively. The two values reported for Aethalometer refer to instruments having a small spot area, high sensitivity for clean environments, and a large area, extended range for polluted environments.

3.3.6 Thermo-optical analysis

Among all the existing thermo-optical protocols for EC and OC mass concentration determination, the one used in this study is the EASAAR_2. It is a thermo-optical transmittance method, selected as the standard method for the ACTRIS research infrastructure, developed in the context of the EU-project EUSAAR, described in Cavalli et al. 2016, which integrates 20 stations with the objective of harmonizing aerosol measurements of interest to air quality and global climate. The instrument used for this analysis is the Sunset Laboratory Dual-Optical Carbonaceous Analyser (figure 3.15) and the procedure can be divided into three main parts. In the first, the sample is

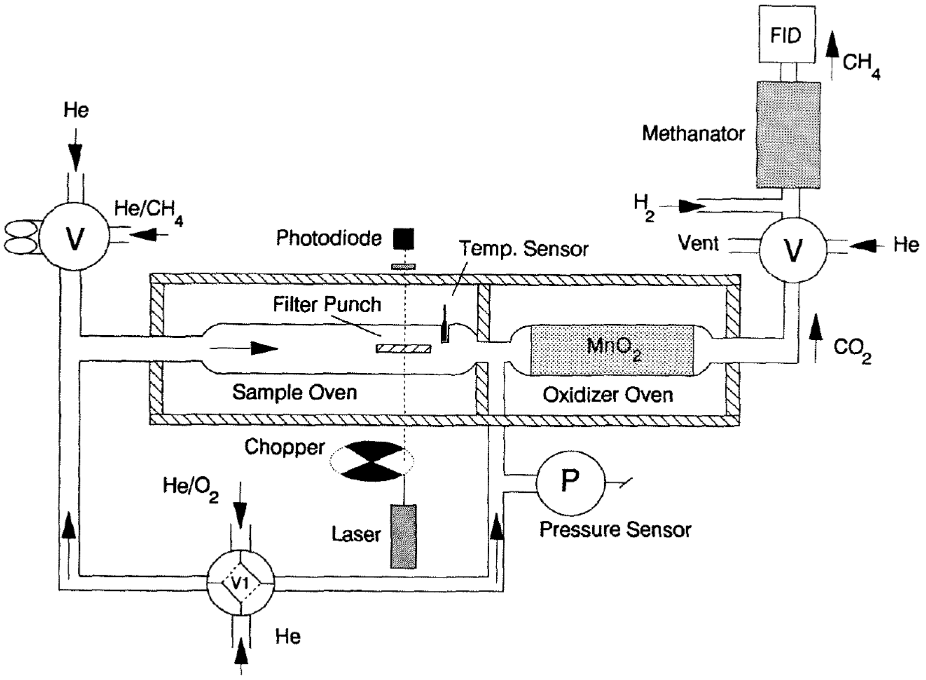

Figure 3.15: Schematic representation of Sunset Laboratory Dual-Optical Carbonaceous Analyser.

heated in an oxygen-free atmosphere to four increasing temperatures listed in table 3.2. This heating removes all the organic carbon excluded the pyrolytical carbon produced. The volatilized part of organic carbon is transported by a constant flow of helium to an oxidizer that follows the sample owen, where it is converted to CO_2. Then the flow is directed to a methanator oven where CO_2 is converted in methane detected by a flame ionization detector. In the second step, the sample is cooled to 500 °C and the flow of helium is converted to a 2% oxygen/helium mixture. The sample is then heated to 850 °C to oxidize the EC, both the original and that produced by pyrolysis. The carbon dioxide is then converted to methane and detected by a flame ionization detector as in the first step. At the end a known volume and concentration of methane is injected into the sample oven to calibrate the sample and check the operation of the instrument.

Samples from SPC and BO have been analysed at ARPAE laboratoratory, based in Ravenna, while MC samples were sent to CNR-ISAC Lecce for thermos-optical analyses. Both Laboratories participated in the European Center for Aerosol Calibration (ECAC) intercomparison, in the framework of ACTRIS Research Infrastructure. The uncertainties of this analysis have been estimated from the two laboratories, performing independent measures on fragments of the same filters. The results show a percentage uncertainty of 3.4 % for BO and SPC filters and 8 % with a bias of 2 % for MC filters.

Step	T °C	time s
H_e 1	200	120
H_e 2	300	150
H_e 3	450	180
H_e 4	650	180
H_e/O_2 1	500	120
H_e/O_2 2	550	120
H_e/O_2 3	700	70
H_e/O_2 4	850	80

Table 3.2: Heating cycles of EUSAAR_2 procedure.

3.4 Data analysis

3.4.1 Absorption and scattering coefficients

The scattering coefficient was derived from data provided by the integrating Nephelometer with a time resolution of 1 minute, for all the three sites. To avoid uncertainties due to high humidity values and to eliminate outliers, we removed data corresponding to humidity higher than 60% and applied the following statistical method:

$$x^{reteined} = |x - MA(x,\tau)| < c \cdot MSD(x,\tau), \tag{3.14}$$

where MA is the moving average of the data on a time interval of three hours and MSD the moving standard deviation on the same period. The choice of c was made after a comparison between different parameters in order to eliminate the most evident outliers in the time series, by excluding less than 3 % of the values. This does not significantly influence the statistical parameters.

The values were then corrected for the truncation effect described in section 3.3.1, using the equation 3.4, with a SAE derived from:

$$SAE(\lambda_1/\lambda_2) = -\frac{\ln(b_{sca}(\lambda_1)/b_{sca}(\lambda_2))}{\ln(\lambda_1/\lambda_2)}. \tag{3.15}$$

SAE (450/550) was used for correcting b$_{sca}(450nm)$, SAE (450/700) and SAE (550/700) for b$_{sca}(550nm)$ and b$_{sca}(700nm)$ respectively. To allow comparison with MAAP values, the b$_{sca}(637nm)$ was then calculated through the equation:

$$b_{sca}(637nm) = b_{sca}(550nm)(\frac{637}{550})^{-SAE(550/700)}. \tag{3.16}$$

The absorption coefficient was obtain with three different instruments MAAP, Aethalometer model AE31 and Aethalometer model AE33. MAAP, AE31 and AE33 at MC and SPC and MAAP and AE31 at BO. The influence of outliers was reduced by applying the same statistical method as for Nephelometer data. We considered the MAAP free from errors due to the loading effect and the multiple scattering and therefore we did not apply corrections to the data supplied by it. Initially it was thought that this instrument operated at a wavelength of 670 nm, but it was then observed that the true wavelength is equal to 637 ± 1 nm. For this reason, the absorption coefficient determined by the MAAP firmware must be increased by 5% to obtain the correct absorption coefficient. This correction has been applied to the measured absorption coefficient values. The b$_{abs}$ has been previously calculated as the product of the BC mass concentration in output from the instrument, with a time resolution of 1 minute, and 6.6 m^2 g^{-1}, which is the assumed MAC applied by the firmware.

The Aethalometer model AE31 is instead subject to both sources of error and its data have therefore been processed in a multi-step correction procedure. BC mass concentration values, measured at different time resolutions for each site, every 10 minutes at BO and every 5 minutes at SPC and MC, were firstly converted in b$_{ATN}$ values using the assumed MAC listed in table 3.3 for each λ.

	Aethalometer						
	370 nm	470 nm	520 nm	590 nm	660 nm	880 nm	950 nm
MAC$_{BC}$ (m^2 /g)	39.5	31.1	28.1	24.8	22.2	16.6	15.4

Table 3.3: MAC$_{BC}$ values implemented in Aethalometer AE31, AE33 for the BC mass concentration determination at different wavelengths.

Then we correct b$_{ATN}$ at each λ for the loading effect, using the relation 3.9. The f parameter were derived as a monthly average of f at each time step, calculated from equation 3.10. The values of SSA needed in this equation was previously obtained from b$_{abs}$ and b$_{sca}$ measured by MAAP and Nephelometer, through the following relation:

$$SSA = \frac{b_{sca}^{Nephelometer}}{b_{abs}^{MAAP} + b_{sca}^{Nephelometer}}. \tag{3.17}$$

The correction for multiple scattering effect was then performed comparing the hourly average of b$_{ATN}^{loading\ corrected}$(637 nm), calculated by the equation:

$$b_{ATN}^{loading\ corrected}(637nm) = b_{ATN}^{loading\ corrected}(590)(\frac{637}{590})^{\mathrm{AAE\ (590/660)}}, \tag{3.18}$$

and hourly means of b$_{abs}$ measured by MAAP. Assuming this relation between b$_{ATN}^{loading\ corrected}$ and b$_{abs}^{MAAP}$:

$$C_0 = b_{ATN}^{loading\ corrected} \ / \ b_{abs}^{MAAP}, \tag{3.19}$$

C$_0$ can be derived from the slope of a linear fit between them. This value can be then multiplied to b$_{ATN}^{loading\ corrected}$ at each λ, to derive b$_{abs}^{AE31}$.

The Aethalometer model AE33 provides automatically derived b$_{ATN}^{loading\ corrected}$ at each wavelength which need a correction only for multiple scattering. This is done using the same procedure described for AE31.

The uncertainty associated to Aethalometer derive from a combination of that of measured b$_{ATN}$ and those due to correction procedure. On b$_{ATN}$ values that suggested by the instrument manual which is 10 %. C$_0$ parameter for multiple scattering correction is then the major source of uncertainty related to the final value. It was observed that it varies by about ±25% (1σ) for different aerosol types (WMO, 2016; Collaud Coen et al., 2010; Müller et al., 2011). The final uncertainty on AE31 and AE33 values derive from the propagation of the uncertainties on b$_{ATN}^{loading\ corrected}$ values and this 25 % associated to C$_0$.

The scattering and absorption coefficients at different wavelengths were then used to derive the scattering (SAE) and absorption (AAE) Angstrom exponents over a wide spectral region, with the following relations.

$$SAE = -\frac{\ln(b_{sca}(450)/b_{sca}(700))}{\ln(450/700)}, \tag{3.20}$$

$$AAE = -\frac{\ln(b_{abs}(470)/b_{abs}(880))}{\ln(470/880)}. \tag{3.21}$$

These are useful parameters to derive information on aerosol composition as described in section 1.2.1. One of possible technique, applied in this study, to do this is the construction of the Angstrom matrix (figure 3.16) as described in Cazorla et al. (2013). Uncertainties in derived parameters SAE, AAE and SSA were calculated by an error propagation through the following formulae:

$$\Delta AAE = \frac{1}{\ln 470/880} \cdot \sqrt{(\frac{\Delta b_{abs}(470)}{b_{abs}(470)})^2 + (\frac{\Delta b_{abs}(880)}{b_{abs}(880)})^2}, \tag{3.22}$$

$$\Delta SAE = \frac{1}{\ln 450/700} \cdot \sqrt{(\frac{\Delta b_{sca}(450)}{b_{sca}(450)})^2 + (\frac{\Delta b_{sca}(700)}{b_{sca}(700)})^2}, \tag{3.23}$$

$$\Delta SSA = \frac{1}{(b_{abs} + b_{sca})^2} \cdot \sqrt{(b_{abs}\Delta b_{sca})^2 + (b_{sca}\Delta b_{abs})^2}, \tag{3.24}$$

assuming negligible errors in λ compared to the other measured values. Those on b$_{abs}$ and b$_{sca}$ at 637 nm were obtained through:

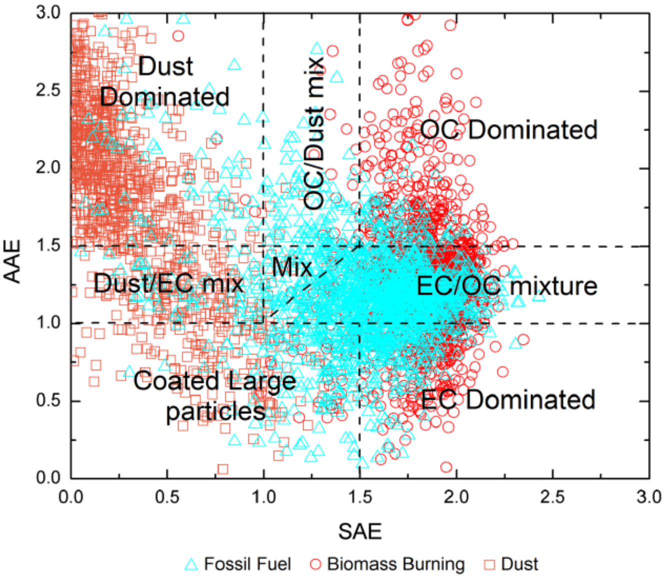

Figure 3.16: Division of the Absorption Angström Exponent vs. Scattering Angström Exponent Absorption space, the Angström matrix, overlapped with the AERONET measurements from stations with a dominant sources (fossil fuel in cyan triangles, biomass burning in red circles or dust in orange squares).

$$\Delta b_{abs}(637) = \sqrt{(\Delta b_{abs}(590)\cdot(\frac{637}{590})^{-AAE(590/660)})^2 + (\Delta AAE(590/660)\cdot b_{abs}(590)\cdot \cdot \ln(637/590)\cdot(\frac{637}{590})^{-AAE(590/660)})^2}, \tag{3.25}$$

$$\Delta b_{sca}(637) = \sqrt{(\Delta b_{sca}(550))\cdot(\frac{637}{550})^{-SAE(550/700)})^2 + (\Delta SAE(550/700)\cdot b_{sca}(550)\cdot \cdot \ln(637/550)\cdot(\frac{637}{550})^{-SAE(550/700)})^2}, \tag{3.26}$$

3.4.2 EC mass concentration (m$_{EC}$) and MAC derivation

The EC mass concentration was quantified using the thermo-optical technique with the EUSAAR-2 protocol. Filter sample were collected at MC over different time period and in various times of the day, in order to distinguish between diurnal and nightly concentration. At the sites of BO and SPC, the samples were collected in order to be representative of the daily average. M$_{EC}$ was used in combination with the aerosol absorption coefficient measured by all the available instruments, for the determination of the mass absorption cross section (MAC) at the wavelength of 637 nm. Assuming that at this wavelength the absorption is mainly affected by BC, the definition of MAC can be written as:

$$MAC = \frac{b_{abs}}{m_{EC}}. \tag{3.27}$$

The absorption coefficient were averaged over the time intervals of the filter samples for the thermo-optical analysis, in order to obtain comparable pairs of m$_{EC}$ and b$_{abs}$, before calculating the corresponding MAC values. The uncertainty associated to these values has been derived by propagating that of EC and b$_{abs}$ with the relation:

$$\frac{\Delta MAC}{MAC} = \sqrt{(\frac{\Delta b_{abs}}{b_{abs}})^2 + (\frac{\Delta EC}{EC})^2}. \tag{3.28}$$

Chapter 4

Results and discussion

4.1 Meteorological characterization

July 2017 was a particularly hot and dry month throughout all the region of interest, with temperatures above expectations and very low rainfall, especially on the hills where they were among the lowest since 1961. Maximum temperatures were everywhere between one and two degrees above the above the climatological averages and rainfall was about 60% less. The figure 4.1 illustrates the anomalies of these variables compared to the climate average over the period 2001-2015. Those of maximum, minimum, average temperature and precipitation calculated from the averages over the period 1961-1990 were instead +3.2, +1.5, +2.1 degrees and -34 mm respectively.

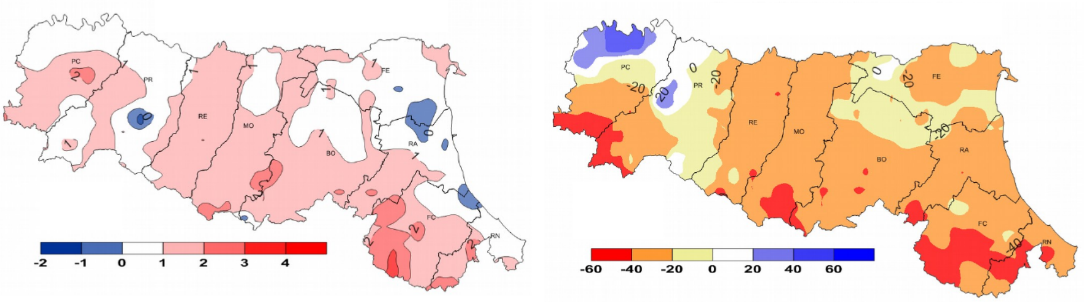

(a)

(b)

Figure 4.1: Temperature anomalies (a) and precipitation (b) compared to the climate average over the period 2001-2015, recorded in July 2017 in Emilia Romagna (monthly agroclimatic bulletin drawn up by the hydro-meteo-climate service of ARPAE).

Figure 4.2 also show the weekly averages of 500-hPa geopotential height, starting from the 3rd of July 2017, computed from the NCEP/NCAR reanalyses. This field describes the large-scale circulation over the European territory.

The dominant feature of the whole month was a stronger than normal cyclonic circulation over Northern Europe (negative anomaly of monthly averaged 500-hPa geopotential height computed over the 1981-2010 reference climate, not shown). South of this area, over Southern Europe and the Mediterranean basin, the flow was westerly and mainly associated with anticyclonic systems, with the higher geopotential height values observed over North-Western Africa. However, some variation in the mean westerly flow is observed along the month. In particular, during the 1st and 3rd week, a southern component affects the circulation especially over the western and central portion of the Mediterranean basin. This circulation, not observed on the other 2 weeks, was also associated with warm air.

As an example, figure 4.3 shows the synoptic situation at 18 UTC of 21 Jul 2017, as forecast in the BOLAM-MOLOCH run of the same day. Upstream of the baroclinic wave featuring the relatively strong cyclone over Ireland, a warm tongue of air coming from Africa (thus initially dry) crosses the Western Mediterranean towards the Balkans. As a consequence of the warmer mean temperature of these airmasses, higher geopotential height are observed; however such warm air advection is associated with moderate south-westerly flow, as shown in the wind field forecast at 850 hPa (mid-low torposhere) by the high-resolution MOLOCH model.

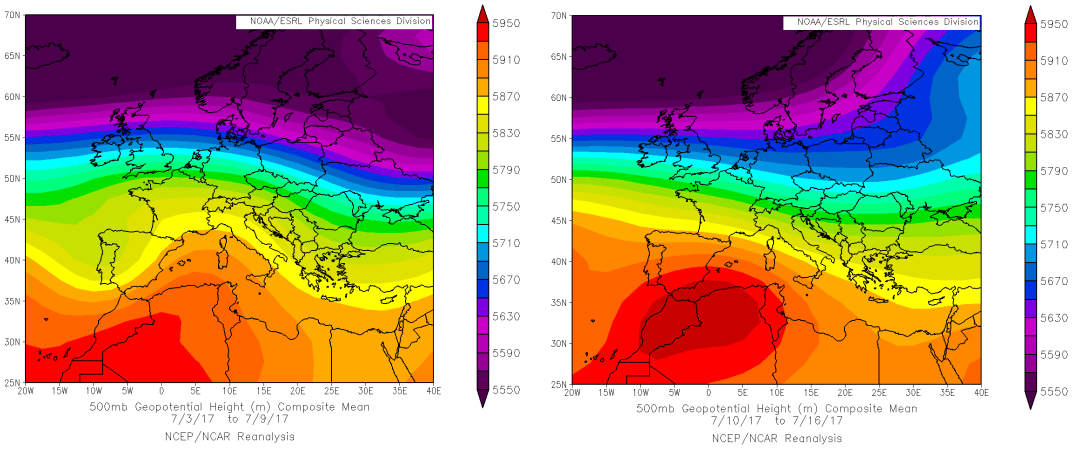

(a) *Week 1* (b) *Week 2*

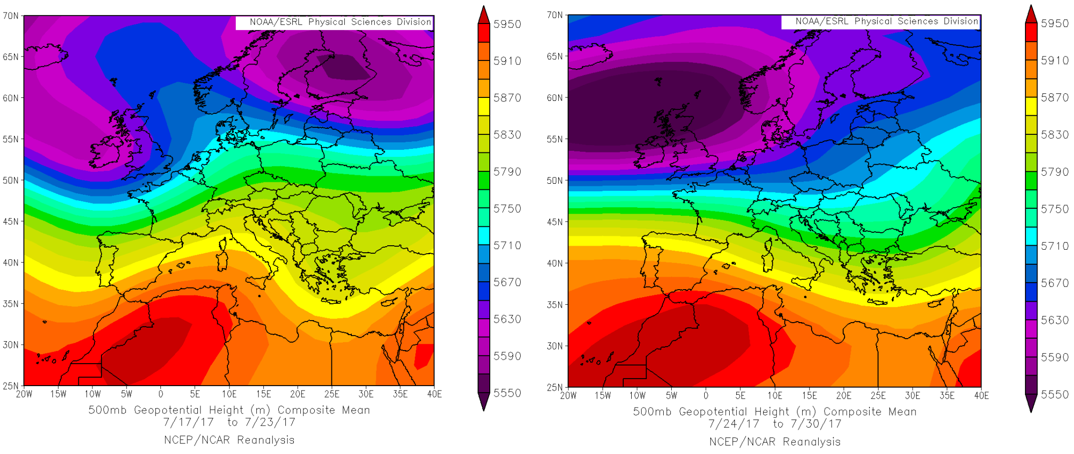

(c) *Week 3* (d) *Week 4*

Figure 4.2: Weekly averages of 500-hPa geopotential height, starting from the 3rd of July 2017, computed from the NCEP/NCAR reanalyses.

Specific weather conditions at the three sites studied, for the analyzed period, are summarized below. The temperature and humidity trends are shown in the graphs in the figure 4.4.

At BO, the temperature fluctuates by about 10 degrees between night and day, with daytime values often above 30 degrees and never below 25. The coolest periods were recorded between 14 and 18 and between 25 and 27. The humidity is very variable during the month, with values ranging between 30 % and 80 % and an average of 52 %. The SPC site is characterized by very wide daytime variations in both variables. Humidity values span from 20 to 90 % with an average of 60 %. The temperature is very similar to BO but with larger variations between day and night. The average value is 24.8 °C. The values recorded at the MC vary much less between day and night but show larger differences at different times of the month. The average temperature is 12.6 °C, with very low values at the beginning of the month and between 16 and 17 July.

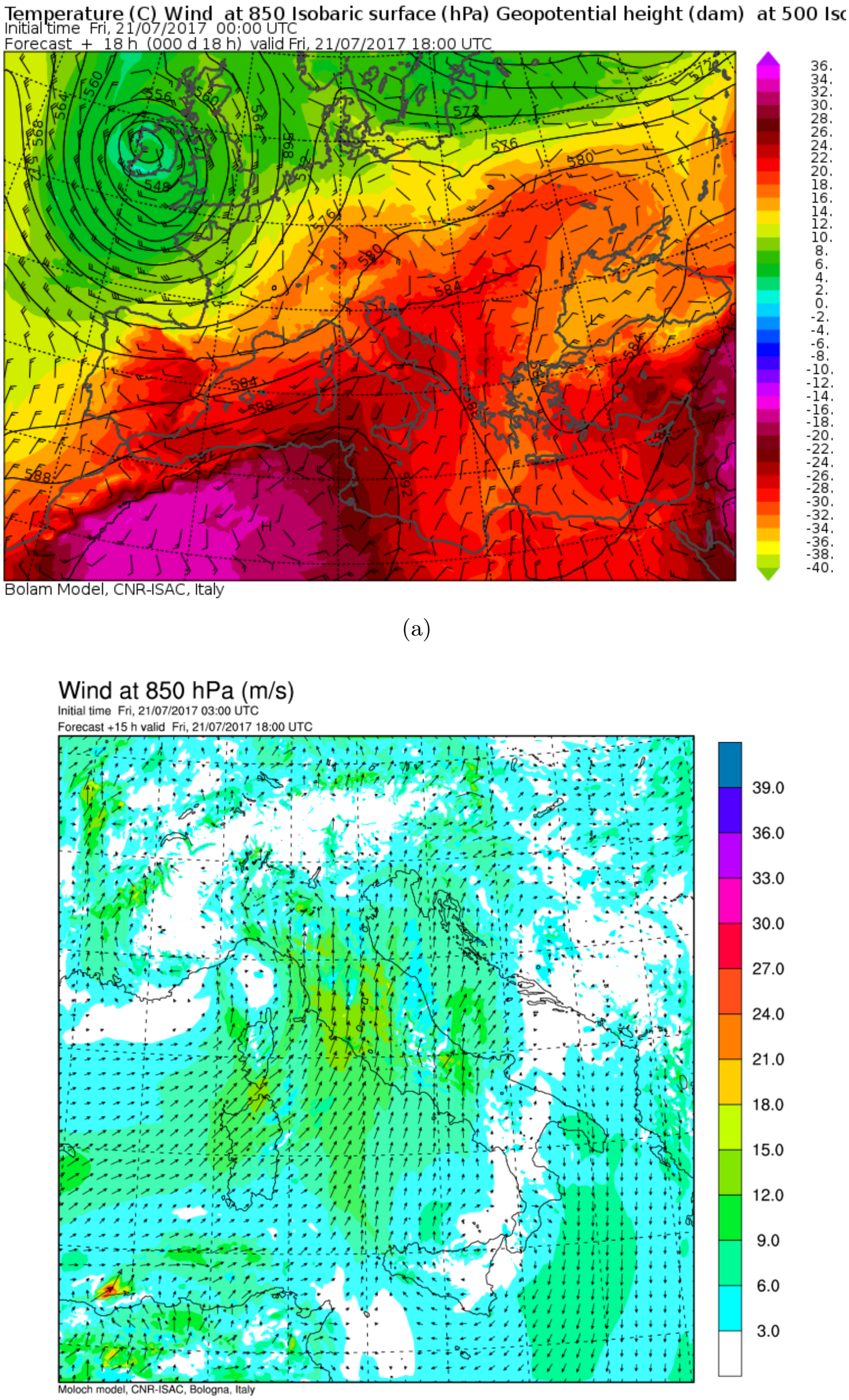

(a)

(b)

Figure 4.3: Synoptic situation at 18 UTC of 21 Jul 2017, as forecast in the BOLAM-MOLOCH run of the same day.

Maximum values around 20 °C were recorded on the 8th, 9th, 19th and 20th and in the last part of the month. The humidity was very variable with an average of 64%.

The only rains recorded were: 10 mm on 12 July at SPC and two short periods on 11 July at BO, with values around 15-20 mm.
The SPC site was characterized by rather weak winds with an average speed of 1.7 m/s, distributed in all directions. The one with the highest frequency was the south-east towards Ravenna, while the ones with the lowest frequency were the south and south-west (from Bologna, Imola and Modena).

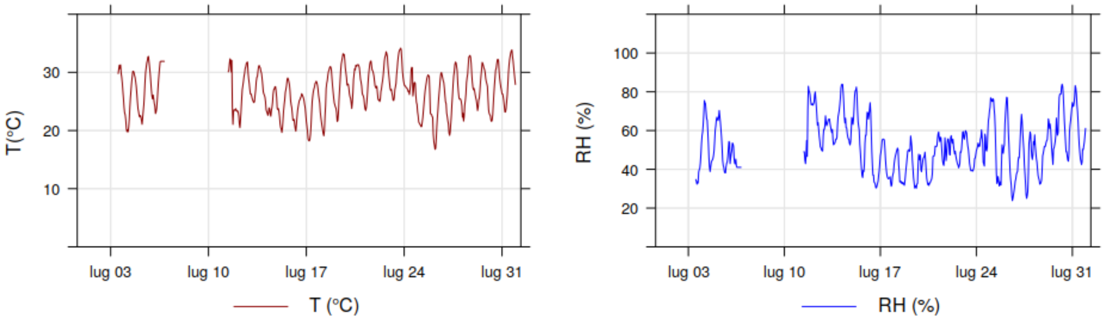

(a) *Temperature (BO)* (b) *Humidity (BO)*

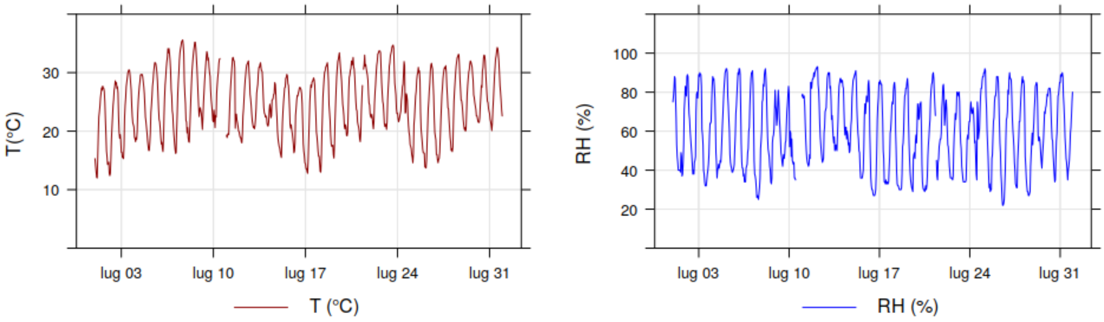

(c) *Temperature (SPC)* (d) *Humidity (SPC)*

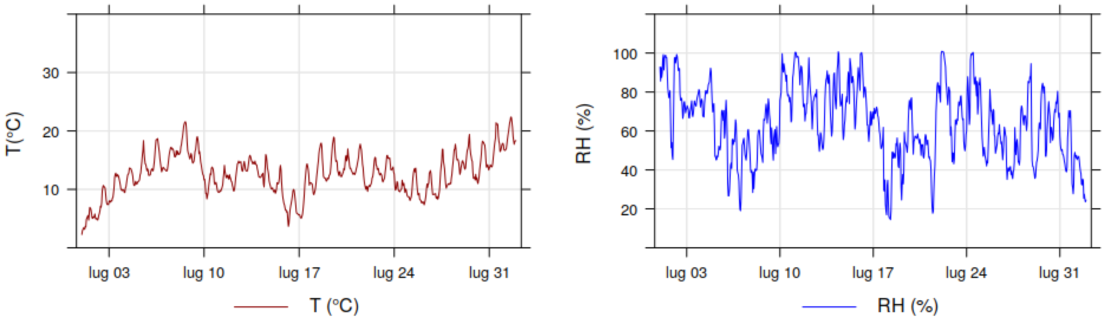

(e) *Temperature (MC)* (f) *Humidity (MC)*

Figure 4.4: Temperature and humidity variability over the month for all the three sites.

At BO there was an average of 2.36 m/s. Winds from the east and west are more frequent and more intense, while winds from the south (from the city centre) and from the north in the direction of the largest and busiest road, are less frequent or very weak respectively. At the MC the intensity is much higher with an average of 4.5 m/s and the prevailing direction is the south-east towards the Tyrrhenian Sea. The figure 4.5

depicts this situation through wind roses for each site.

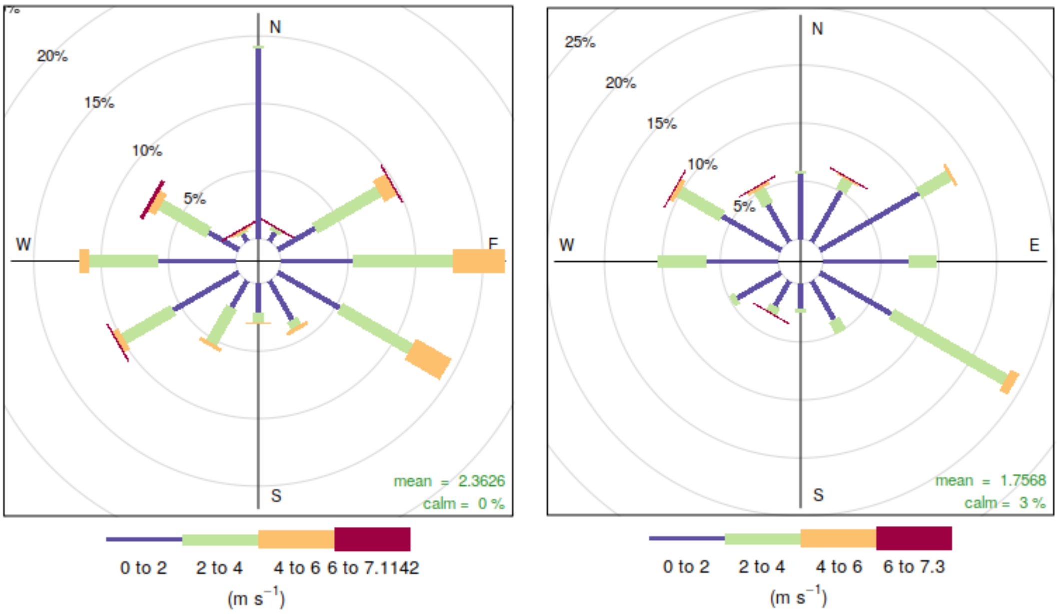

(a) *BO* (b) *SPC*

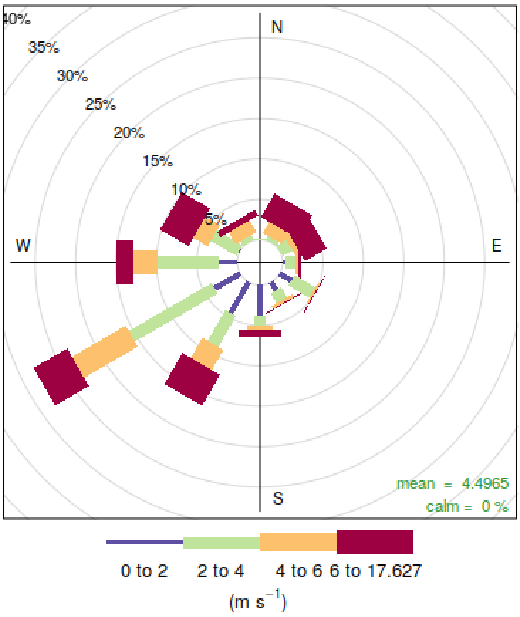

(c) *MC*

Figure 4.5: Wind roses derived from wind speed and wind direction data measured during all month, in the three sites.

4.2 BC mass concentrations

The optical instruments for BC determinations directly measures the light attenuation or absorption coefficient, but for practical reasons instead of giving as output the value of the physical parameter really measured, i.e. the absorption coefficient in the case of MAAP and the attenuation coefficient for Aethalometers, provide an estimate of BC mass concentration. The main reason for this is that BC is the most interesting quantity for air quality agencies, especially for investigate the effects of combustion pollution on human health through epidemiological studies. For deriving the BC concentration a default MAC value is set in every instrument: 6.6 m^2/g for MAAP and those reported in table 3.3 for Aethalometers.

Table 4.1 lists the monthly averages of BC mass concentration measured by all available instruments in the three sites, while the time series of the hourly mean are shown in figure 4.6, 4.7 and 4.8.

However, these values are subject to large uncertainties mainly because they are derived from the ratio between the measured b_{abs} or b_{ATN} and a coefficient set in the instrument as MAC. This is derived from comparison with other measurement techniques under controlled conditions, but unfortunately there is not yet one that is able to accurately measure the mass of BC to be used as a reference, without any interference.

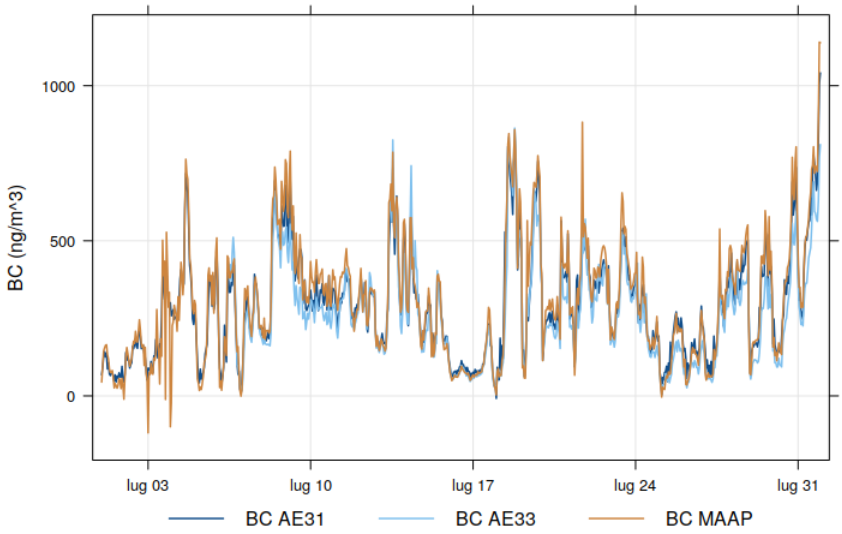

Figure 4.6: Time series (UTC+1) of BC mass concentration obtained by all instruments at MC.

In the natural environment, the aerosol components are often mixed, externally or internally and it is difficult to identify the possible interferences. The observed b_{abs} is representative of BC and the various components externally and internally mixed with it, and the corresponding MAC being variable as the composition and mixture of the sampled aerosol change, is not known. If particles were only pure BC or if it was possible to isolate the absorption due to the BC alone, a MAC equal to 7.5 ± 1.2 m^2/g (Bond and Bergstrom 2006) could be used, but this is not the case. Unfortunately, there is still no method for isolating absorption due to BC alone and aggregates are rarely emitted as pure BC, but are encapsulated, or "mixed," with other aerosol species.

Basically, the mixing state of BC particles is function of particle age and other factors. BC particles that have traveled for long periods before reaching a sampling site will have had ample opportunity to gather layers of coating. Freshly emitted BC containing particles will have had less opportunity to gather a coating beyond that imparted upon emission. Differences in mixing state are related to particle history.

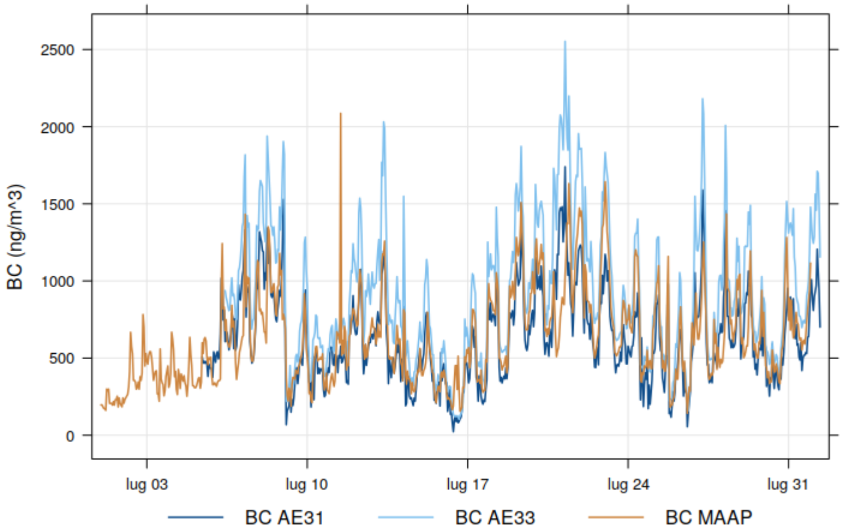

Figure 4.7: Time series (UTC+1) of BC mass concentration obtained by all instruments at SPC.

These differences may change MAC substantially. For example increases in absorption by coating can be described in terms of “absorption amplification".

	Cimone			St. Pietro Capofiume			Bologna	
	MAAP	AE31	AE33	MAAP	AE31	AE33	MAAP	AE31
mean (ng/m^3)	289	292	274	594	639	926	952	1037
sd (ng/m^3)	211	188	178	286	429	505	633	673

Table 4.1: Mean and standard deviation of BC (ng/m^2) for all instruments in their whole period of measure.

Beyond the great uncertainties these measures can be used to compare different sites and to observe the trend during the month. What we can see from a quick analysis of these time series is that the various instruments placed in the same environment, are able to measure comparable average concentrations and standard deviations and to follow similar trends, with the exception of the AE33 placed at SPC which tends to overestimate the mass concentrations with respect to the other two instruments.

In the following paragraphs, the various instruments will be compared in more detail and we'll derive the correction coefficients that allow to transform the attenuation values measured by the Aethalometers into absorption values. In addition, an evaluation of MACs and their variability at different sites will be provided, calculating this parameter from the ratio between the optically measured absorption coefficients and mass of EC measured with the thermo-optical method.

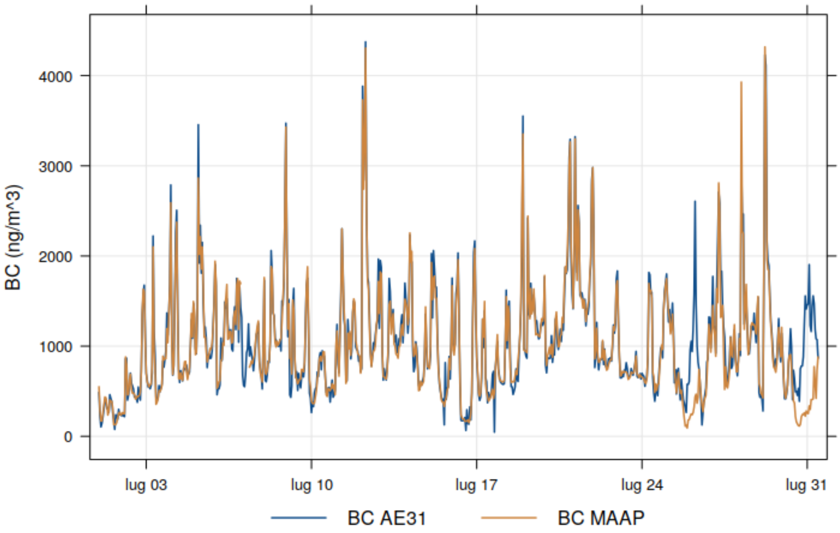

Figure 4.8: Time series (UTC+1) of BC mass concentration obtained by all instruments at BO.

4.3 Comparison between attenuation and absorption

In this section we compare the results of all the different measurement techniques used to derive absorption coefficients, in all the three sites. This was done through scatterplots of hourly averaged b_{abs} by MAAP and $b_{ATN}^{loading\ corrected}$ provided by Aethalometers (model AE31 and AE33) at the same wavelength of 637 nm.

Data obtained in the MC site are plotted in figure 4.9. Figure 4.9 a and 4.9 b compare the two models of Aethalometers with the MAAP, while 4.9 c compares Aethalometers among each other. The correlation is good in all cases, as testified by the correlation coefficient (R^2) ranging from 0.91 to 0.95, even if with some outliers and a tendency to disperse for growing values; the best instruments agreement is clearly the AE31 with MAAP.

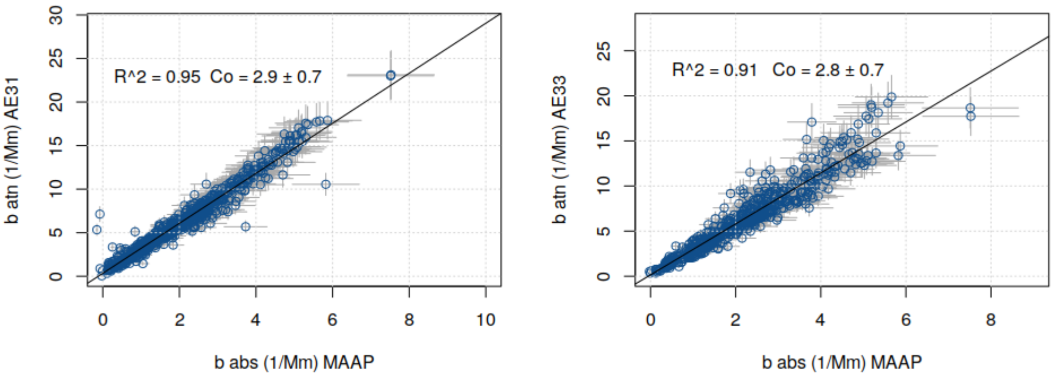

(a) *AE31 VS MAAP* (b) *AE33 VS MAAP*

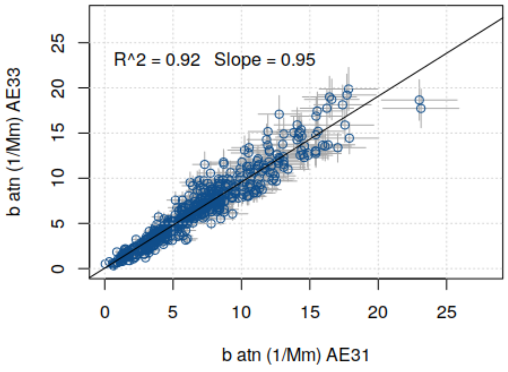

(c) *AE31 VS AE33*

Figure 4.9: Scatterplot and linear fit between all instruments used at MC.

The intercept was always negligible, while the slope was very close to unity only between the two Aethalometers, that measures the attenuation. Obviously the comparison between MAAP and each of the Aethalometers show large discrepancy from the unity in the slope, because the measured feature is different in the two kinds of instrument. The Aethalometer overestimation is in accordance with the multiple scattering effect described by Weingartner et al.; 2003, which is an apparent increase in absorption due to scattering by the filter fibres and/or non-absorbing particles here deposited, that increases the optical path of the beam. To correct this effect, a parameter C_0 was estimated as the ratio between the absorption values of the MAAP and the values of

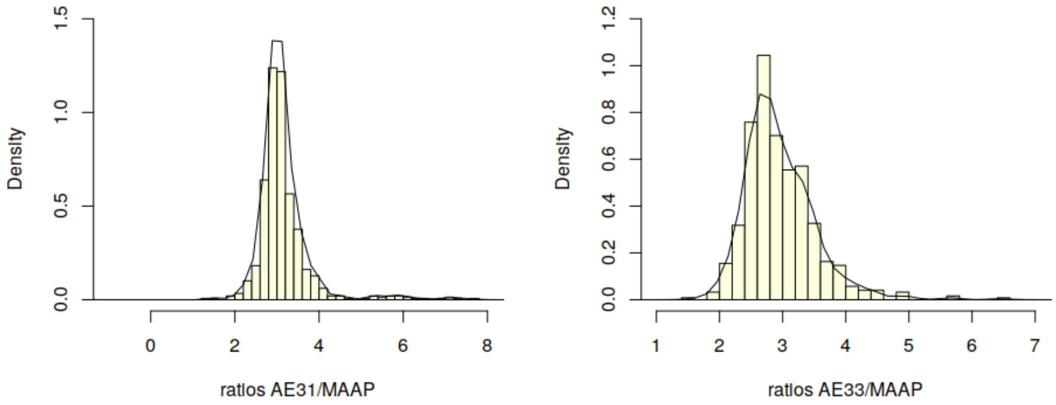

(a) *b(AE31) / b(MAAP)* (b) *b(AE33) / b(MAAP)*

Figure 4.10: Histograms and distribution of ratios between $b_{ATN}^{loading\ crrected}$ measured by AE31 (a), AE33 (b) and b_{abs} obtained by MAAP, at MC.

the Aethalometers already adjusted for the loading effect, as described in the previous chapter.

The distributions of ratios between hourly averaged values measured by Aethalometers and MAAP at MC are displayed in figure 4.10. That representing ratios between AE31 and MAAP's values is made up of a single main mode near 3, while that of AE33, MAAP ratios has a mode at about the same value that can be divided into two superimposed submodes, in accordance with their lower correlation. As the AE33 and AE31 are measuring the same aerosol population, the difference cannot be ascribed to different aerosol properties, but the interaction between aerosol and filter fibers scattering and the average among two different aerosol loads can possibly be the causes of the C_0 histogram distribution for AE33. The time series in figure 4.11, in which the few most evident outliers differing for more than 5 from the previous values were deleted, confirms that there are only a few moments in which the ratios significantly differ from the average, but that last for at most one hour.

The figure 4.12 shows then the same comparison between the instruments used at SPC. AE33 overestimates AE31 by a factor of 1.2 but with a good correlation (R^2=0.9). As expected, both Aethalometers attenuation values, overestimate the MAAP absorption values, but with a poorer correlation with them (R^2=0.62 and 0.7 for AE31 and AE33, respectively). The histograms in figure 4.13 confirm this trend by showing that the distribution of ratios between $b_{ATN}^{loading\ crrected}$ and b_{abs} has more than one mode of variability centered on significantly different values.

In SPC C_0 for AE33 is thus larger with respect to AE31 and both the distributions of ratios are less "clean" with respect to MC. In addiction it is possible to identify several populations of samples with higher factor. It remains difficult to put forward hypotheses on the causes of this behavior. One can be related to the non-ideal sampling line, which was not able to completely dry the aerosol population in the hot and humid summer in the low Po Valley. The discrepancy between the comparison of instruments in two different sites open questions that will be addressed in other frames.

Analyzing the time series of these ratios (figure 4.14), it can be observed that most of the particularly high ones, are concentrated in a few days along the campaign and the increases are simultaneous for Aethalometers AE31 and AE33. There is also one period at 12:00 UTC+1 on 16 July were they show a lower value. But this is also a period of very low values of b_{ATN} that probably falls below the detection limit, and

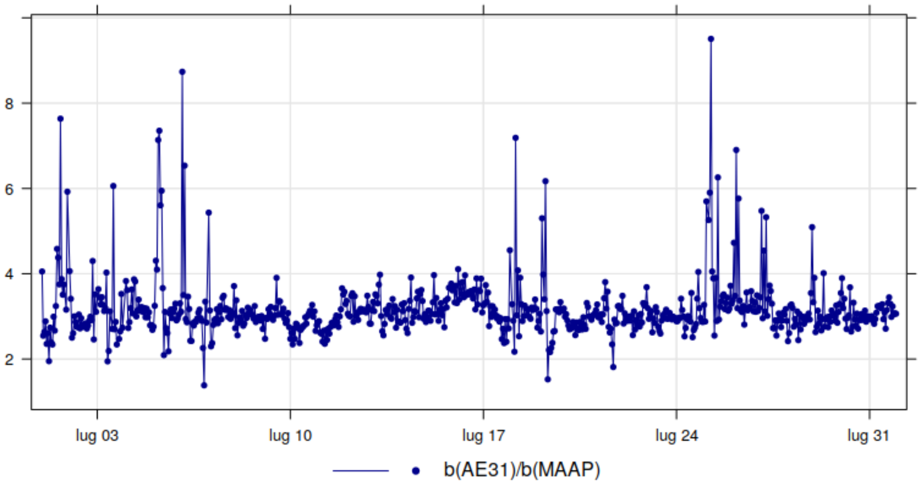

(a) *b(AE31) / b(MAAP)*

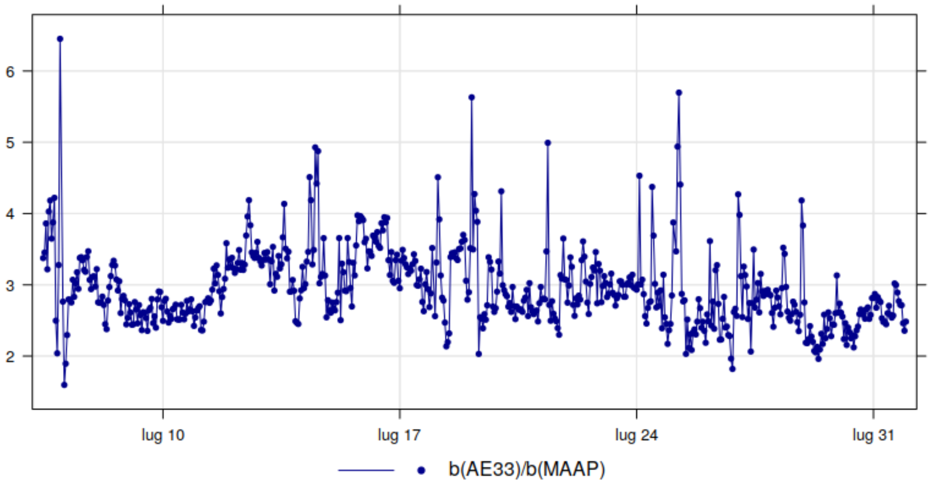

(b) *b(AE33) / b(MAAP)*

Figure 4.11: Time series of ratios between hourly averaged $b_{ATN}^{loading\ crrected}$ measured by AE31 (a), AE33 (b) and b_{abs} obtained by MAAP at MC.

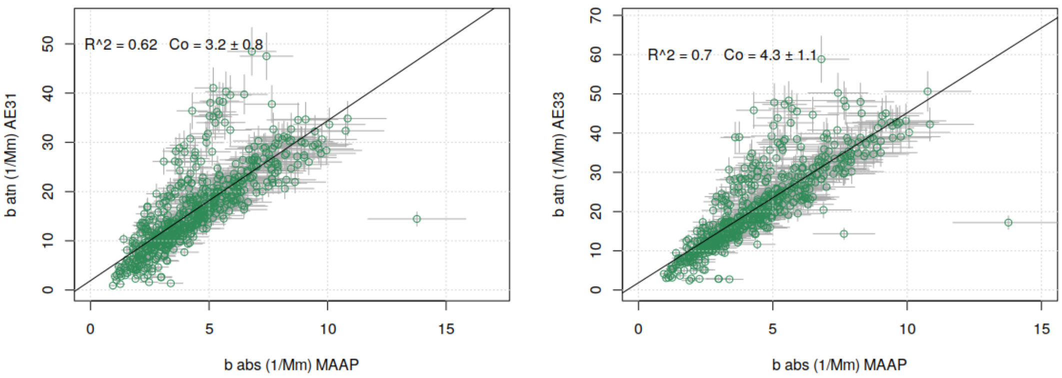

(a) *AE31 VS MAAP* (b) *AE33 VS MAAP*

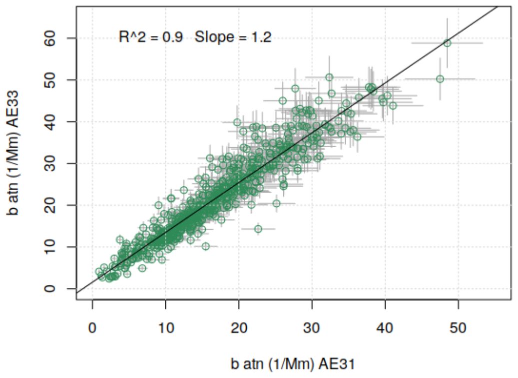

(c) *AE31 VS AE33*

Figure 4.12: Scatterplot and linear fit between all instruments used at SPC.

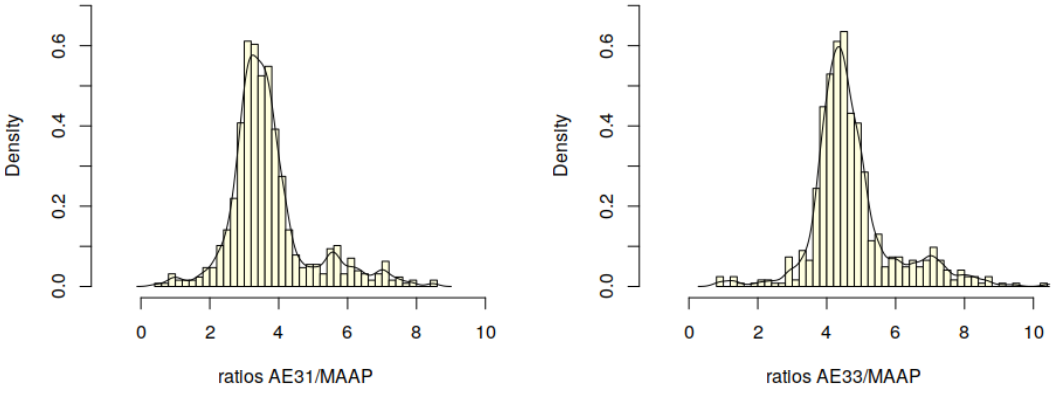

(a) *b(AE31) / b(MAAP)* (b) *b(AE33) / b(MAAP)*

Figure 4.13: Histograms illustrating the distributions of ratios between b$_{ATN}^{loading\ crrected}$ by AE31 (a), AE33 (b) and b$_{abs}$ by MAAP at SPC.

thus not attributable to a change in the aerosol population.

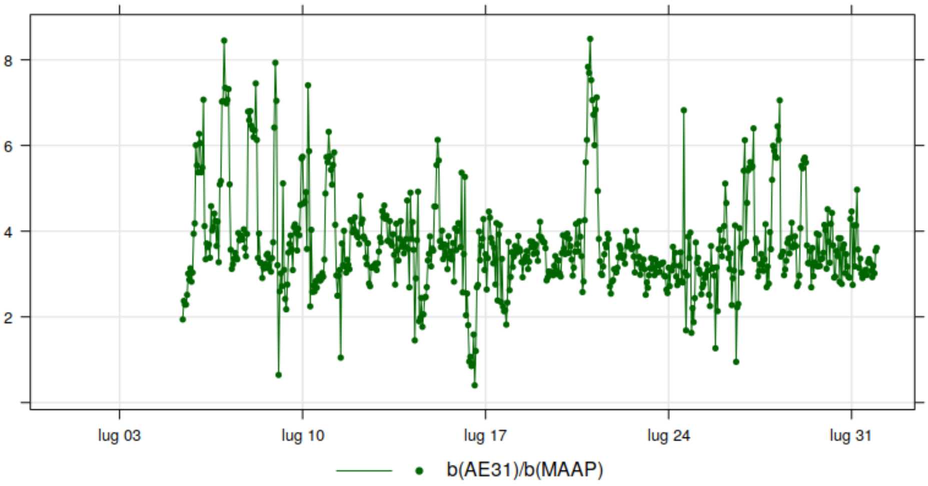

(a) *b(AE31) / b(MAAP)*

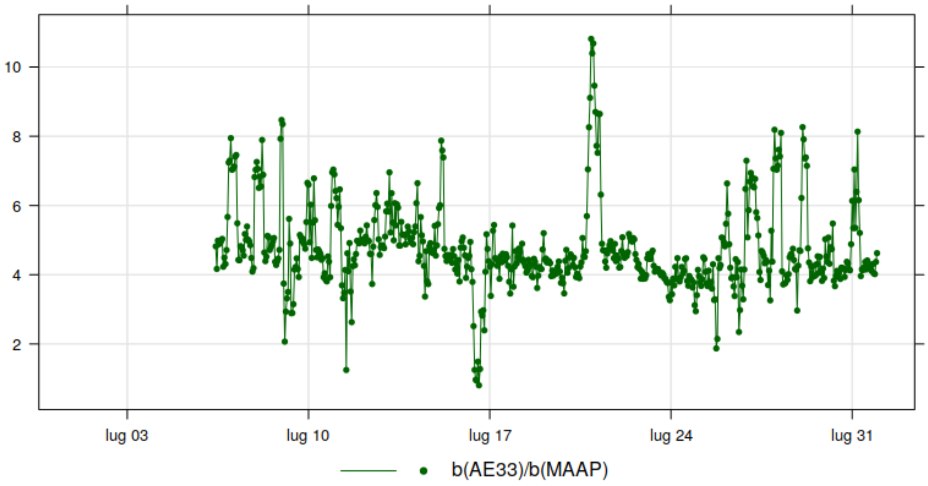

(b) *b(AE33) / b(MAAP)*

Figure 4.14: Time series of the ratios between $b_{ATN}^{loading\ crrected}$ by AE31 (a), AE33 (b) and b_{abs} by MAAP at SPC.

We analyzed in details the relationship with meteorological parameters for a couple of positive events, reported in figure 4.15. It is possible to notice that the C_0 increases are often associated with a temperature drop in a high humidity environment (possible saturation and droplets activation). A possible explanation for this higher overestimation in some periods of the month could be the condensation of vapours on the filter when temperature is enough low and the environment is rich in condensable species. The additional scattering material thus embedded in the filter leads to a significant increase of the optical path of the light beam, which explains the observed enhancement in b_{ATN}.

Scatterplots comparing AE31 and MAAP's values at BO are finally depicted in figure 4.16, and show a good correlation ($R^2 = 0.86$) and the typical overestimation attenuation on MAAP absorption coefficient. The typical C_0 factor, derived from Bologna data is 3.3, in agreement with other literature values for an urban site. Also in this case there are some points in which this overestimation becomes higher, concentrated in two short periods in the last part of the month on 26 and 31 July. Figure 4.17 illustrates that in

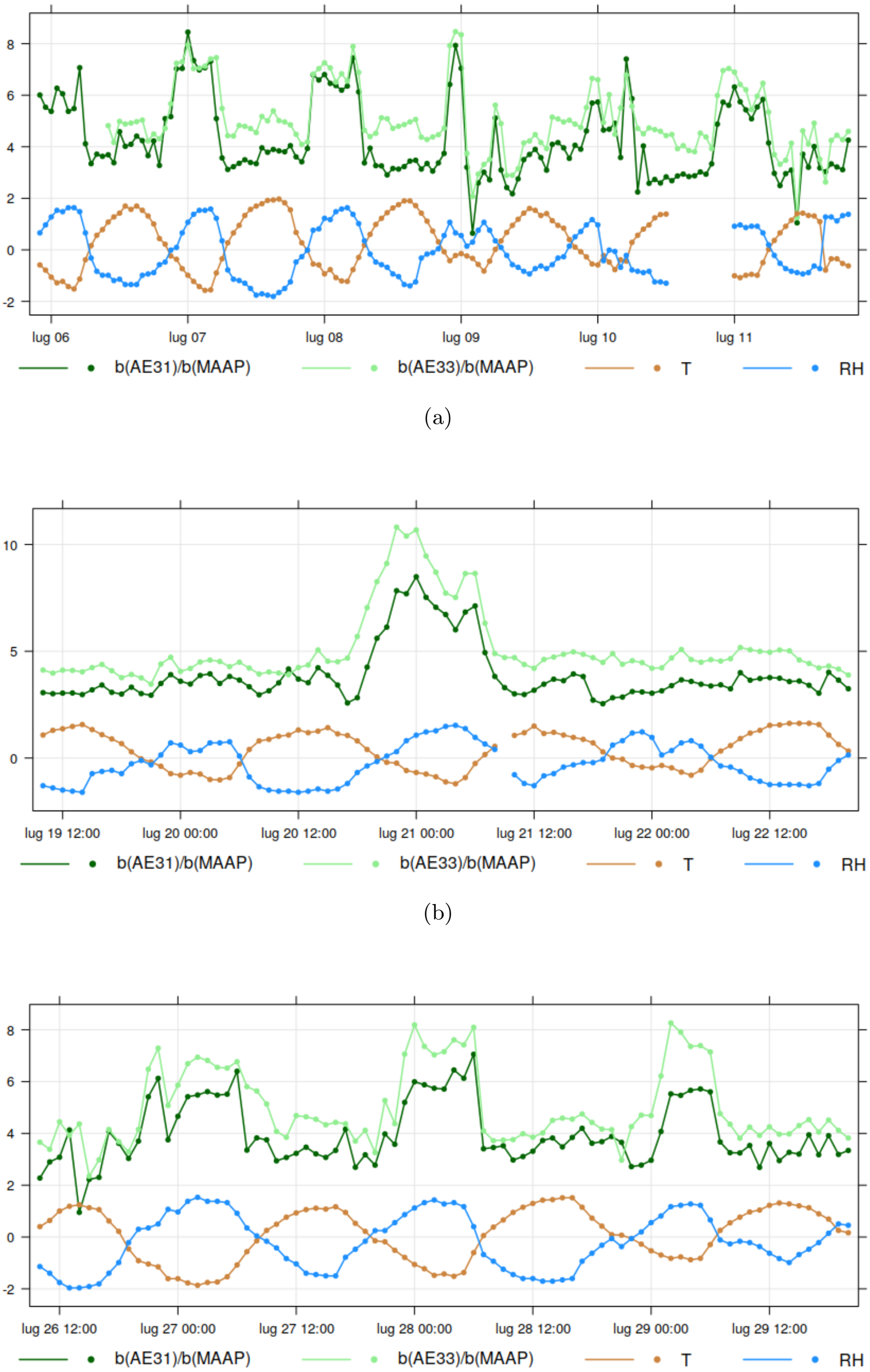

(a)

(b)

(c)

Figure 4.15: Comparison between and normalized values of temperature and humidity, obtained by subtracting the mean and dividing for their standard deviation and $b_{ATN}^{loading\ crrected}$ / b_{abs} ratios, in three different periods at SPC: a) from 6 to 12 July; b) from 19 July at 12:00 to 22 at 16:00; c) from 26 at 12:00 to 29 at 16:00.

those days there were very low values of absorption very close to the detection limit of the instruments, combined with similar conditions as in SPC.

The enhancement in C_0 values due to condensation on the filter is also described in Weingartner et al. (2003) and is observed in particular in the two sites of the plain, while it is less effective in the mountain site, where the atmosphere does not have the same high concentrations of condensable species as in BO and SPC.

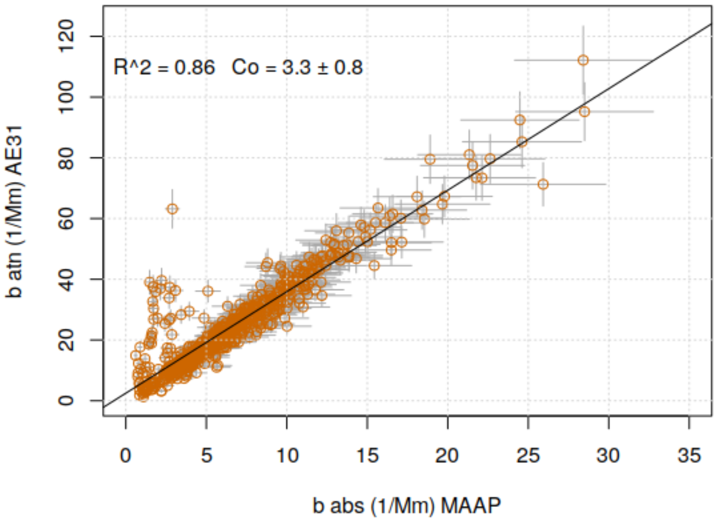

Figure 4.16: Scatterplot and linear fit of $b_{ATN}^{loading\ crrected}$ measured by AE31 and b_{abs} by MAAP at BO.

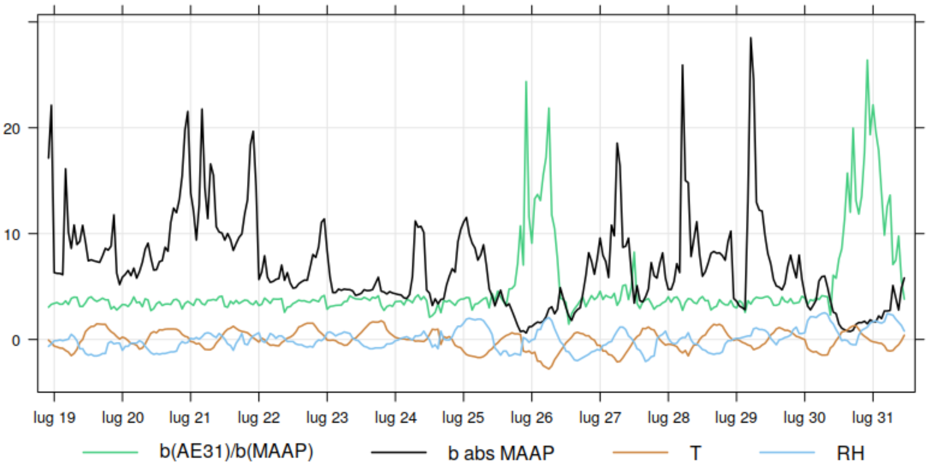

Figure 4.17: Comparison between $b_{ATN}^{loading\ crrected}$ / b_{abs} ratios, b_{abs} by MAAP and normalized temperature and pressure at BO between 19 and 31 July.

A summary of all C_0 parameters for correcting the Aethalometer data for the multiple scattering effect is provided in figures 4.9, 4.12, 4.16 and table 4.2, which also shows the values of R^2 indicating the correlation between the instruments.

The mountain site shows in general lower values of C_0 than the other two. This is in accordance with the observed decrease in C_0 with the aerosol aging time, discussed in Weingartner et al. (2003).

Comparing them with those determined in other ACTRIS measurement campaigns, throughout Europe, depicted in figures 4.18, it can be seen that they are in good agreement with them and that within the measurement uncertainties, they are close to the value of 3.5 suggested by the WMO when only Aethalometer measure are available, indicated in the graph with a straight line.

	Cimone		St. Pietro Capofiume		Bologna
	AE31	AE33	AE31	AE33	AE31
C_0	2.9 ± 0.7	2.8 ± 0.7	3.2 ± 0.8	4.3 ± 1.1	3.3 ± 0.8
R^2	0.95	0.91	0.62	0.7	0.86

Table 4.2: C_0 values for correcting AE31 and AE33's data for multiple scattering for all the instruments in all sites.

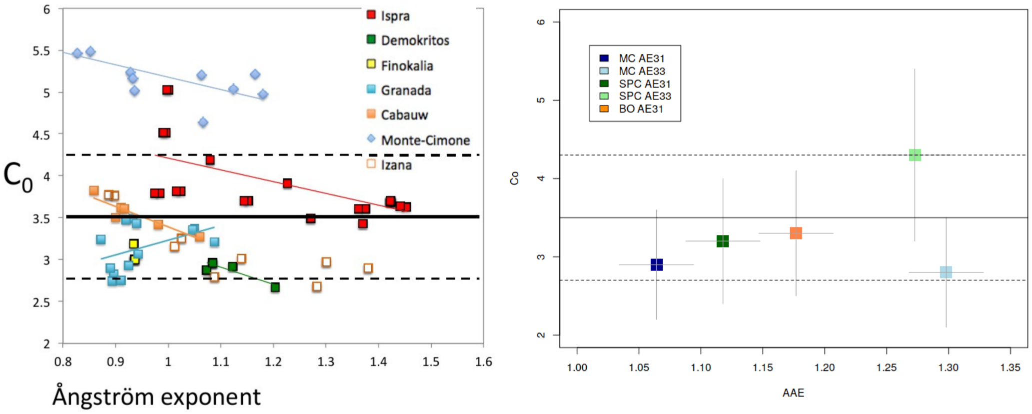

(a) (b)

Figure 4.18: C_0 calibration coefficient obtained a) within ACTRIS network, b) from data analyzed in this thesis.

Once all the necessary corrections had been applied, the measurements made by the two models of Aethalometers were further compared with those of the MAAP for the 637 nm wavelength and with each other over the entire measured spectrum, to assess their comparability.

In table 4.3, monthly averaged values of absorption coefficients derived by all available instruments after the application of corrective parameters are listed. Table 4.4 also shows the same mean but filtering the data set by avoiding points in which the ratio falls in the tails of its distribution. It is possible to notice that, at BO and MC all average values increase suggesting that the main reason for different ratios is the influence of uncertainty on C_0 factor derived from very low values of absorption that falls below the detection limit of the instrument, while at SPC there were both influence of very low (high uncertainty) absorption values, as well as interference from moisture that increase the attenuation values but not the absorption measured by MAAP. .

In the plots of figure 4.19 it is possible to observe the time series of daily averages of the values of each instrument, in each measurement site. The time series of MC daily means have similar trends with few periods of non matching values where the differences are, however, falling in the range of error bars. The AE31 follows the MAAP trend well and measures larger values only in a few days. The AE33, on the other hand, deviates more overestimating on several days, such as the July, 6th. In SPC the agreement is less strict: both models of Aethalometers overestimates the MAAP absorption, especially on those days where locally the C_0 values were much higher, due to non ideal sampling in humid environment. The same behavior can be observed on the BO site, with the

	Cimone			St. Pietro Capofiume			Bologna	
	MAAP	AE31	AE33	MAAP	AE31	AE33	MAAP	AE31
mean (1/Mm)	2.0 ± 0.3	2.1 ± 0.7	2.2 ± 0.8	4.1 ± 0.6	5.1 ± 1.8	5.0 ± 1.7	6.6 ± 0.9	7 ± 2
sd (1/Mm)	1.3	1.3	1.4	2.0	2.5	2.4	4.1	4

Table 4.3: Mean and standard deviation of b_{abs} (1/Mm) for all instruments in their whole period of measure (July 2017).

	Cimone			St. Pietro Capofiume			Bologna	
	MAAP	AE31	AE33	MAAP	AE31	AE33	MAAP	AE31
mean (1/Mm)	2.1 ± 0.3	2.2 ± 0.7	2.3 ± 0.8	4.5 ± 0.6	4.8 ± 1.8	4.7 ± 1.7	6.9 ± 0.9	7.5 ± 1.9
sd (1/Mm)	1.3	1.3	1.4	2.0	2.2	2.2	4.0	4.5

Table 4.4: Mean and standard deviation of b_{abs} (1/Mm) for all instruments in their whole period of measure after filtering data deleting the tails of $b_{ATN}^{loading\ corrected}$ / b_{abs} ratios distributions (July 2017).

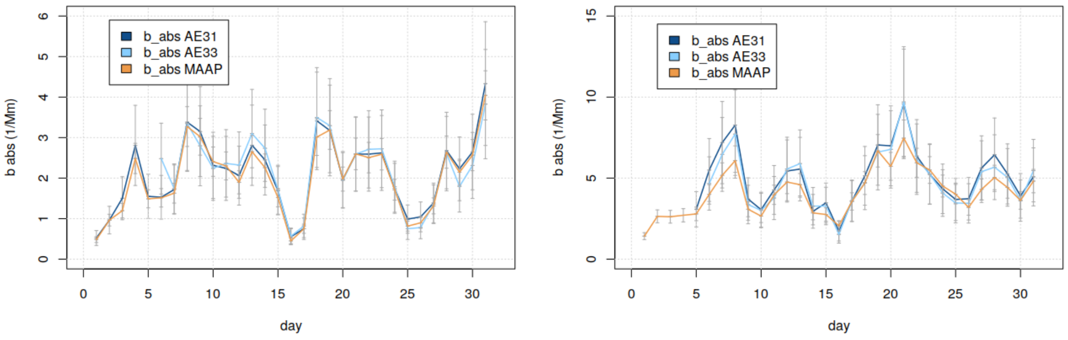

(a) *MC* (b) *SPC*

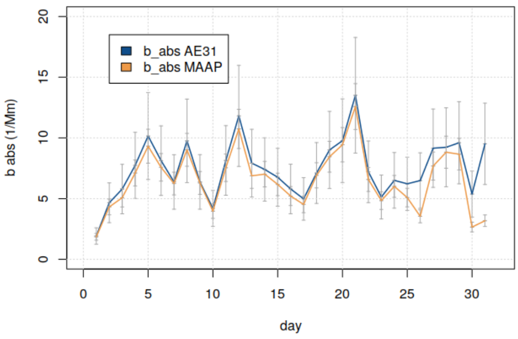

(c) *BO*

Figure 4.19: Comparison between daily averages of absorption coefficients measured by all instruments in the three sites. All values are reported at 637 nm through the AAE.

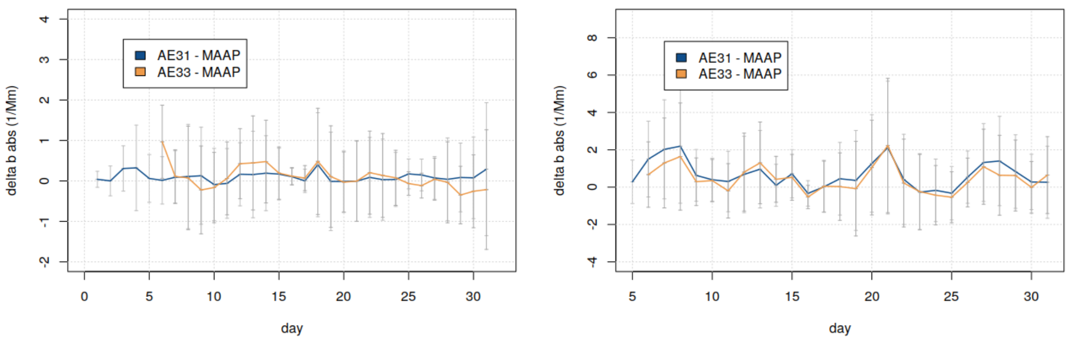

(a) *MC* (b) *SPC*

Figure 4.20: Comparison of daily averages of differences between the two models of Aethalometers, at SPC and MC

periods of overestimation discussed above making the MAAP and AE31 measures not comparable and a good agreement in the rest of the month.

From table 4.3 it can be observed that in the case of the MC site, the absorption values calculated from Aethalometer attenuation are very close to the MAAP measurements, while in the case of SPC and BO, where there are limitations due to possible condensation of water vapour and possible other substances, the discrepancies are higher. Especially AE31 in Monte Cimone shows the best performances, while in San Pietro AE33 seems to be in better agreement.

Site				b_{abs} AE31 VS b_{abs} AE33 at:				
		370 nm	470 nm	520 nm	590 nm	660 nm	880 nm	950 nm
MC	R^2	0.93	0.93	0.93	0.92	0.91	0.89	0.88
	Slope	0.89	0.87	0.89	0.91	0.94	0.92	0.87
SPC	R^2	0.92	0.92	0.92	0.91	0.90	0.89	0.89
	Slope	0.86	0.93	0.95	0.99	1.0	1.1	1.0

Table 4.5: Parameter of the linear fit between AE31 and AE33 at all wavelength at MC and SPC.

The figure 4.20 then shows how the difference between absorption values of the two models of Aethalometers and those from the MAAP along the month, to compare them and assess whether one of them shows a better agreement with the MAAP. At MC the AE31 is the one that matches best with smaller differences, on average 7 % and with a maximum of 26 %, less variable during the month. While the AE33 has an average difference of 11 % with a much higher maximum that reaches 64 %. In the case of SPCs both are larger and more variable but also in greater agreement between them. The average and maximum values for AE31 and AE33 are 17% and 14% respectively and 39% and 30% respectively. However, the corrected Aethalometers values show large uncertainties.

Figure 4.22, 4.23 compare b_{abs} measured by the two Aethalometers at each wavelength. The linear fits show values of R^2 around 0.9 for every wavelength. The slopes vary between 0.87 and 0.92 showing small overestimates of the AE33 on the AE31 used at the MC site, larger for the wavelengths: 370 nm, 470 nm and 950 nm. At SPC instead show slopes much closer to one in all cases with the larger exception for 370 nm.

In figure 4.21, the time series of the instruments differences for all wavelengths, together with the b_{abs} at 637 nm, are shown. The 370 nm wavelength shows the larger difference among the two instruments. In addition, these differences are not constant along the campaign, but become particularly pronounced where the BC concentration are larger.

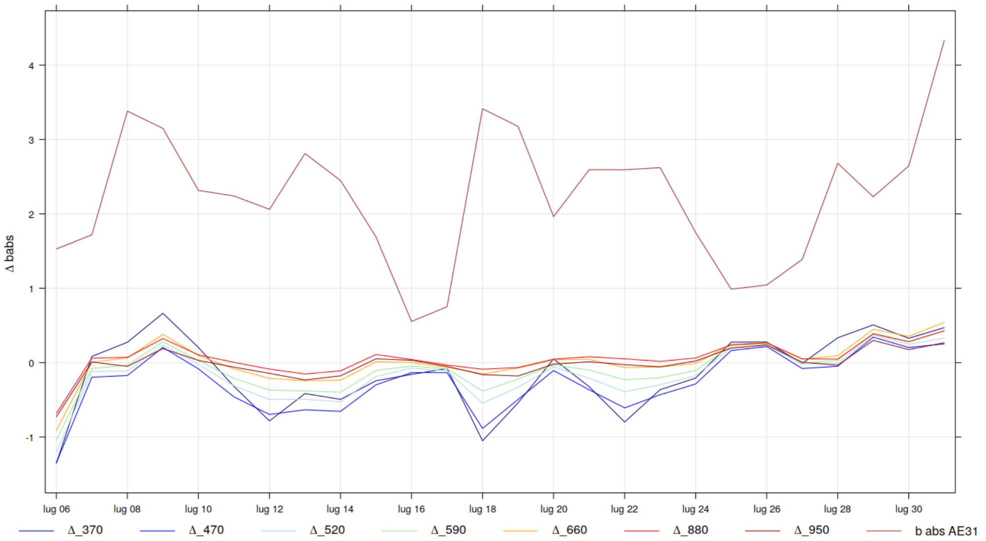

(a) *MC*

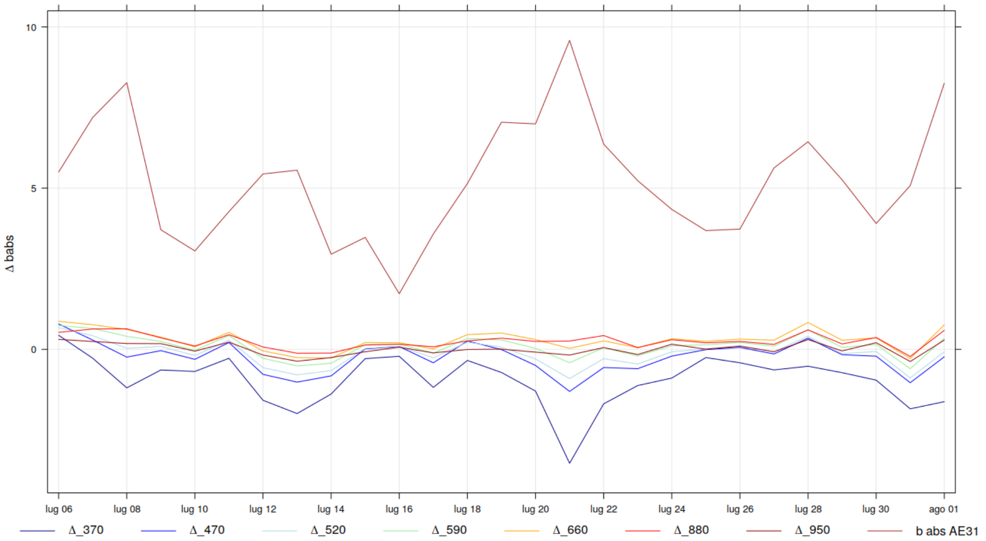

(b) *SPC*

Figure 4.21: Time series (UTC+1) of differences between daily averaged $b_{abs}(\lambda)$ measured by AE31 and those measured by AE33, compared to the daily averages of $b_{abs}(637nm)$ derived from AE31.

It could be that, especially at high concentrations, the effects of loading and multiple scattering, as well as the possible bias in the value of the absorption coefficient to be associated with BC for the presence of other absorbing compounds or for the internal and external mixing of BC with other substances, become important causing substantial differences with the MAAP but also between different Aethalometers, that use different correction scheme, impacting preferentially the lower wavelengths. Details of this variability should be further investigated also considering measure under controlled environmental conditions in order to improve the identification of factors affecting the instrument uncertainties. The calculation of the absorption angstrom exponent (AAE), related to the BC source identification is then affected by a large uncertainty.

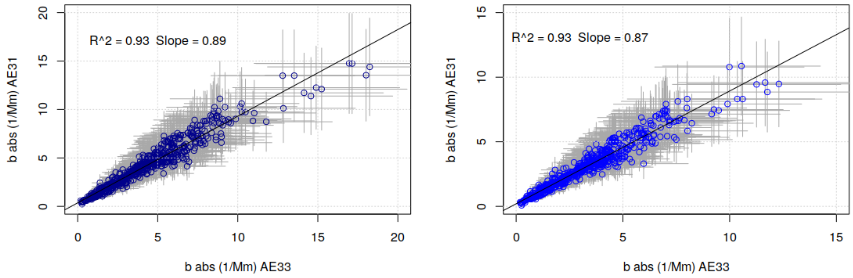

(a) *370 nm* (b) *470 nm*

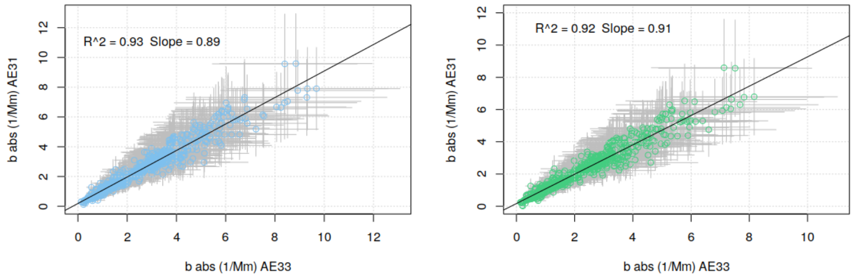

(c) *520 nm* (d) *590 nm*

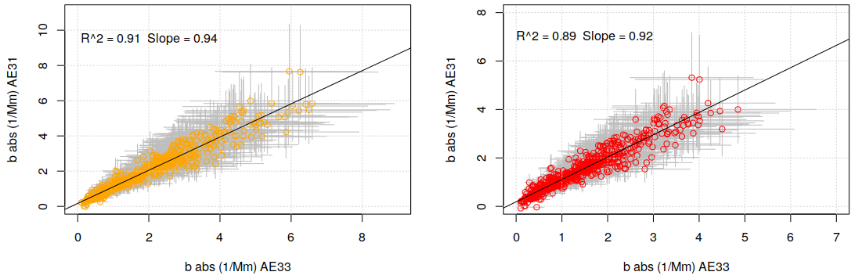

(e) *660 nm* (f) *880 nm*

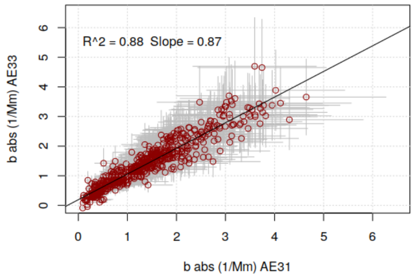

(g) *950 nm*

Figure 4.22: Comparison of the measured absorption values of both Aethalometers at all wavelengths at MC.

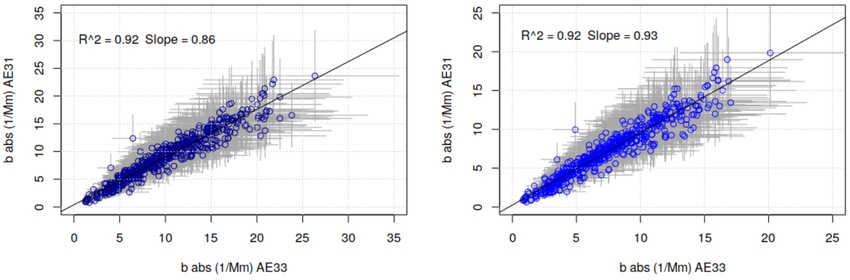

(a) *370 nm* (b) *470 nm*

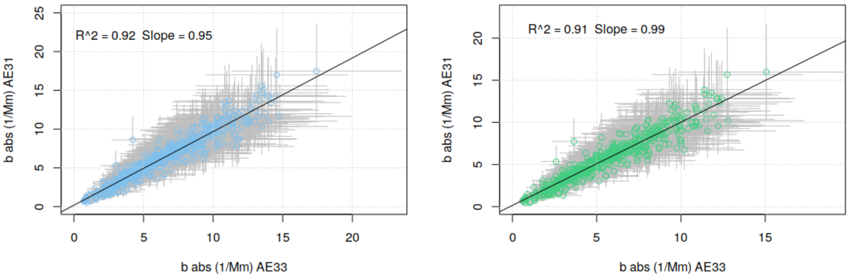

(c) *520 nm* (d) *590 nm*

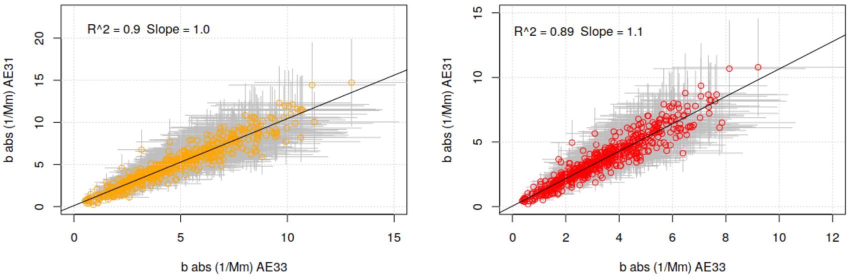

(e) *660 nm* (f) *880 nm*

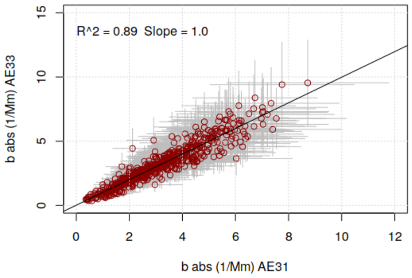

(g) *950 nm*

Figure 4.23: Comparison of the measured absorption values of both Aethalometers at all wavelengths at SPC.

4.4 Aerosol optical properties

4.4.1 Absorption and scattering coefficients in July 2017

A general analysis of the monthly variability of the optical properties was carried out studying the overall behavior of the absorption, scattering coefficients and derived parameters, like single scattering albedo and aerosol absorption and scattering Angstrom exponents. The overall behavior over the month is summarized by the box and whiskers plots in figure 4.24.

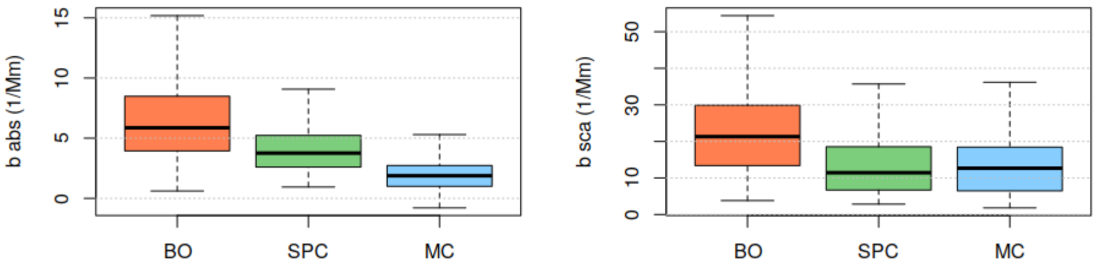

(a) *Absorption coefficient (1/Mm)* (b) *Scattering coefficient (1/Mm)*

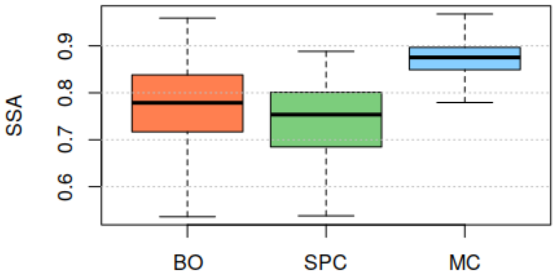

(c) *Single Scattering Albedo (SSA)*

Figure 4.24: Box and whiskers plots showing the median of the values, the 25th and 75th percentile and maximum and minimum values of: a) absorption coefficients measured by MAAP; b) scattering coefficients measured by Nephelometer; c) SSA derived from them, for all the three sites.

The highest values of both absorption and scattering coefficients are those measured in the urban site of BO, with a mean of 6.6 ± 0.9 Mm^{-1} and 23 ± 3 Mm^{-1} respectively. This site has also the largest variability in both coefficients with standard deviation of 4.4 and 12 Mm^{-1}. These values agree with what is expected for an urban site with strong influence of many different anthropogenic local sources, first of all the vehicular traffic. SPC shows a mean b_{abs} of 4.1 ± 0.6 Mm^{-1} with standard deviation of 2.0 Mm^{-1} and b_{sca} which mean value and standard deviation are 13.4 ± 1.6 and 8.8 Mm^{-1} respectively. It has thus slightly lower values of b_{abs} with respect to BO but not negligible amount of scattering particles, in accordance with what we could expect from a rural site in the Po basin, that often shows homogeneous pollution degree among urban and extra-urban areas.

Site	Parameter	Mean	St. Dev.	Median	Percentiles 5th	 95th
	b abs (1/Mm)	2.0	1.3	1.9	0.3	4.5
MC	b sca (1/Mm)	13.5	7.9	12.7	3.5	27.2
	SSA	0.87	0.04	0.88	0.81	0.93
	b abs (1/Mm)	4.1	2.0	3.8	1.5	7.9
SPC	b sca (1/Mm)	13.6	8.7	11.4	3.9	28.9
	SSA	0.74	0.08	0.75	0.59	0.85
	b abs (1/Mm)	6.6	4	5.9	1.6	13.7
BO	b sca (1/Mm)	22.8	12.2	21.3	8.0	42.9
	SSA	0.77	0.09	0.78	0.61	0.89

Table 4.6: Statistical analysis of b_{abs}, b_{sca} and SSA on the whole month of measure at the three measurement sites.

In rural sites we expect lower traffic sources than the urban one, but agricultural, industrial, energy related activities and possible transport from more polluted regions. The site of MC shows the lowest values of absorption (2.0 ± 0.3 Mm^{-1} on average, with standard deviation of 1.5 Mm^{-1}) and values of scattering coefficient with a mean of 13.4 ± 1.6 Mm^{-1}, and standard deviation of 7.9 Mm^{-1}. The mountain environment is thus characterized by a cleaner air than the plain, but can be subject to transport of pollutants in particular in the summer season. The mean values reported here are in accordance with those determined in other campaigns in the framework of ACTRIS for European urban, rural and mountain sites (Pandolfi et al., 2018; Zanatta et al. 2016).

Mean values of SSA for BO, SPC e MC are respectively 0.77 ± 0.03, 0.74 ± 0.04 and 0.87 ± 0.03. Such low values of single scattering albedo in the sites of BO and SPC reflect the influence of combustion sources in emission of aerosol population in Po Valley, while the higher values at MC indicate that aerosol reaching the mountain site are in general more mixed with non absorbing fraction and secondary aerosols. Concerning SPC, although it is a rural site and suffers less from sources such as traffic or household activities, it is still immersed in the Po Valley and exposed to transport from nearby, highly polluted areas. The values of the scattering coefficient should certainly be higher than those of the MC and more similar to those of BO, as is the case for absorption. A probable explanation for this discrepancy is the elimination of periods with high humidity, which are very frequent in this site. The days eliminated between 12 and 14 and the days of 8 and 31 were in fact characterized by very high values and including them would significantly raise the average value.

The behavior of scattering and absorption coefficient, as well as the derived parameters, along the month are now discussed, also in comparison with the origin of air masses. The backtrajectories of air masses reaching the three sites, derived through simulations performed each 6 hours from the middle of June until the end of August, using the Lagrangian transport model FLEXPART, were used and also PM_{10} mass concentration at Bologna and the identification of dust events derived in a previous study in which FLEXPART simulations were coupled to AEROCOM database for all the three sites.

Looking at the time series of both coefficients at all three sites, we can identify three periods of low concentrations of both absorbing and scattering particles, common to all the sites and thus probably related to regional circulation and/or common removal processes. The first period was at the beginning of the month, the second one around the 16th and the last around the 26th of July. These periods are also associated with a decrease in temperatures throughout the region and therefore probably due to larger-scale weather phenomena that have affected meteorology and concentrations throughout

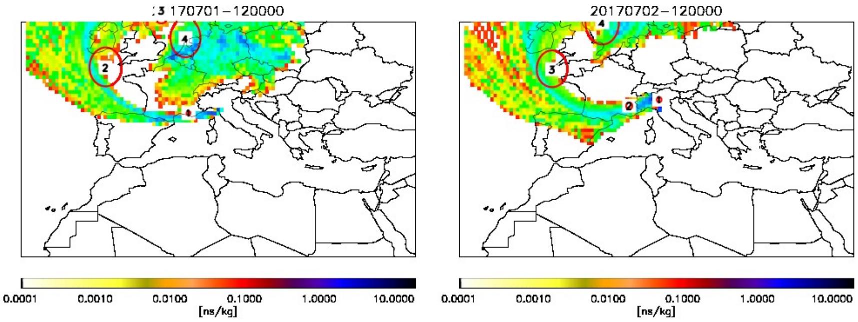

(a) 1 july MC (b) 2 july MC

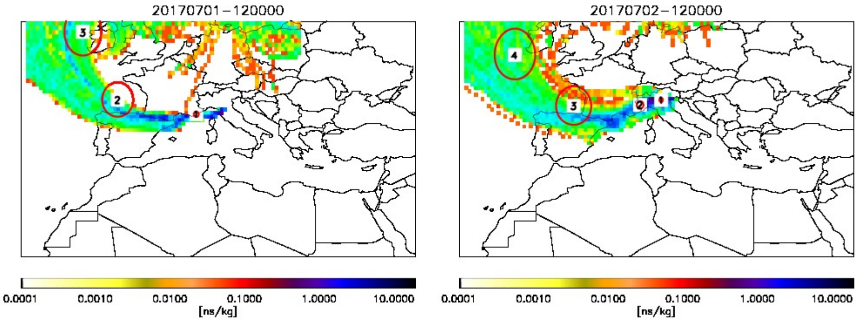

(c) 1 july SPC (d) 2 july SPC

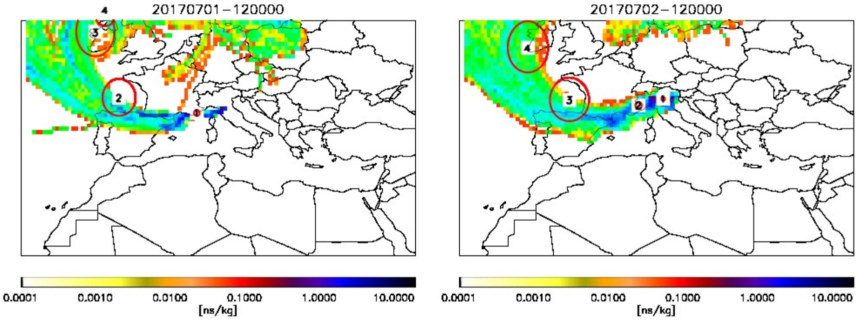

(e) 1 july BO (f) 2 july BO

Figure 4.25: Backtrajectories of air masses reaching: MC site on a) 1 and b) 2 July; SPC site on c) 1 and d) 2 July; BO site on e) 1 and f) 2 July, by FLEXPART's simulations.

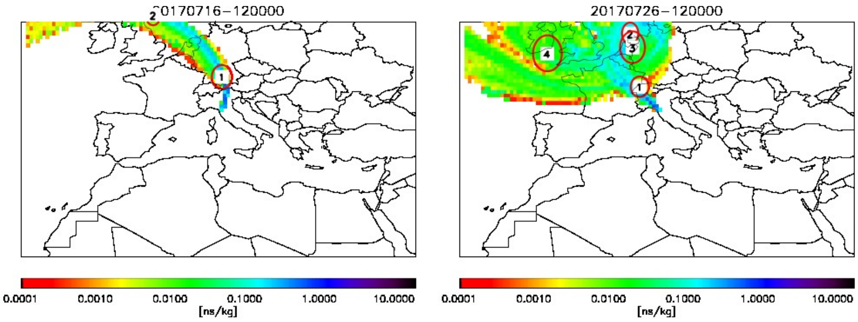

(a) 16 july MC

(b) 26 july MC

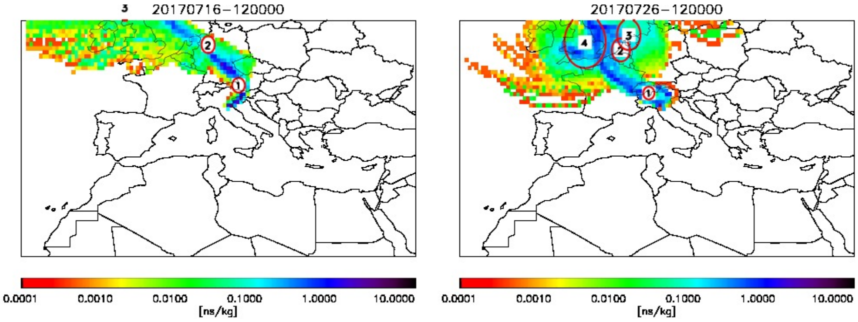

(c) 16 july SPC

(d) 26 july SPC

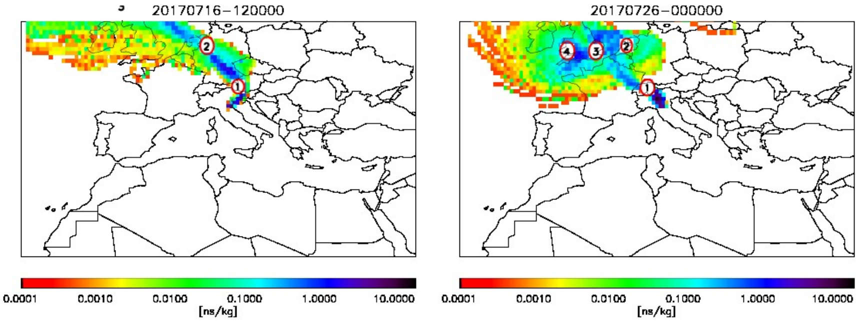

(e) 16 july BO

(f) 26 july BO

Figure 4.26: Backtrajectories of air masses reaching: MC site on a) 16 and b) 26 July; SPC site on c) 16 and d) 26 July; BO site on e) 16 and f) 26 July, by FLEXPART's simulations.

the region. The trajectories obtained by the model for these days in the various sites are shown in the figures 4.25, 4.26 and show that air masses, in these days with low values of aerosol concentrations, came mainly from the North of Europe passing through the Atlantic Ocean or from Germany.

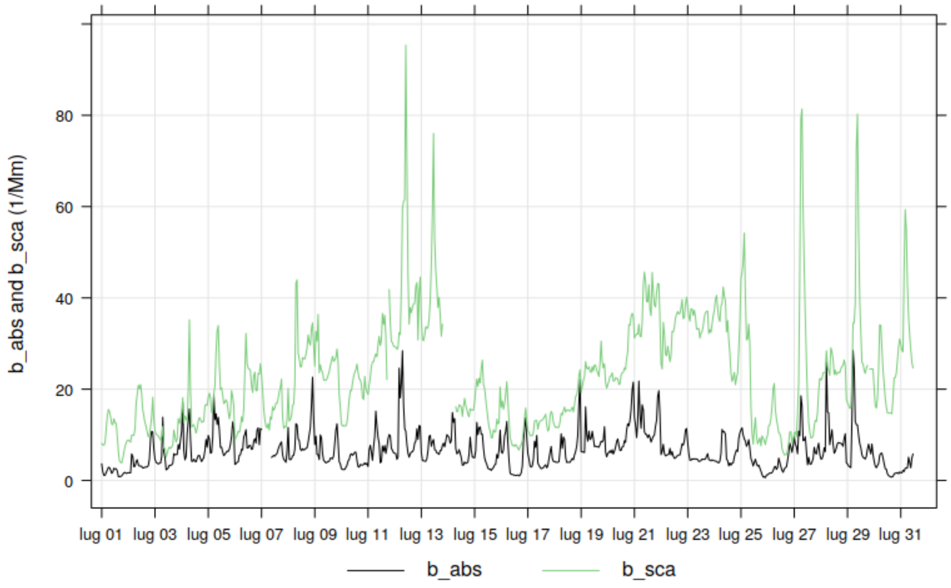

(a) b_{abs} and b_{sca}

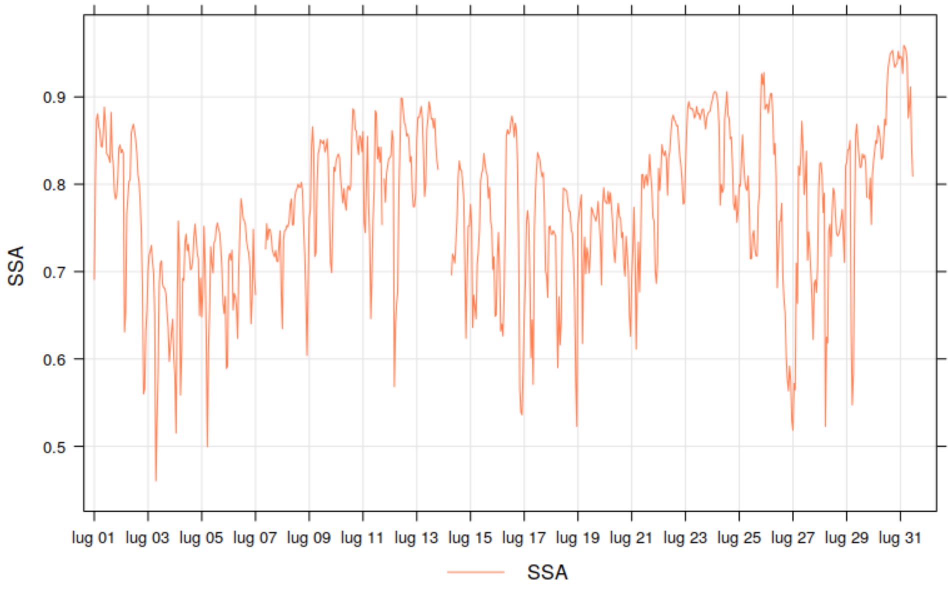

(b) *Single Scattering Albedo (SSA)*

Figure 4.27: Time series (time zone UTC+1) of hourly averaged values of: a) absorption and scattering coefficients; b) single scattering albedo. Measured or determined from values acquired by MAAP and Nephelometer at BO site.

The time series of hourly averaged values measured at BO is depicted in figure 4.27, were we can see that scattering and absorption show a variability not always well correlated with some different maximums and minimums, reflecting a change in the aerosol composition and properties. This is evident in SSA values which strongly varies during the month, spanning a range between less than 0.6 and more than 0.9.

The reason for this is that, even if the main sources of urban pollution are freshly

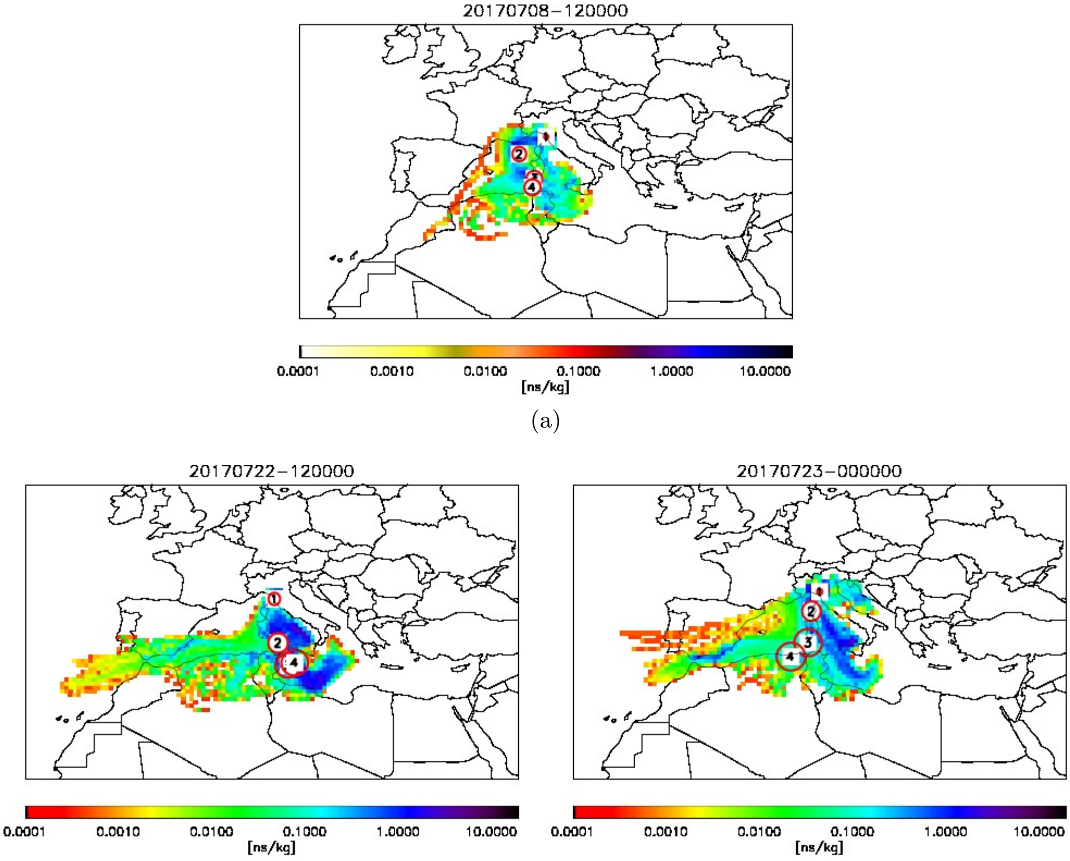

(a)

(b)

(c)

Figure 4.28: Backtrajectories by FLEXPART's simulations on a) 8; b) 22 and c) 23 July.

emitted particles from traffic related sources, there are also some periods in which it is affected by less absorbing particles from different sources, such as factories or long range transport of dust (or re-suspended from the soil), see spray and more aged particles.

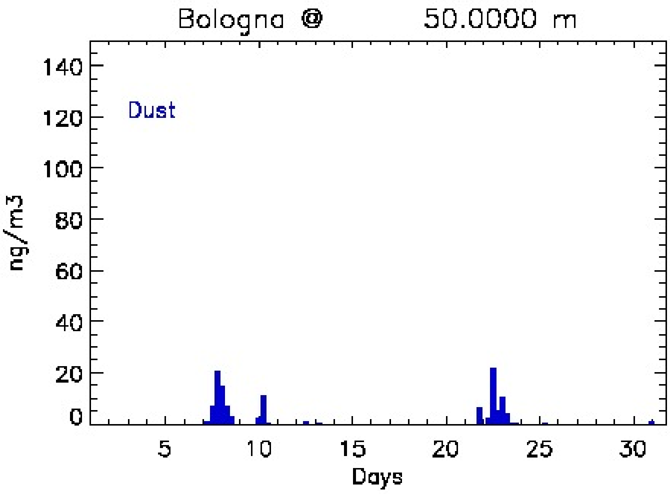

Figure 4.29: Identification of dust events at BO.

It also shows that two other periods can be observed with very low absorption coefficients on 10 and 30 and 31, but accompanied by higher values of scattering coefficient and single scattering albedo. On 10 and 31 July, the figure 4.29 assumes two episodes of dust, although not particularly strong. These are not well visible in the absorption values for which one would expect an increase in line with the fact that the dust absorbs the radiation even if especially at wavelengths smaller than 637 nm.

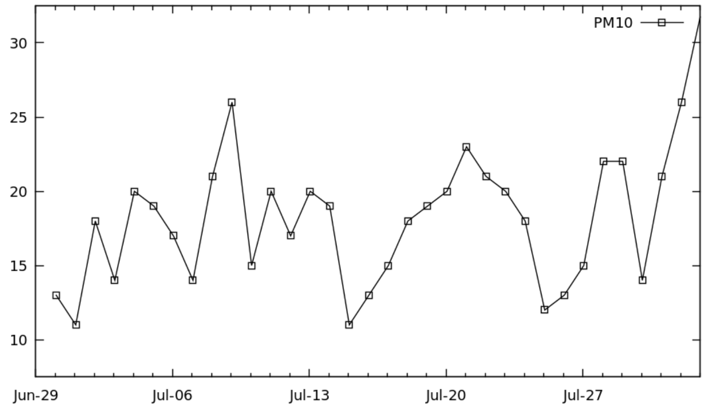

Figure 4.30: Time series of daily averaged values of PM_{10} at BO.

Two more dust episodes occurred in BO on 8 and 22 and 23 July, as can be seen from the backtrajectories in the figure 4.28 and 4.29, where air masses came mainly from the Mediterranean sea and north Africa. On the 8th there are peaks in the morning and in the evening both in absorption and in scattering, with lower SSA values in the morning and increasing towards evening. While on 22 and 23, absorption remains rather low with only one peak on 22 evening and scattering has instead high and constant values on both days with little variation during the day. In general, these BO dust events seem to be associated with higher and more constant values in the scattering coefficient, without strong influences on the absorption coefficient and generally with higher SSAs.

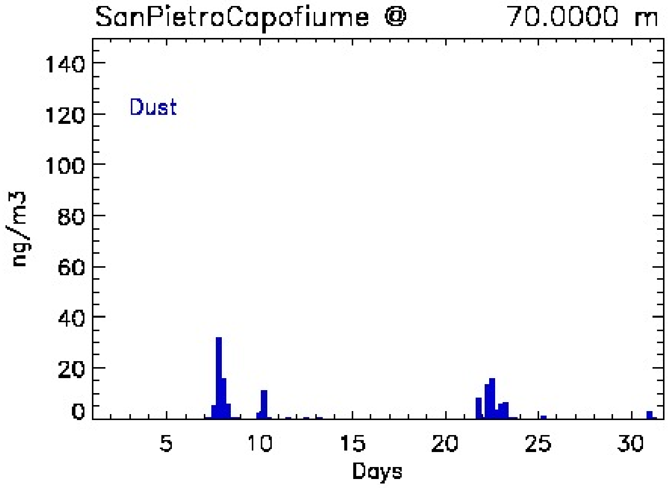

Figure 4.31: Identification of dust events at SPC.

The concentration measured between 19 and 21, were then high for both coefficients and also for PM_{10} concentration in figure 4.30, this, in association with low values of SSA, suggest anthropogenic sources of pollution or biomass burning as the main causes.

Figure 4.32 shows the time series of b_{abs}, b_{sca} and SSA measured at SPC. As already mentioned above, they have the same low concentration periods on the first days of the month, on the 16th and 26th of the other two sites, with air masses coming from higher altitudes and less polluted areas.

High values of absorption and scattering with high variability in the SSA were measured on 6, 7. The 8 was characterized by dust transport(figure 4.31), it shows high

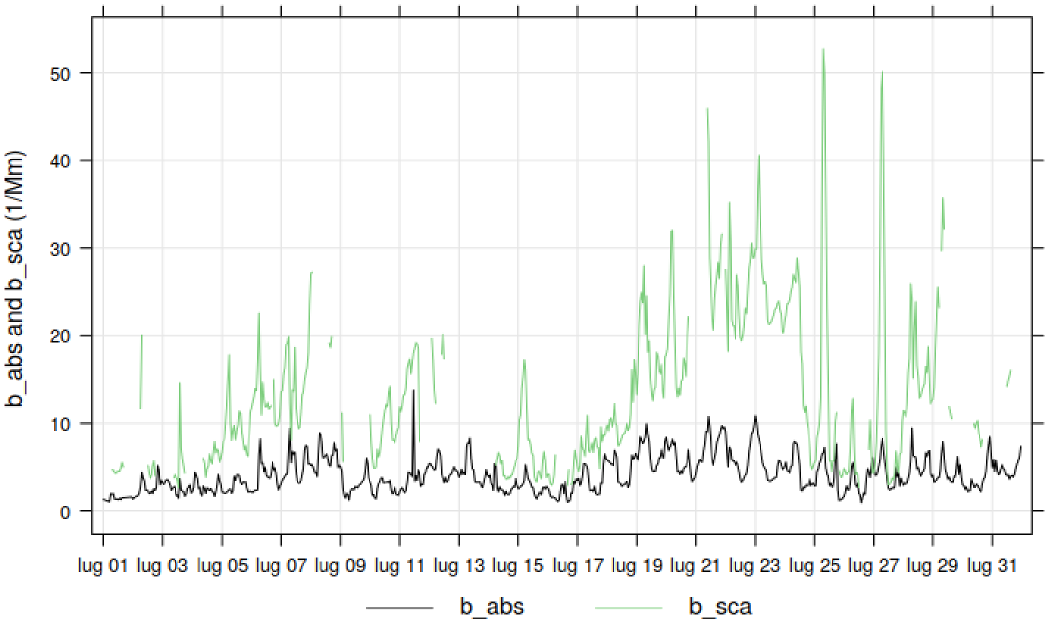

(a) *Babs and Bscat*

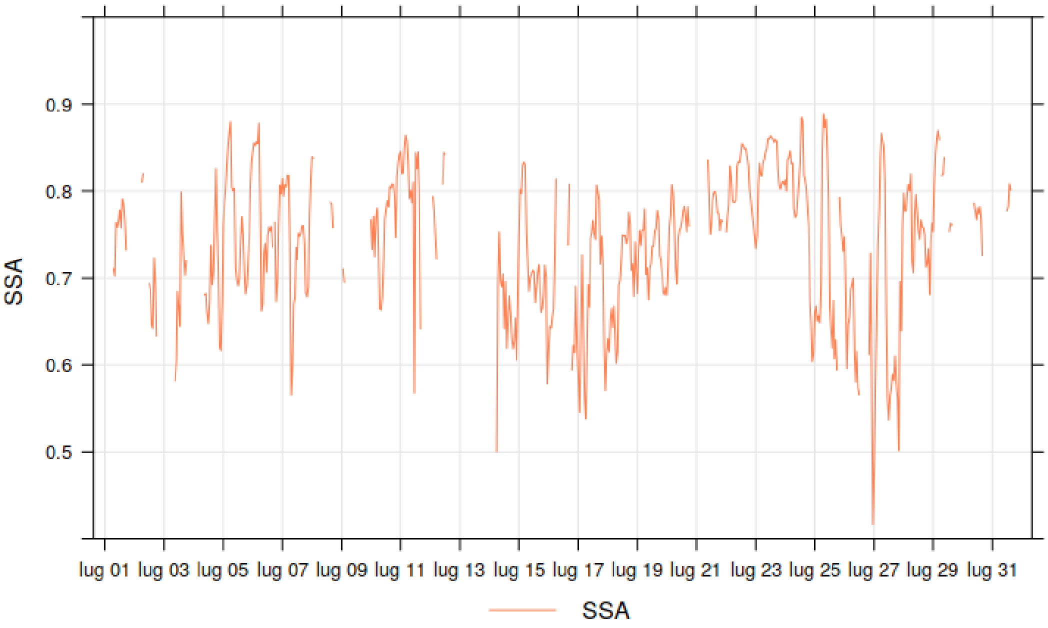

(b) *Single Scattering Albedo (SSA)*

Figure 4.32: Time series (time zone UTC+1) of hourly averaged values of: a) absorption and scattering coefficients; b) single scattering albedo. Measured or determined from values acquired by MAAP and Nephelometer at SPC site.

values of absorption but it is not possible to analyze the scattering coefficient because of high humidity levels. The 10th is also affected by dust transport and shows intermediate values of both coefficients. On 11 there was an high b_{abs} coefficient for a very short period associated with a lower peak in the scattering coefficient, probably associated with some local source.

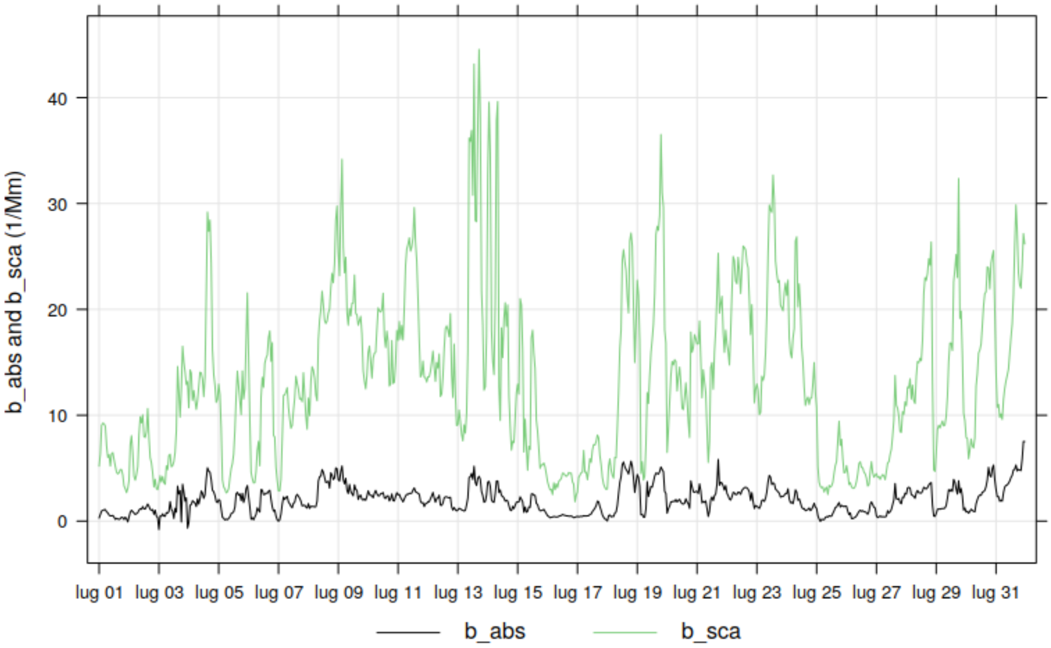

(a) *Babs and Bscat*

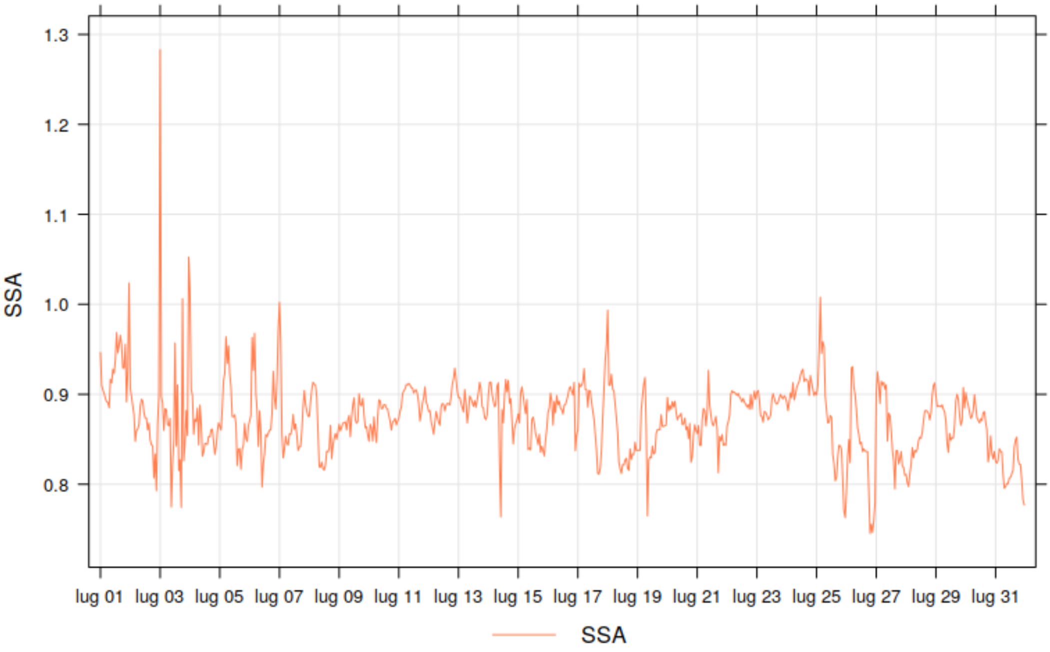

(b) *Single Scattering Albedo (SSA)*

Figure 4.33: Time series (time zone UTC+1) of hourly averaged values of: a) absorption and scattering coefficients; b) single scattering albedo. Measured or determined from values acquired by MAAP and Nephelometer at MC site.

A sustained period of high pollution level from 19 to 24 was then observed and was visible also in the time series of BO. This period was characterized by initial low values of SSA which slowly increase reaching values near 0.9 between 22 and 24. It is probably due to high levels of pollution throughout the region that the 22 and 23 add up to an episode of dust, which is associated with an increase in the SSA. On 25 and 27 in the morning there were very highly scattering particles but with low absorption coefficients, resulting in high SSA. While in the last part of the month, on 28, 29 and 31, there were high concentration of absorbing particles.

Figure 4.33 shows that the site of MC is characterized by a good correlation between scattering and absorption coefficients, which plots have approximately the same variability and common maximums and minimums. This correlation is confirmed by the behavior of the SSA, which remains roughly constant and high, with values in the range 0.8, 0.9, for the whole month.

(a)

(b)

Figure 4.34: Comparison between a) pressure, b) temperature and b_{abs} time series for MC site.

The main periods of minimum values are 1, 2, 16 and 17 and the 25 of july, while those with the highest concentrations are: 8 and 9, 18 and 19 and the last days of the month. Maxima and minima of both coefficients for this site are associated with common environmental characteristics. The three periods of low scattering and absorption coefficients are associated with low temperatures and pressure periods as can be seen in figure 4.34.

On the other hand high absorption and scattering coefficients are typically associated with periods of high temperatures and pressures, that can favor the accumulation of

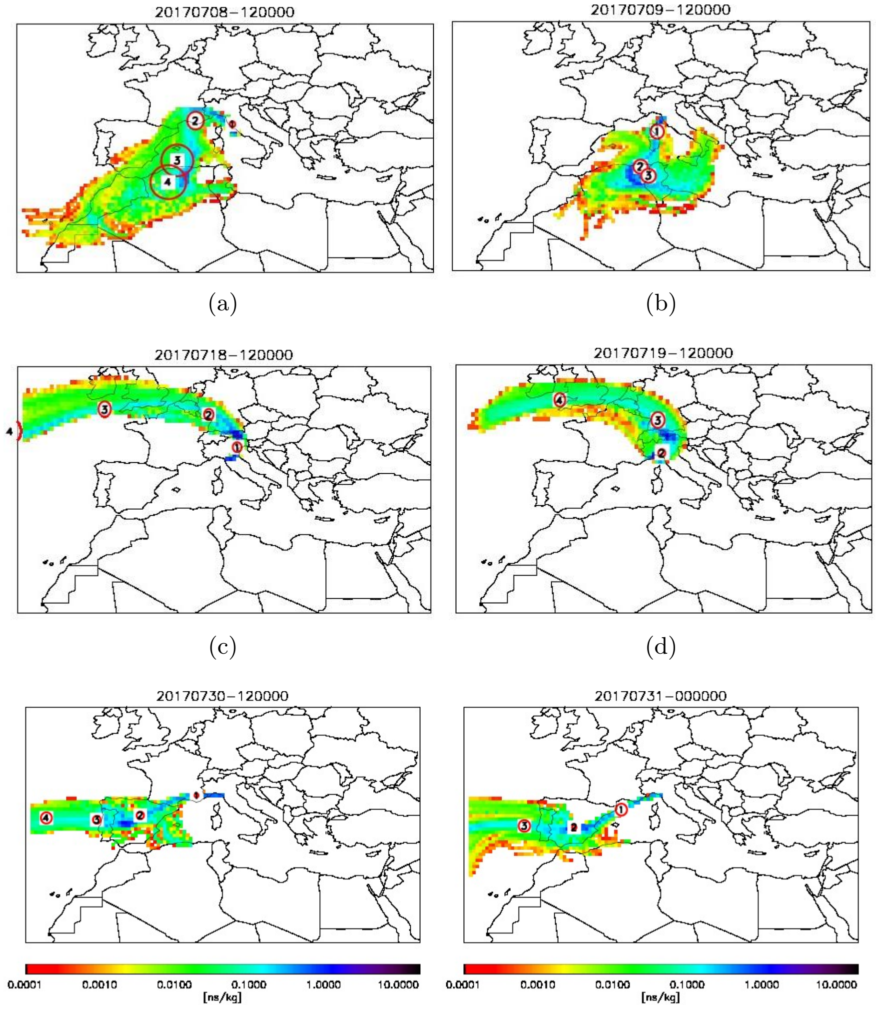

(a) (b)

(c) (d)

(e) (f)

Figure 4.35: Backtrajectories of air masses reaching the MC site on: a) 8; b) 9; c) 18; d) 19; e) 30; f) 31 July, by FLEXPART's simulations.

pollution in the close basin of Po Valley, as well as with air masses coming from south or circulating over the Po Valley as we can see in figure 4.35. The day 8 and 9 were characterized by air masses coming from Africa reaching the MC site passing through the Mediterranean sea and the east cost of Spain. The July 18th and 19th were then associated to air masses from the North of Europe, but reaching the site passing through the eastern part of the Po Valley. The 30 and 31 to air masses are from Spain and North Africa and we observe an increase of both absorption and scattering coefficients. In the mountain site of MC the highest concentrations of aerosols, which leads to maximum values of absorption and scattering coefficients are reached at the end of the month when a severe heat wave was approaching, linked to a high pressure system (figure 4.34 b). The subsidence over the Po basin and increase of temperature determined an accumulation of pollutants in the low levels of Po Valley, also reaching MC due to the growing height of the boundary layer. On the other hand, low temperature and pressure that favor high level transport, combined with air from the North are instead associated with low concentrations of pollutants.

Some dust events occurred in these anticyclonic periods as we can see in figure 4.36, in particular two weak events on 21 and 24 and a prolonged and strong transport from 7 to 10. The strongest event is characterized by high values of both coefficients in particular on 8 and 9 that remain sustained and with less diurnal variation until the 11th. The SSA shows a weak decrease up to about 0.8 on the 8th but stays close to 0.9 in the rest of the period.

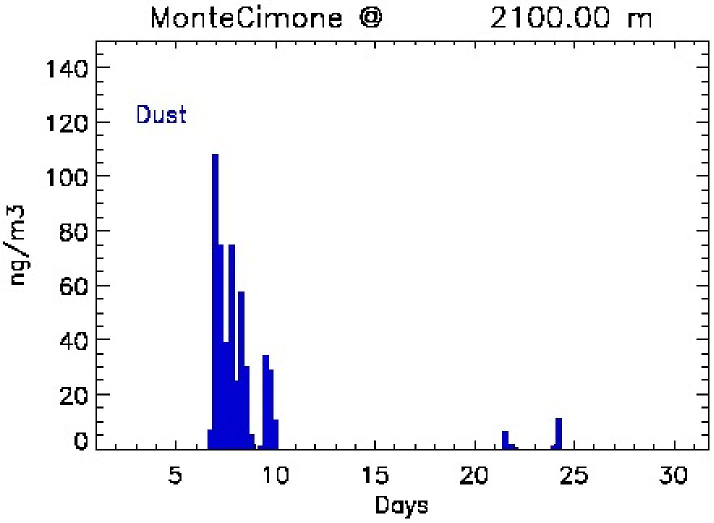

Figure 4.36: Identification of dust events at MC.

4.4.2 Diurnal and weekly variations

The typical diurnal behavior of b$_{abs}$, b$_{sca}$ and SSA in the measurement period considered in this study, is shown in figure 4.38, where the mean and the interval of 95% of confidence are depicted. Typically, the daily cycle of these variables, especially in a summer month such as July, is the result of the combination of the variability of the emission sources, linked to the daily and productive activities of humans and photochemical processes, and of the dynamic of air masses, mainly related to the height of the PBL and regional circulation. The PBL in which the pollutants are confined, remains stable and slight during the night, because of low temperatures at the surface, but grows and become unstable during the day, when the insolation on the ground causes the development of convective movements that mix the pollutants with the cleaner air above. The concentration of particles in the different sites, are affected by PBL height and evolution, depending on their altitude. In addiction when PBL drops it can cause an increase in horizontal motions and therefore an increase in the wind at the surface, that further influences the concentration of particles in the atmosphere. To give an idea of the variability of this layer, the figure 4.37 shows the diurnal variations in temperature and wind speed at the three sites studied.

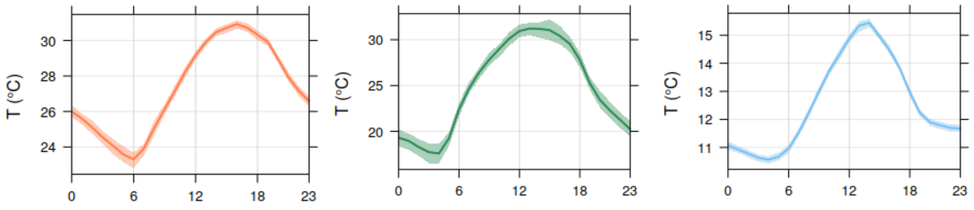

(a) *BO* (b) *SPC* (c) *MC*

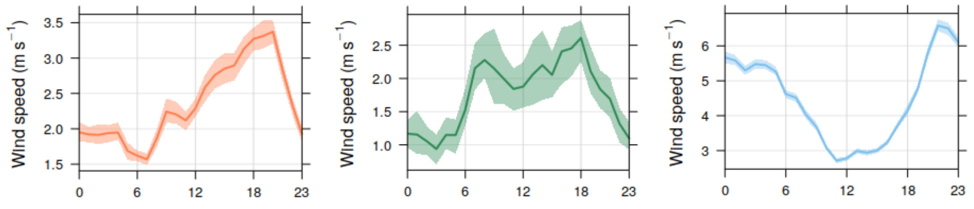

(d) *BO* (e) *SPC* (f) *MC*

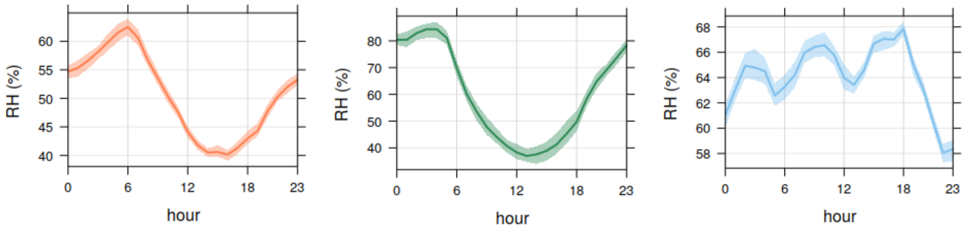

(g) *BO* (h) *SPC* (i) *MC*

Figure 4.37: Diurnal variations in temperature, humidity and wind speed for all the three sites.

Temperature variability was the same for all the three sites and follows that of diurnal insolation, with a minimum early in the morning and a maximum in the afternoon. The wind diurnal cycle was similar for BO and SPC, with low values during the night, a maximum late in the afternoon and a variable behavior for the rest of the day. At MC the minimum is recorded in the central hours of the day, when the temperature is higher and a maximum during the night, when stronger winds connected to larger scale circulation are dominant.

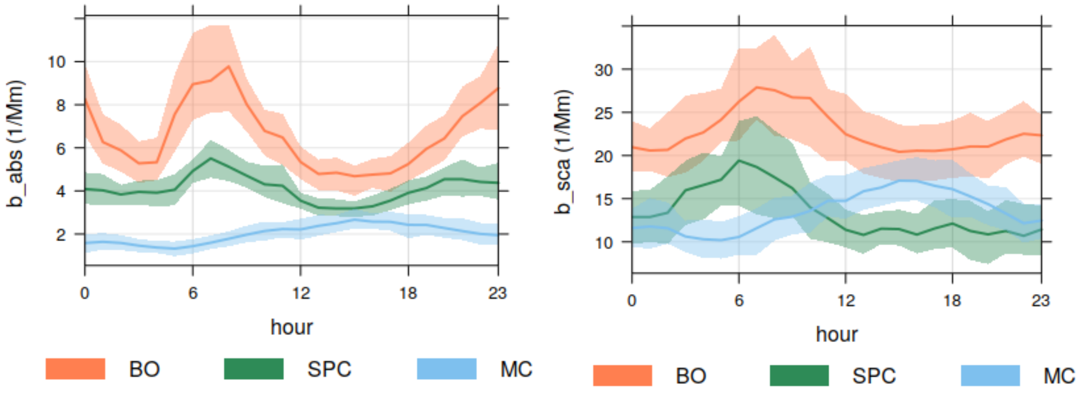

(a) *Absorption coefficient (1/Mm)* (b) *Scattering coefficient (1/Mm)*

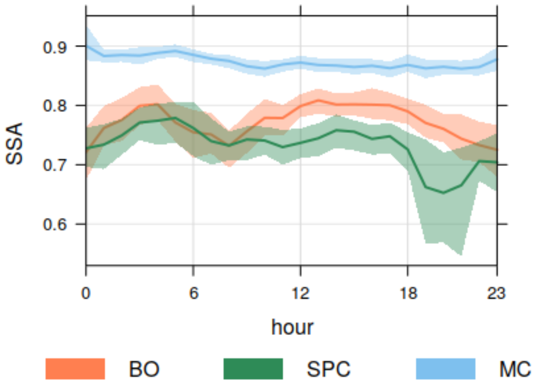

(c) *Single Scattering Albedo*

Figure 4.38: Diurnal variations in absorbing and scattering coefficients and in the single scattering albedo.

The absorption coefficient in figure 4.38a shows a very similar behavior at the BO and SPC sites, with the main difference being less wide oscillations in the second. The rapid increase in the early morning is clearly linked with the rush hour of the morning traffic and it is weaker in SPC, because intense sources are further away from the site. A second less intense maximum is due to the evening traffic; the values drop during the night reaching a minimum in the early morning, before sunrise. In the early hours of the day, as human activities begin and traffic on the roads develop, this increases to a maximum at around 8:00 in the morning when the simultaneous increase in the height of the PBL, inhibits the climb and causes a progressive decrease. A minimum is reached in the afternoon when the height and therefore the mixing of pollutants is maximum and at the same time the vehicular traffic becomes less intense. Towards evening a new increase in traffic accompanied by a decrease in the height of the PBL cause a new peak. This trend is therefore in good agreement with what can be expected from an urban site, very influenced by human activities and the delay in the increase that can be observed in the rural site (SPC) may be due to the fact that it has fewer local sources and is more influenced by transport from nearby and more polluted areas.

The scattering coefficient at BO and SPC sites, shows a similar trend but with a much lower or even absent peak in the evening and a less intense one that lasts longer in the morning. This behavior may be due to the production of secondary aerosols, which have a more direct influence on the scattering component of particulate matter and which are more effective during the day than during the evening when the absence of sun prevents photochemical reactions. The SSA then shows two valleys at times when traffic pollution is highest, so in the morning and in the evening, with that present at SPC during the evening probably so accentuated due to a combination of events on some days at that precise time.

On the other hand, it has higher values at night and during the day when the reduced traffic cannot compensate for the more constant and variable in sources scattering aerosol production. The diurnal variation at MC is very different from the previous ones, with low values in the morning and a maximum in the afternoon, both in terms of scattering and absorption. The main driver of diurnal cycle is the strong influence of valley winds transporting air from PBL, increasing the concentrations of pollutants in this site. Being a site at a very high altitude of 2175 m, it is generally above the upper limit of this layer and is therefore characterized by free tropospheric air masses.

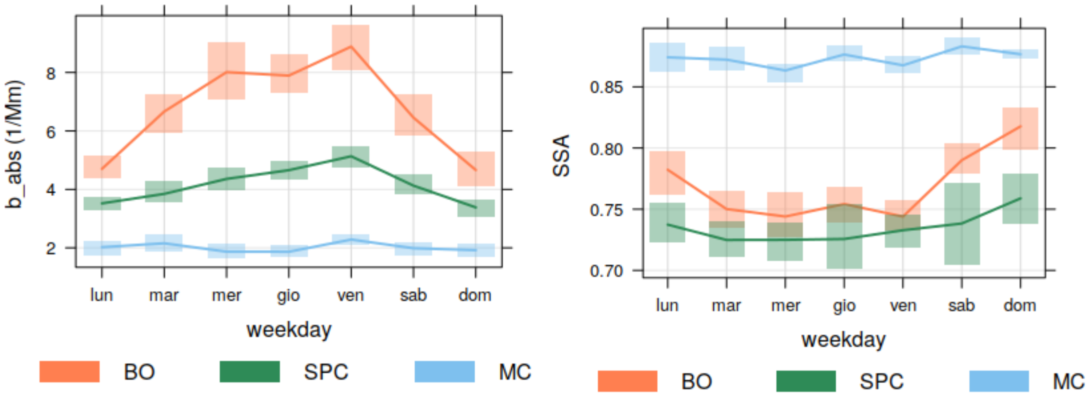

(a) *Absorption coefficient (1/Mm)* (b) *Single Scattering Albedo*

Figure 4.39: Weakly variations of b_{abs} and SSA in all the three sites.

The figure 4.39 finally shows the changes that have occurred during the week. Although for the month of July we would expect to find a strong influence of the absorbing component in the last part of the week, due to the typical movements to the coast this season, what we see is instead a high concentration of absorbing particles during the week and lower values at the weekend.

The low concentrations in BO and SPC during the weekends are also characterized by higher SSA, indicating the lower influence of traffic and/or other combustion sources to aerosol composition. At Monte Cimone no clear weakly cycle is evident, indicating the influence from boundary layer is not dominant in the aerosol properties and concentrations.

4.5 EC mass concentrations and mass absorption cross section

The mass concentration of EC measured with the thermo-optical technique is considered the best indicator of the presence of carbonaceous aerosols consisting of pure refractory carbon with a graphite structure, distinct from organic carbon, another dominant component of particles emitted by combustion processes, in which carbon is linked to other elements. It is considered as the real component of the particulate matter having strong absorption of solar radiation without deep dependence on the wavelength, that could be defined as Black Carbon. During the ACTRIS-2 Monte Cimone Po Valley campaign, aerosol was collected on quartz filters for EC determinations, these measurements are summarized with the box and whiskers plots in figure 4.40 that show the median, the 25th and 75th percentile together with the extreme values, in each site considered.

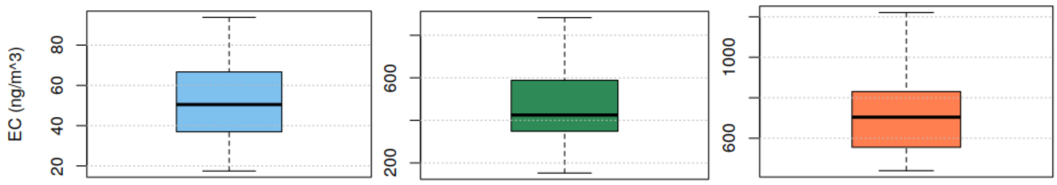

(a) *MC* (b) *SPC* (c) *BO*

Figure 4.40: Boxplots showing the median of the values, the first and third quartile and maximum and minimum values of EC mass concentration in ng/m^3 in: a) MC; b) SPC; c) BO.

The average values and standard deviations obtained are: 50 ± 12, 471 ± 3 and 720 ± 5 ng/m^3 and 22, 190, 275 ng/m^3, at MC, SPC and BO respectively. BO being an urban site affected by a variety of combustion sources, is the most polluted among the three. MC has the lowest concentrations being a mountain site, and SPC, a rural one, shows intermediate conditions. Comparing the values with those found from a phenomenology paper, derived from ACTRIS network (Zanatta et al. 2016), there is a good agreement for environments of the same type. In fact the polluted site of Ispra, for example, has a summer geometric mean of 630 ng/m^3 with geometric standard deviation of 130 and the mountain site of Puy de Dome has a summer geometric mean of 73 ng/m^3 and geometric standard deviation of 136. At the MC site, the particles were collected on a filter in periods of time that made it possible to distinguish between day and night concentrations. For these the averages are respectively 70 ± 20 ng/m^3 and 46 ± 14 ng/m^3, in agreement with what we could expect from a mountain site in which pollution derives primarily from transport processes from the plain and reach it mainly during the day.

The figures 4.41 then show how the EC values vary over time by comparing their trend with that of the absorption coefficient at 637 nm, i.e. a wavelength in which it is assumed that this is almost entirely due to the BC. The values of b_{abs} before comparison were averaged over the same acquisition period as the EC samples and reported in the graph with a scale allowing to compare them directly. Patterns are very similar in BO, similar but with some discordant days in SPC, while a clear shift is visible for MC. The values of Bologna and San Pietro where considered valid and consistent with other measurements, while the Monte Cimone ones need more investigation and eventual correction factor determination, probably linked with the sampling dichotomous system. The behavior at BO and SPC shows that the two quantities are actually well bound with a consistent MAC. The value obtained for MC (46 ± 7 m^2/g) is clearly unrealistic and need to be explained in other framework. The monthly averages of the MAC calculated from the observations made at the other two sites are equal to: 46 ± 7 m^2/g at MC, 9.2 ± 1.4 m^2/g at SPC and 9.4 ± 1.4 m^2/g at BO. With standard deviations of 23, 2.2, 1.8 m^2/g. The values calculated at BO and SPC are well comparable with the range typically observed for this quantity which is between 4.3 and 22.7 m^2/g. There seems to be no difference between the two sites and a value of about 9.3 ± 1.4 can be considered as representative of the Po Valley background for the measurement period considered, at a wavelength of 637 nm.

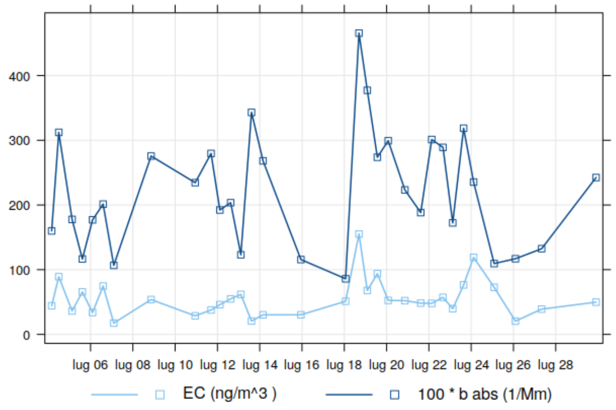

(a) *MC*

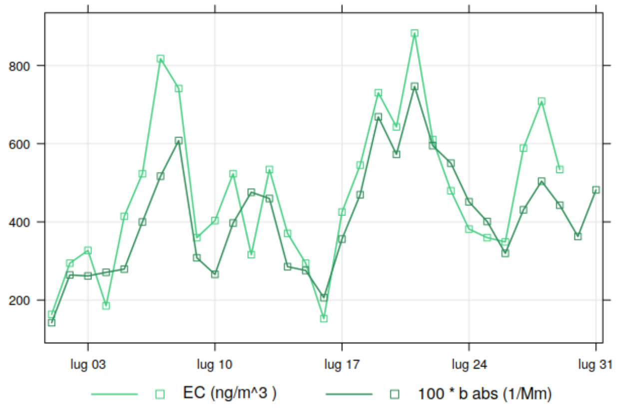

(b) *SPC*

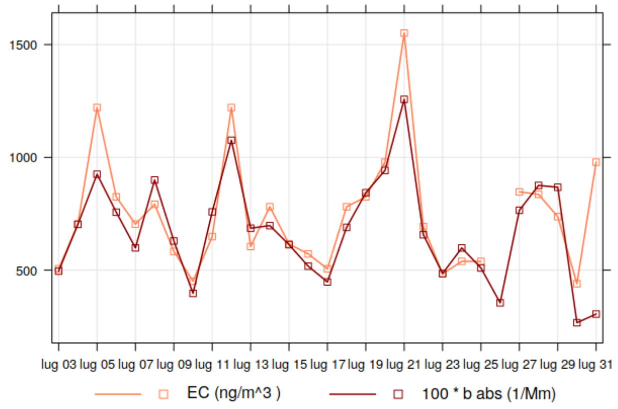

(c) *BO*

Figure 4.41: Time series (time zone UTC+1) of EC and b$_{abs}$ values measured in the three sites of: a) MC; b) SPC; c) BO.

There are many possible sources of bias in these values that cause additional uncertainties in the value compared to those considered for b$_{abs}$ and EC. The absorption value as well as the Angstrom exponent can be influenced by the presence of absorbing particles other than black carbon. Organic carbon and dust, even though they have very little influence on the absorption at 637 nm, have an effect and can determine positive bias in the absorption that causes an overestimation of the MAC. In Zanatta et al. 2016 it is estimated that this can cause a bias of about 10 %. As far as dust events are concerned, in addition to the possible slight overestimation in absorption, there may also be an overestimation of the EC due to a misinterpretation of carbonates as EC, which in the case of large particles, such as dust particles (coarse mode) in dust events can cause a negative bias in the MAC (Karasinou et al. 2015, Zanatta et al. 2016). Another possible source of bias that causes an increase in absorption and therefore an overestimation of the MAC is the lensing effect caused by the coating around the BC cores that is formed during the aging processes because of vapor deposition on the particle surface and mixing with other particles. But even taking into account a possible increase in MAC due to aging of BC during transport from the plain and possible bias due to the presence of large amounts of organic material, such a high value is not realistic. Moreover the ratio between absorption and EC stay quite constant along the month, suggesting the possibility of a problem of accuracy in EC determination. The scatterplot in the figure 4.42, in which the values corresponding to EC samples collected during the night were highlighted in dark blue, those collected during the day in blue and those corresponding to samples collected over several days in orange, further confirms the lack of correlation by distinguishing between these three types of samples. In fact, a different aging degree could result in different MAC between day and night. This suggests that there may have been errors in the measurement procedure. The daily averages of the MAC values at the two sites of BO and SPC are finally shown in the figure 4.43. From an analysis of these plots and of the values of the standard deviation it can be seen that the temporal variability at BO is rather limited with a standard deviation slightly higher than the uncertainty and probably due in large part to the very low value observed on 31 July. SPC, on the other hand, is characterized by greater variability, with some very marked positive peaks on 4, 12, 16 and between 23 and 25. The higher values can be related to transport of aged aerosol, in which MAC is amplified because of the lensing effect, while in Bologna the presence of fresh particles is dominant. The last period of the campaign is characterized by a decrease of the MAC

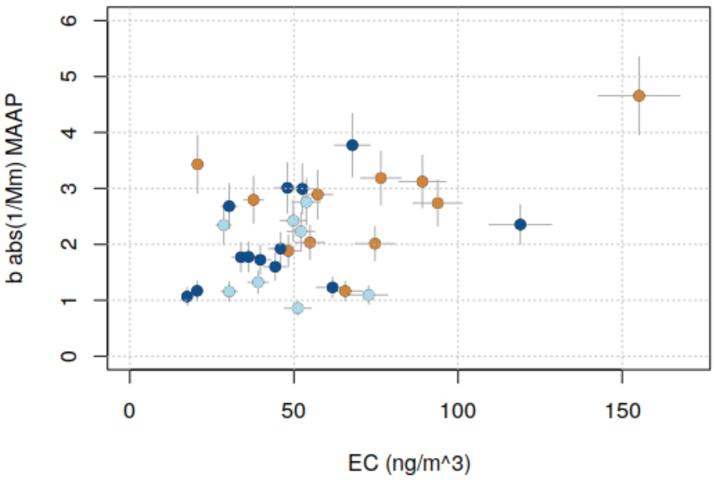

Figure 4.42: EC from thermo-optical method VS b$_{abs}$ measured by MAAP at MC site highlighting in blue the ones from filters collected during the night, in orange those collected during the day, in blue those obtained from filters collected over more than one day.

value, in Bologna.

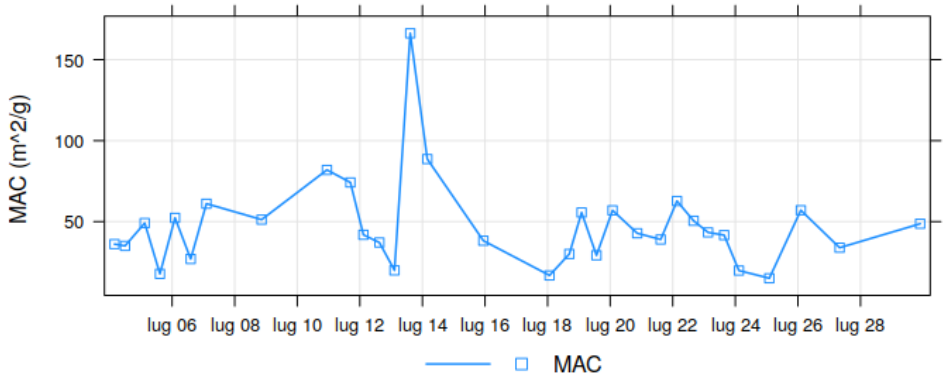

(a) *MC*

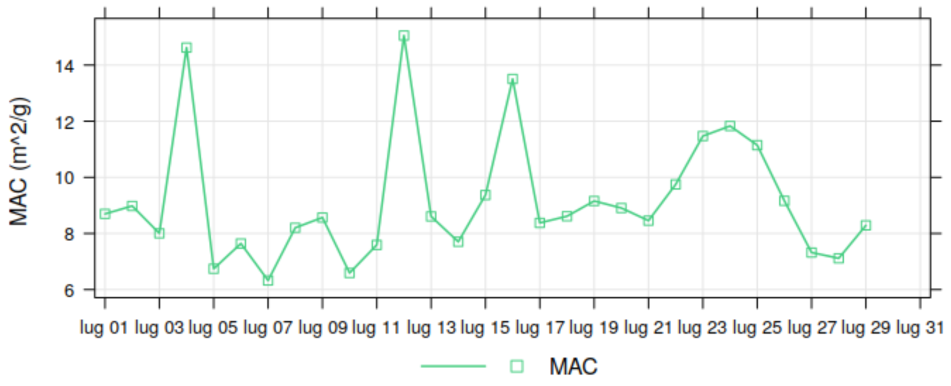

(b) *SPC*

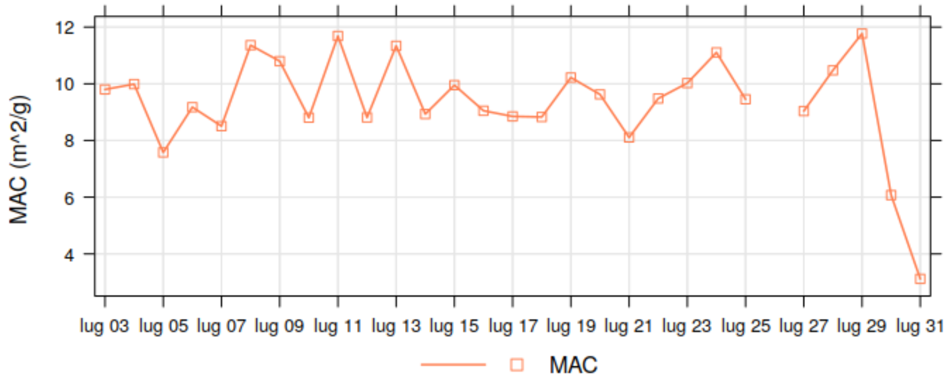

(c) *BO*

Figure 4.43: Time series of MAC values measured in the sites of: a)MC; b) SPC; c) BO.

4.6 Absorption and scattering Angstrom exponents

Finally, the dependence of the scattering and absorption coefficients on the wavelength of the incident radiation was analyzed to obtain information on the particles dominant composition. The overall characteristics of their variability on the whole month and at all sites, are described by the statistical parameters (mean, median, st. dev., 5th and

95th percentile) listed in table 4.7. The mean and standard deviation of AAE (from AE31) in BO were 1.2 ± 0.6 and 0.2, at SPC were 1.1 ± 0.6 and 0.1, at MC were 1.1 ± 0.6 and 0.2. Those derived by AE33 were 1.3 ± 0.6 and 0.1 at SPC and 1.3 ± 0.6 and 0.2 at MC. AE33 therefore tends to overestimate the values obtained from the AE31 even if given the great uncertainties are not very different. The mean and standard deviation of SAE were instead 1.9 ± 0.3 and 0.3 in BO, at SPC were 1.5 ± 0.3 and 1, on MC were 1.8 ± 0.3 and 0.3. Figure 4.44 shows also the variation of AAE hourly averages as a function of SAE and SAE as a function of SSA.

					Percentiles	
Site	Parameter	Mean	St. Dev.	Median	5	95
MC	AAE	1.06	0.21	1.06	0.66	1.41
	SAE	1.78	0.33	1.87	1.05	2.20
SPC	AAE	1.12	0.13	1.13	0.9	1.29
	SAE	1.45	0.98	1.84	-0.8	2.28
BO	AAE	1.17	0.21	1.16	0.95	1.45
	SAE	1.87	0.29	1.93	1.26	2.25

Table 4.7: Statistical analysis of AAE and SAE on the whole month of measure at the three measurement sites.

From these it can be seen that the average and median of the AAE remain very close to 1 for all three measurement sites, with very limited standard deviations over the month. The values are very close to the AAE of pure BC particles that is widely accepted to be 1.0, although observational estimates give quite a wide range of 0.6 to 1.3. This indicates that the absorbing particles on the filter are mostly BC with a limited influence of dust or BrC, that absorb much more in the shorter wavelengths. Anyway AAE also depends from sizes and refractive index, making difficult to make strong assumptions only based on AAE values.

At BO and MC sites the range of variation of this parameter is pretty similar, but is shifted to slightly higher values at BO and with larger variations, probably due to a greater influence of absorbing organic carbon. At SPC the average and median are intermediate compared to the other two sites and the standard deviation is smaller, indicating an even stronger dominance of pure BC over the absorbing aerosol population. The average and median values of the SAE are all very similar between the three sites and are in all cases quite high, indicating a dominance of scattering particles with high wavelength dependence and therefore small sizes, especially in BO. This indicates that the entire region in the measurement period is characterized mainly by small freshly emitted particles. The highest values were recorded at BO, in accordance with vicinity to the direct sources from combustion processes, while lowest valid values were measured at MC, showing the larger variability of aerosol types. The remote site of Monte Cimone, despite the predominance of small BC particles, is also characterized by few coated large particles and dust, most probably long range transported to the measurement site. The SPC very low values are considered unrealistic. However, these are concentrated at times when the concentrations, although high enough to make the b_{sca} greater than the detection limit, were still very low. The effect may therefore be due to a low signal-to-noise ratio rather than to a higher actual scattering at larger wavelengths. Comparing these parameters also to the SSA it can be concluded that BO and SPC are characterized in the month of measurement by small and freshly emitted particles with BC dominance in the absorbing component, present at high percentages compared to the scattering one. While at MC there are far fewer absorbing particles but still small in size and mostly consisting of BC.

In the figure 4.45 the time series of daily averages of AAE and SAE compared to

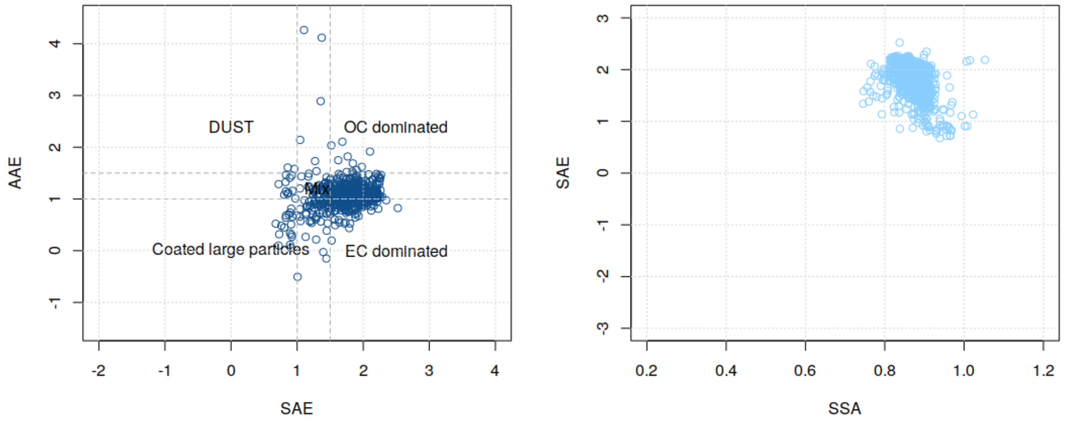

(a) *AAE VS SAE (MC)* (b) *SAE VS SSA (MC)*

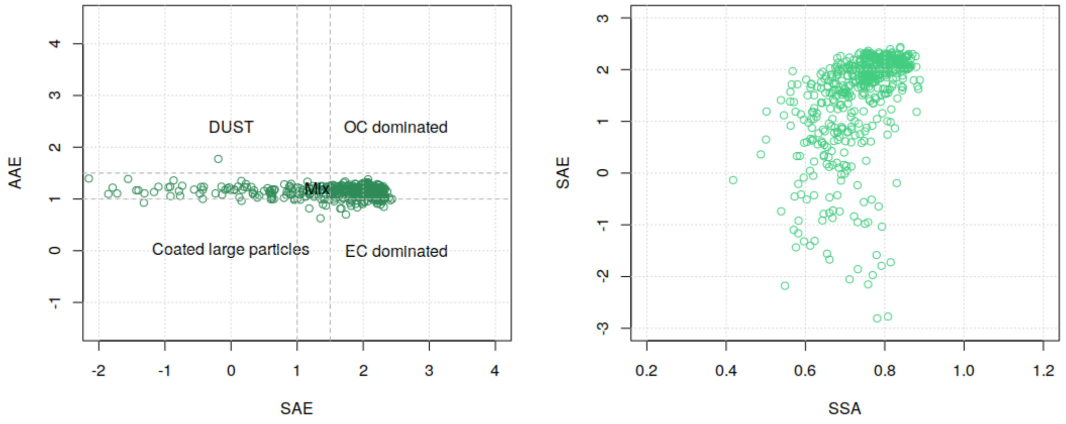

(c) *AAE VS SAE (SPC)* (d) *SAE VS SSA (SPC)*

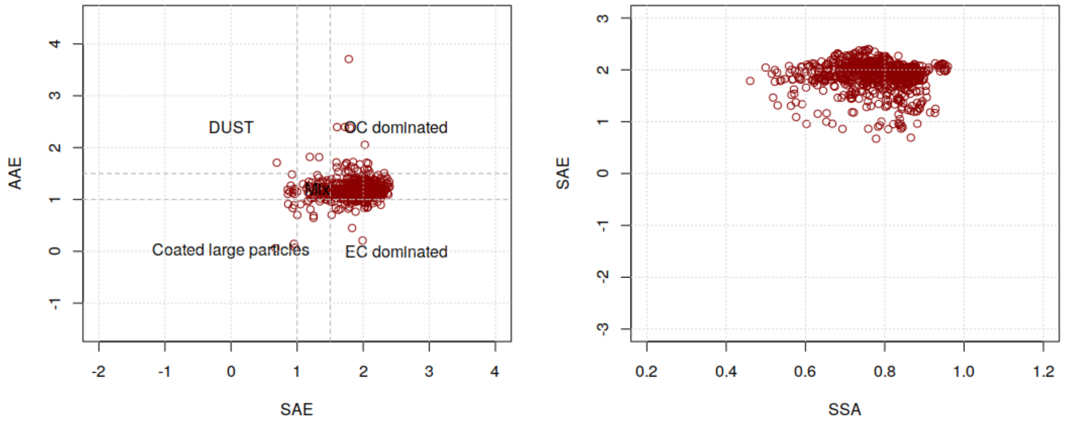

(e) *AAE VS SAE (BO)* (f) *SAE VS SSA (BO)*

Figure 4.44: Scatter plots of hourly averaged values of AAE in function of SAE, and SAE in function of SSA.

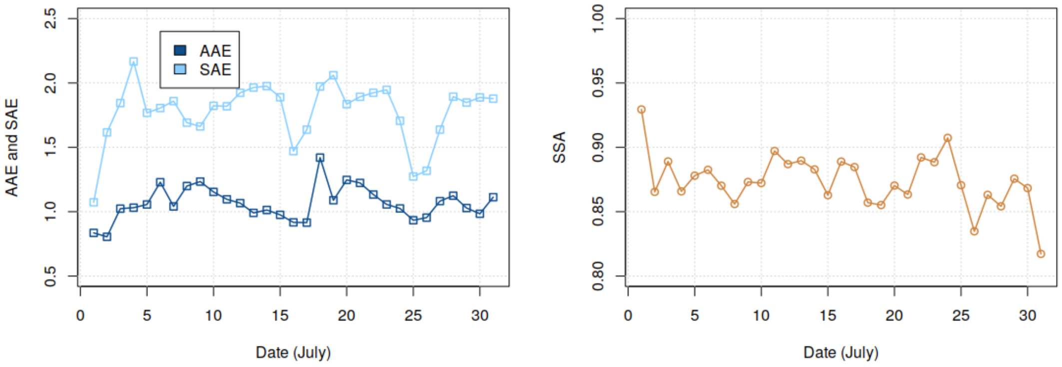

(a) *AAE and SAE (MC)* (b) *SSA (MC)*

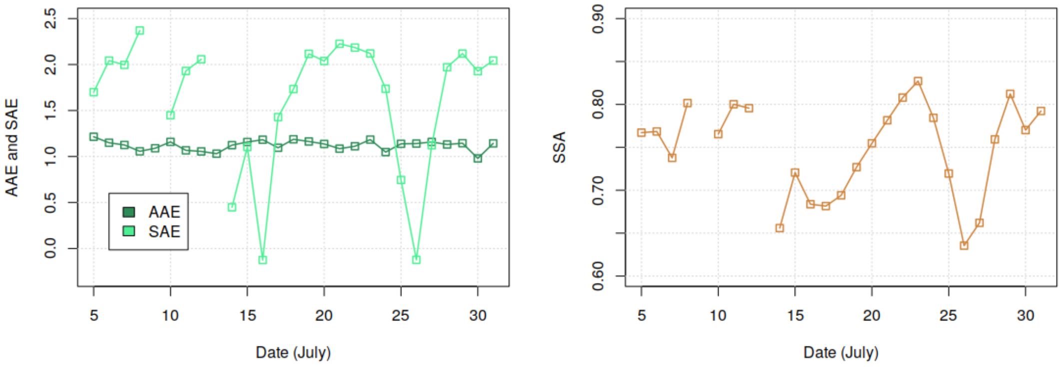

(c) *AAE and SAE (SPC)* (d) *SSA (SPC)*

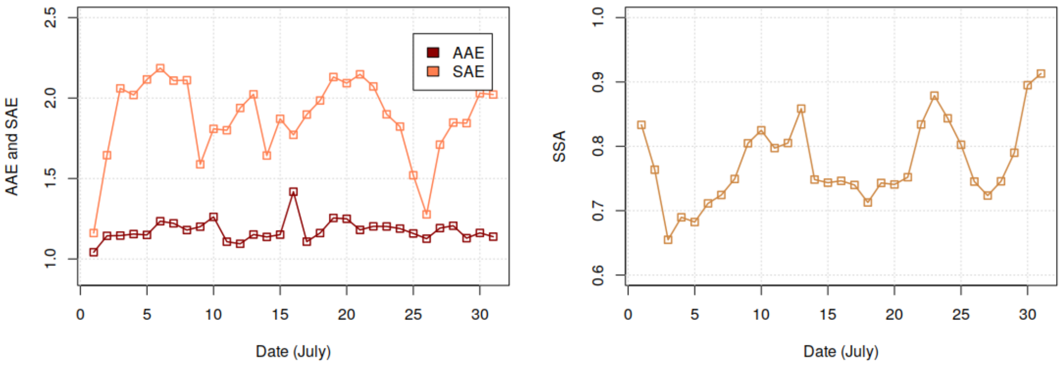

(e) *AAE and SAE (BO)* (f) *SSA (BO)*

Figure 4.45: Time series (UTC+1) of daily averages of AAE, SAE and SSA, measured at: a) b) MC; c) d) SPC; e) f) BO on the whole month.

those of the SSA are shown. SAE values tend to be more uncertain at the very low scattering coefficient values. The negative peaks that are present in all stations on July 1st, 2nd, 16th and 26th are probably due to very low signal-to-noise ratios rather than to a real diurnal variability of this parameter. The same is true for the AAE at its peak on 16 July where the very high value is associated with extremely low b_{abs}. Leaving aside these periods, the days when the SAE has reached particularly low values or AAE high ones are illustrated in more detail in the following figures. In the first one (figure 4.46) the days of 8 and 9 July at the sites of MC and BO are displayed. There are a few hours when the SAE becomes particularly low and the AAE has positive peaks. This pattern suggest the presence of large coarse particles, with larger absorption dependency on the wavelength than for pure BC, attributable to dust particles and in accordance with events visible in the backtrajectories, as well as from the simultaneous low SAE values. At both MC and BO these are also associated with higher than average SSA values. These two days showed episodes of dust also at SPC but it was not possible to analyze the variability in detail because of the high values of relative humidity.

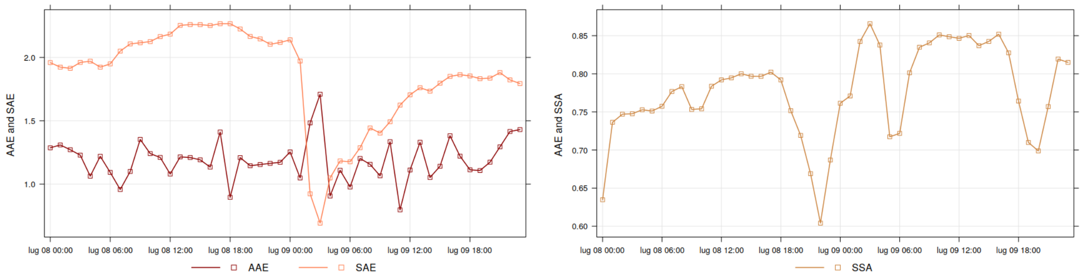

(a) *AAE and SAE (BO)*

(b) *SSA (BO)*

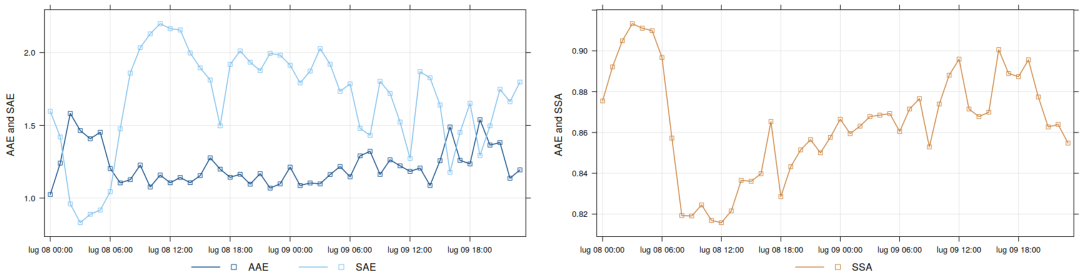

(c) *AAE and SAE (MC)*

(d) *SSA (MC)*

Figure 4.46: Time series (UTC+1) of hourly averages of AAE, SAE and SSA, measured at BO (a, b) and MC (c and d), on 8 and 9 July.

Looking at the behavior of these parameters in correspondence with other significant episodes of dust, recorded in all three stations on July 10 and at the MC on July 21, it can be seen that the instruments do not always measure significant variations in AAE and SAE. On the 10th at the MC there are corresponding, even not very intense peaks, showing simultaneous increase of AAE up to 1.4 and weak decrease of SSA to the same value. The SSA around 0.87 and SAE in the range of small particles suggest a sudden and short advection of aerosol with organic coating. On the 20th and 21st the values of AAE remain quite high with several points where they rise above 1.5 associated with SAE between 2 and 1.5. On the 10th at SPC the values of AAE remain about constant while those of SAE show two big decreases suggesting coarse particle presence, probably local dust resuspended, while at BO the SAE change very little while there are some peaks of AAE.

At SPC there are also three other moments of strong decrease of SAE with about constant AAE and low SSA, the 14 and 15, the 17 and the 27 and 28 (figure 4.49). That

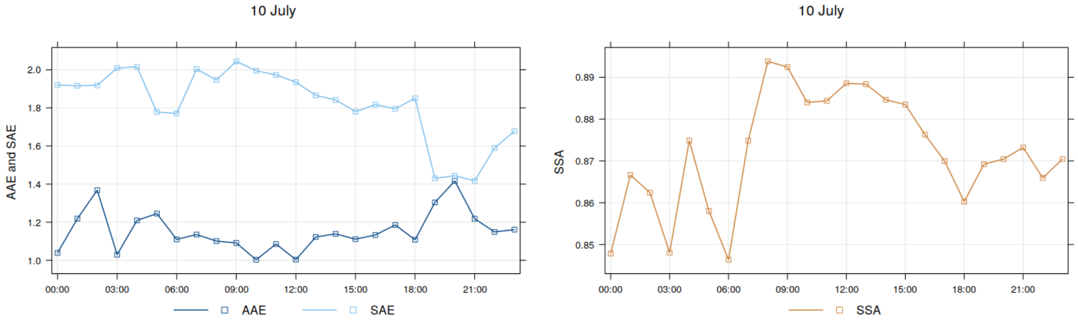

(a) *AAE and SAE (MC)* (b) *SSA (MC)*

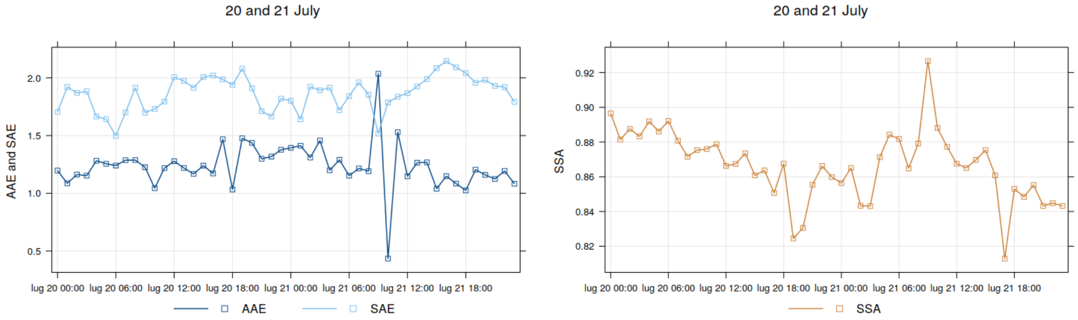

(c) *AAE and SAE (MC)* (d) *SSA (MC)*

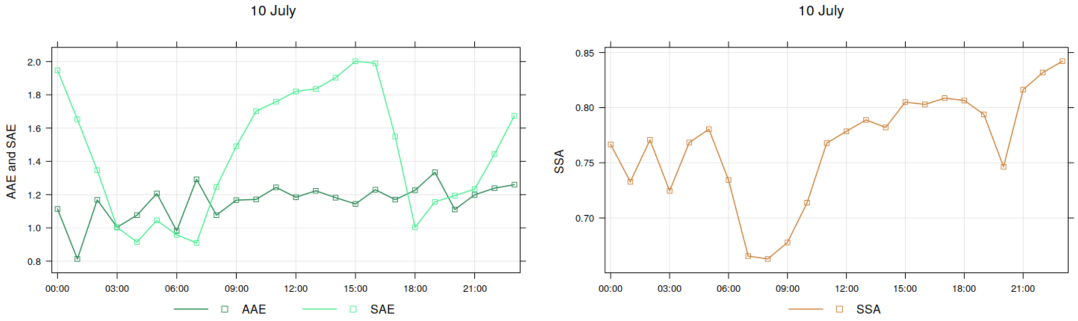

(e) *AAE and SAE (SPC)* (f) *SSA (SPC)*

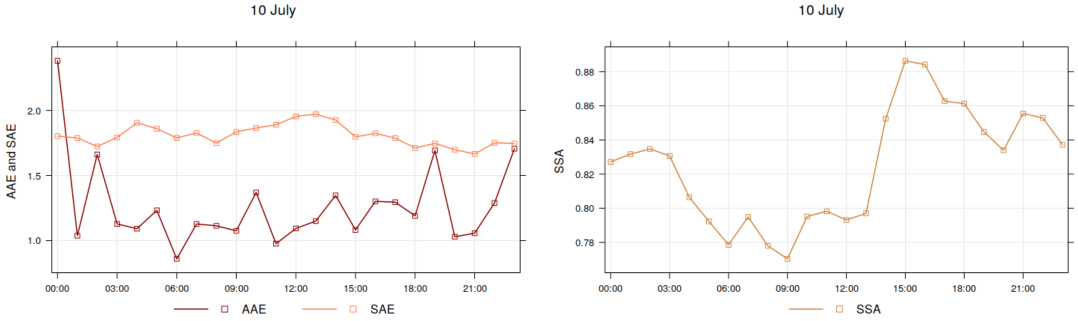

(g) *AAE and SAE (BO)* (h) *SSA (BO)*

Figure 4.47: Time series (UTC+1) of hourly averages of AAE, SAE and SSA, measured: a) b) at MC on 10 July; c) d) at MC on 20 and 21 July; e) f) at SPC on 10 July; g) h) at BO on 10 July.

on 17 may be due to large uncertainty, because of low values of b_{sca}, the 13 and 14 is probably due to periods with few measurements of b_{sca} because of high humidity, the 27 and 28 being days with peaks in both absorption and scattering may be due to large particles with a thick coating, nevertheless the low values of the MAC recorded in these two days. Finally in BO we observe three periods with peaks of AAE but associated with SAE rather high on 10, 24 and 27 and 28 (figure 4.48). These all have rather high and variable AAE values and few moments of slight decrease in SAE, which could be due more to periods with high OC concentrations than to dust. Such a detailed analysis of these parameters remains however very difficult. The strong influence of the higher concentrations of fine particles, with absorption little dependent on the wavelength well mixed with the others in the summer period, remains dominant preventing the instruments from perceiving changes in optical properties.

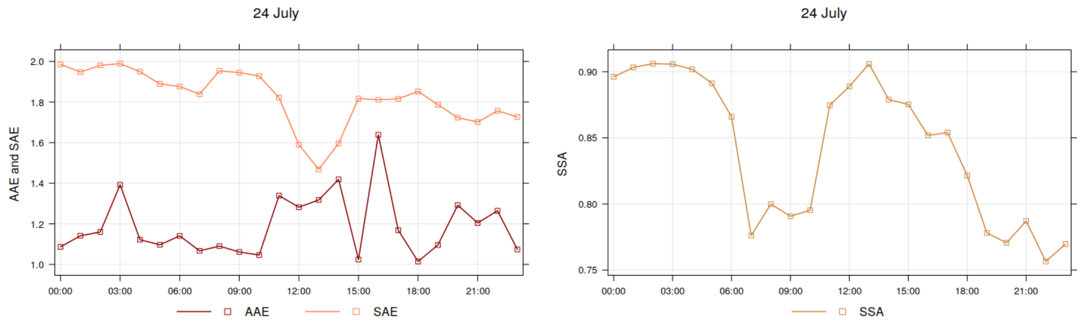

(a) *AAE and SAE (BO)* (b) *SSA (BO)*

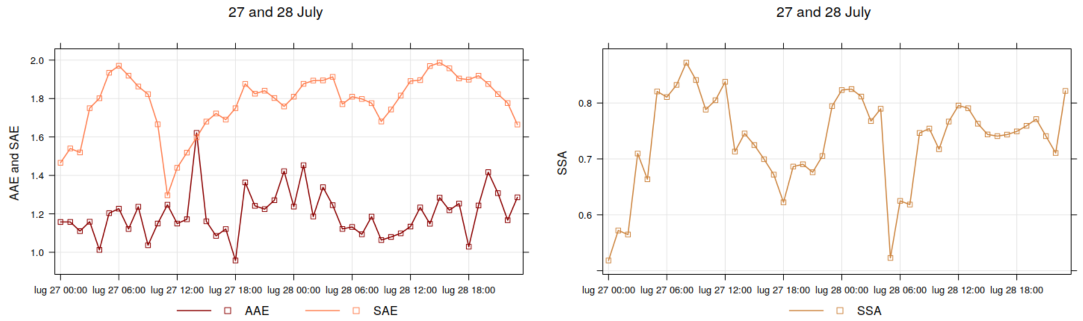

(c) *AAE and SAE (BO)* (d) *SSA (BO)*

Figure 4.48: Time series (UTC+1) of hourly averages of AAE, SAE and SSA, measured in BO: a) b) on 24 July; c) d) on 27 and 28 July.

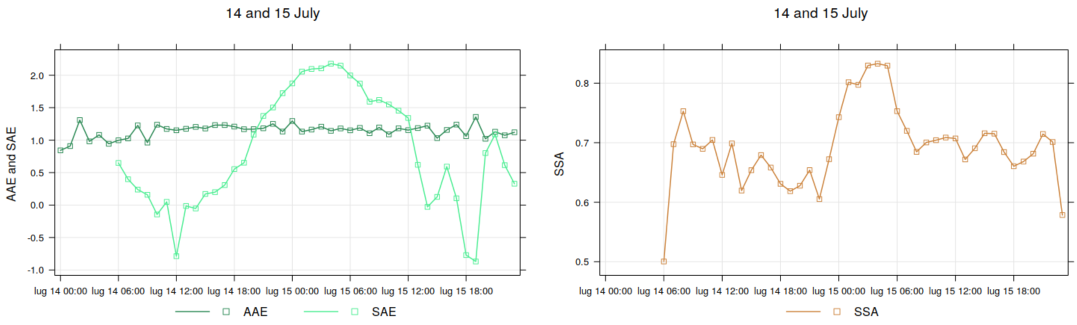

(a) *AAE and SAE (SPC)* (b) *SSA (SPC)*

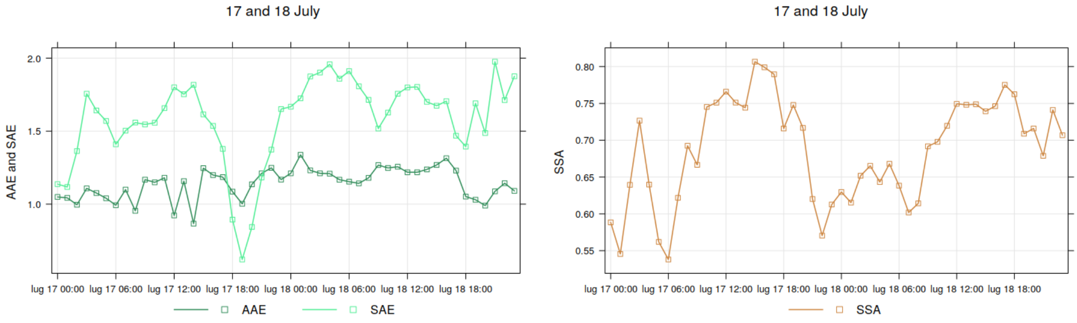

(c) *AAE and SAE (SPC)* (d) *SSA (SPC)*

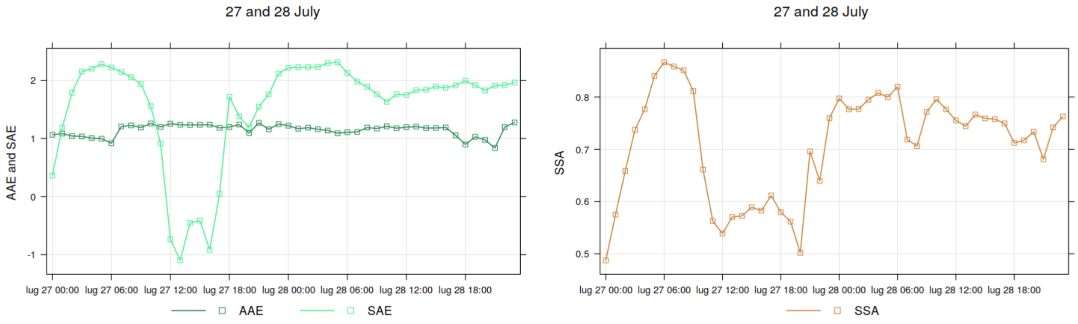

(e) *AAE and SAE (SPC)* (f) *SSA (SPC)*

Figure 4.49: Time series (UTC+1) of hourly averages of AAE, SAE and SSA, measured at SPC on: a) b) 14 and 15 July; c) d) on 17 and 18 July; e) f) on 27 and 28 July.

In the figure 4.50 the diurnal variations of the two exponents are shown. The AAE also remains more or less constant with little oscillations throughout the day, considered negligible in the diurnal cycle. SAE instead remains nearly constant throughout the day at BO with a very slight increase around noon which could simply be associated with the progressive increase of small particles, produced by secondary processes throughout the morning, while the freshly emitted rush hour can have associated a small contribution from resuspension. The diurnal behavior of MC fully reflects the trend in concentrations indicating an increase in fine particles coinciding with the increased transport of pollutants from polluted low levels. Finally, the SPC pattern is more uncertain and reflects the great variability and oscillations that occur in this site, where there is a large decrease throughout the day that could be linked to the wind lifting of larger soil particles from agricultural land or the condensation of vapour that increases the size of the particles, in agreement with Bucci et al., 2018.

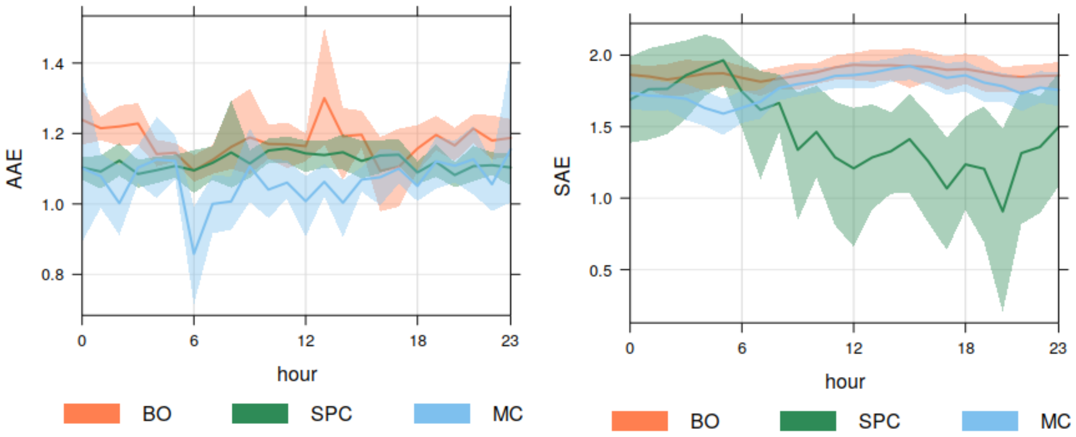

(a) *AAE*

(b) *SAE*

Figure 4.50: Diurnal variations of AAE and SAE (UTC+1).

The analysis presented in this chapter of these two parameters derived from optical properties, shows the difficulty of obtaining clear information, especially when present in low concentrations, the need of a perfect control of sample conditions (especially in term of drying) and the high uncertainties that characterize the Aethalometers measurements. New technological development is still needed to improve the capacity of these instruments to distinguishing different aerosol types even at low concentrations.

Chapter 5

Conclusions

During a field campaign performed within ACTRIS-2, optical properties and concentration of absorbing particles have been measured with different optical and thermo-optical techniques, at three sites in the Po Valley: Bologna, Monte Cimone and San Pietro Capofiume.

The absorption observations were carried out with two types of filter based instruments: Aethalometers (MAGEE Scientific models AE31 and AE33) that measure the attenuation coefficient, and a Multi Angle Absorption Photometer (MAAP) which directly derives the absorption coefficient by the simultaneous measurement of both scattered and transmitted light.

The various instruments have been compared and we derived the correction coefficients that allow to transform the attenuation values measured by the Aethalometers into absorption ones. The observed Aethalometer overestimation is in accordance with the multiple scattering effect described by Weingartner et al.; 2003, which is an apparent increase in absorption due to scattering by the filter fibers and/or non-absorbing particles here deposited, that increases the optical path of the beam. To correct this effect, a parameter C_0 was estimated as the ratio between the absorption values of the MAAP and the values of the Aethalometers already adjusted for the loading effect. Obtained values ranged between 2.8 and 4.3 in accordance with previous observations and the 3.5 recommended by GAW/WMO to convert the attenuation coefficients into absorption when only Aethalometer measurements are available. The variability of C_0 factor was site dependent: at Monte Cimone the C_0 factor was 2.9 ± 0.7 for AE31 and 2.8 ± 0.7 for AE33, with a very low variability (R^2 of scatter plot $= 0.95$ and 0.91, respectively). At San Pietro Capofiume the ratio between attenuation and absorption was characterized by higher spread (R^2 of scatter plot $= 0.62$ for AE31 and 0.7 for AE33), while the C_0 values were 3.2 ± 0.7 and 4.3 ± 1.1, respectively). In Bologna only AE31 and MAAP were used and a C_0 factor of 3.3 ± 0.8 was derived, with a R^2 of scatter plot of 0.86. The lower C_0 factor found in the mountain site can be linked with the aerosol aging time, in agreement with Weingartner et al. (2003). On the other hand, the enhancement in C_0 values due to condensation on the filter also described in Weingartner et al. (2003) is observed in particular in the two sites of the plain, where the atmosphere is richer of condensable species. The variability was affected both by influence of very low (high uncertainty) absorption values, as well as interference from moisture that increase the attenuation values but not the absorption measured by MAAP.

Once all the necessary corrections had been applied, the measurements made by the two models of Aethalometers were further compared with those of the MAAP for the 637 nm wavelength and with each other over the entire measured spectrum, to assess their comparability. At MC site, the absorption values calculated from Aethalometer attenuation are very close to the MAAP measurements, while in the case of SPC and BO, where there are limitations due to possible condensation of water vapor and other substances, the discrepancies are higher. Details of this variability should be further investigated also considering measure under controlled environmental conditions in order to identify the factors affecting the instrument uncertainties. The calculation of the absorption Ångstrom exponent (AAE), related to the BC source identification is then affected by a large uncertainty.

A general analysis of the monthly variability of the optical properties was carried out studying the overall behavior of the absorption, scattering coefficients and derived parameters, like single scattering albedo (SSA) and aerosol absorption (AAE) and scattering (SAE) Angstrom exponents. The highest values of both absorption and scattering coefficients are those measured in the urban site of Bologna, with a mean of 6.6 ± 0.9 Mm^{-1} and 23 ± 3 Mm^{-1}, respectively. This was due to the strong influence of many different anthropogenic local sources. San Pietro shows lower values of b_{abs} with respect to BO but not negligible amount of scattering particles (b_{abs} of 4.1 ± 0.6 Mm^{-1}, b_{sca} of 13.4 ± 1.6 Mm^{-1}), while the site of Monte Cimone shows the lowest values of absorption (2.0 ± 0.3 Mm^{-1}) and scattering coefficient (13.4 ± 1.6 Mm^{-1}). The mountain environment is thus characterized by a cleaner air than the plain, but can be subject to transport of pollutants in particular in the summer season. The mean values reported here are in accordance with those determined in other campaigns in the framework of ACTRIS for European urban, rural and mountain sites (Pandolfi et al., 2018; Zanatta et al. 2016).

Mean values of the single scattering albedo for BO, SPC e MC were respectively 0.77 ± 0.03, 0.74 ± 0.04 and 0.87 ± 0.03. The low values of BO and SPC reflect the influence of combustion sources in emission of aerosol population in Po Valley, while the higher values at MC indicate that aerosol reaching the mountain site is on average mixed with non absorbing component and secondary aerosols. The rural site of SPC, although it is far from sources such as traffic or household activities, well reflected in the concentrations, is characterized by the presence of similar SSA aerosol, and exposed to transport from nearby, highly polluted areas.

Typically, the daily cycle of of b_{abs}, b_{sca} and SSA, especially in a summer month such as July, is the result of the combination of the variability of the emission sources, linked to the daily and productive activities of humans and photo-chemical processes, and of the dynamic of air masses, mainly related to the height of the PBL and regional circulation. The absorption coefficient typical day shows a very similar behavior at the BO and SPC sites, with the main difference being less wide oscillations in the second. The rapid increase in the early morning is clearly linked with the rush hour of the morning traffic and it is weaker in SPC, because intense emissions are far from the site. A second less intense maximum is due to the evening traffic; than the values drop during the night reaching a minimum in the early morning. The scattering coefficient at BO and SPC sites, shows a similar trend but with a much lower or even absent peak in the evening and a less intense one that lasts longer in the morning. This behavior may be due to the production of secondary aersols, which have a more direct influence on the scattering component of the particulate matter and which are more effective during the day than during the evening, when the absence of sun prevents photochemical reactions. The SSA then shows two valleys at times when traffic pollution is highest so in the morning and in the evening, with that present at SPC during the evening probably so accentuated due to a combination of events on some days at that precise time. The diurnal variation at MC is very different from the previous ones, with low values in the morning and a maximum in the afternoon, both in terms of scattering and absorption. The main driver of diurnal cycle is the strong influence of valley winds transporting air from PBL, increasing the concentrations of pollutants in this site. Being a site at a very high altitude of 2175 m, it is generally above the upper limit of this layer and is therefore characterized by free tropospheric air masses.

An evaluation of the mass absorption cross-section (MAC) at 637 nm, i.e. a wavelength in which it is assumed that this is almost entirely due to the BC, and its variability at different sites was also provided, calculating this parameter from the ratio between the optically measured absorption coefficients by MAAP and mass of EC measured with the thermo-optical method (EUSAAR-II protocol). MAC is closely linked with aging and mixing state of the aerosol population. We found values of 9.2 ± 1.4 m^2/g in San Pietro and 9.4 ± 1.4 m^2/g in Bologna, higher than that considered by default in the instrument (6.6 m^2/g). The values calculated at BO and SPC are well comparable with the range typically observed for this quantity which is between 4.3 and 22.7 m^2/g. There seems to be no difference between the two sites and a value of about 9.3 can be considered as representative of the Po Valley background for the measurement period considered, at a wavelength of 637 nm.

Finally, the dependence of the scattering and absorption coefficients on the wavelength of the incident radiation was analyzed to obtain information on the particles source and size. The averaged value of the Absorption Angstrom Exponent (AAE) was shows very little variation at the different sites, suggesting a common source of BC and very limited influence of dust and/or absorbing OC: in BO it was 1.2 ± 0.6, at SPC 1.1 ± 0.6 and 1.1 ± 0.6 at MC, for AE31. The averaged value of SAE showed slightly larger variation: 1.9 ± 0.3 in BO, 1.5 ± 0.3 in SPC and 1.8 ± 0.3 at MC. These values indicates a dominance of scattering particles with high wavelength dependence and therefore small sizes. The entire region seems to be characterized mainly by small freshly emitted particles or non coated even in the free tropospheric, aged, aerosol. The AAE also remains pretty constant throughout the day, while SAE instead has different behavior in the three sites of Po Valley: it remains almost constant throughout the day at BO with a very slight increase around noon which could simply be associated with the progressive increase of secondary aerosol small particles produced throughout the morning. At MC the behavior reflects the increase in fine particles with the afternoon transport of pollutants from the plain. The SPC pattern shows a large decrease throughout the day that could be linked to the wind lifting from the soil of larger particles or the condensation of vapour that increases the size of the particles in agreement with Bucci et al., 2018.

Finally we want to underline the difficult conditions of such field campaign and difficulty of obtaining clear information, especially when present in low concentrations, the need of a perfect control of sample conditions (especially in term of drying) and the high uncertainties that characterize the Aethalometers measurements. New technological development is still needed to improve the capacity of these instruments to distinguish different aerosol types even at low concentrations

Nomenclature

- $\mathbf{b}_{abs}$ aerosol absorption coefficient (1/m)
- $\mathbf{b}_{scat}$ aerosol scattering coefficient (1/m)
- **SSA** ratio of light scattering to light extinction of aerosol particles collected on the filter
- **ATN** attenuation: attenuated fraction of light passing through a filter sample (transmittance measurement)
- **AAE** Absorption Angstrom Exponent
- **SAE** Scattering Angstrom Exponent
- **BC** Black Carbon
- **EC** Elemental Carbon
- **OC** Organic Carbon
- **MAC** Mass absorption cross section as ratio of aerosol absorption coefficient and EC mass concentration
- $\mathbf{b}_{ATN}$ attenuation coefficient
- $\mathbf{b}_{ATN}^{loading\ corrected}$ attenuation coefficient after the application of correction for loading effect
- $\mathbf{C}_0$ corrective parameter for Aethalometer
- $\mathbf{R}^2$ correlation coefficient
- **MC** Monte Cimone site
- **SPC** San Pietro Capofiume site
- **BO** Bologna site

Bibliography

[1] Kouji Adachi and Peter R. Buseck. 'Atmospheric tar balls from biomass burning in Mexico'. In: *Journal of Geophysical Research: Atmospheres* 116.D5 (2011).

[2] P. J. Adams, J. H. Seinfeld and D. M. Koch. 'Global concentrations of tropospheric sulfate, nitrate, and ammonium aerosol simulated in a general circulation model'. In: *J. Geophys. Res.* 104 (1999).

[3] T.L. Anderson et al. 'Performance Characteristics of a High-Sensitivity, Three-Wavelength, Total Scatter/Backscatter Nephelometer'. In: *Journal of Atmospheric and Oceanic Technology* 13.5 (1996), pp. 967–986.

[4] Theodore L. Anderson and John A. Ogren. 'Determining Aerosol Radiative Properties Using the TSI 3563 Integrating Nephelometer'. In: *Aerosol Science and Technology* (1998).

[5] M. O. Andreae and A. Gelencsér. 'Black carbon or brown carbon? The nature of light-absorbing carbonaceous aerosols'. In: *Atmospheric Chemistry and Physics* (2006).

[6] Meinrat O. Andreae and Paul J. Crutzen. 'Atmospheric Aerosols: Biogeochemical Sources and Role in Atmospheric Chemistry'. In: *Science* (1997).

[7] John Backman et al. 'On Aethalometer measurement uncertainties and an instrument correction factor for the Arctic'. In: *Atmospheric Measurement Techniques* (2017).

[8] Robert W. Bergstrom, Philip B. Russell and Phillip Hignett. 'Wavelength Dependence of the Absorption of Black Carbon Particles: Predictions and Results from the TARFOX Experiment and Implications for the Aerosol Single Scattering Albedo'. In: *Journal of the Atmospheric Sciences* 59.3 (2002), pp. 567–577.

[9] M. M. Bisiaux et al. 'Changes in black carbon deposition to Antarctica from two high-resolution ice core records, 1850 2000 AD'. In: *Atmospheric Chemistry and Physics* 12.9 (2012), pp. 4107–4115.

[10] M. M. Bisiaux et al. 'Variability of black carbon deposition to the East Antarctic Plateau, 1800 2000 AD'. In: *Atmospheric Chemistry and Physics* 12.8 (2012), pp. 3799–3808.

[11] F. Bohren and R. Huffman. 'Absorption and Scattering of Light by Small Particles'. In: *Absorption and Scattering of Light by Small Particles.* 1983.

[12] T. C. Bond et al. 'Bounding the role of black carbon in the climate system: A scientific assessment'. In: *Journal of Geophysical Research: Atmospheres banner* (2013).

[13] Tami C. Bond and Robert W. Bergstrom. 'Light Absorption by Carbonaceous Particles: An Investigative Review'. In: *Aerosol Science and Technology* (2006).

[14] Quentin Bourgeois and Isabelle Bey. 'Pollution transport efficiency toward the Arctic: Sensitivity to aerosol scavenging and source regions'. In: *Journal of Geophysical Research* 116 (2011).

[15] A. F. Bouwman, L. J. M. Boumans and N. H. Batjes. ‘Emissions of N2O and NO from fertilized fields: Summary of available measurement data’. In: *Global Biogeochemical Cycles* (2002).

[16] A. F. Bouwman et al. ‘A global high-resolution emission inventory for ammonia’. In: *Global Biogeochemical Cycles* (1997).

[17] P. Brimblecombe and C. Ogden. ‘AIR POLLUTION IN ART AND LITERATURE’. In: *Weather* 32.8 (1977), pp. 285–291.

[18] S. Bucci et al. ‘Vertical distribution of aerosol optical properties in the Po Valley during the 2012 summer campaigns’. In: *Atmospheric Chemistry and Physics* 18.8 (2018), pp. 5371–5389.

[19] Richard T. Burnett et al. ‘An Integrated Risk Function for Estimating the Global Burden of Disease Attributable to Ambient Fine Particulate Matter Exposure’. In: *Environmental Health Perspectives* 122.4 (2014), pp. 397–403.

[20] S C. Alfaro et al. ‘Iron oxides and light absorption by pure desert dust: An experimental study’. In: *Journal of Geophysical Research (Atmospheres)* 109 (2004).

[21] Christopher D. Cappa et al. ‘Radiative Absorption Enhancements Due to the Mixing State of Atmospheric Black Carbon’. In: *Science* 337.6098 (2012), pp. 1078–1081.

[22] F. Cavalli et al. ‘Toward a standardised thermal-optical protocol for measuring atmospheric organic and elemental carbon: the EUSAAR protocol’. In: *Atmospheric Measurement Techniques* 3.1 (2010), pp. 79–89.

[23] A. Cazorla et al. ‘Relating aerosol absorption due to soot, organic carbon, and dust to emission sources determined from in-situ chemical measurements’. In: *Atmospheric Chemistry and Physics* 13.18 (2013), pp. 9337–9350.

[24] Serena H. Chung and John H. Seinfeld. ‘Global distribution and climate forcing of carbonaceous aerosols’. In: *Journal of Geophysical Research: Atmospheres* 107 (2002).

[25] Serena Chung and JH Seinfeld. ‘Climate response of direct radiative forcing of anthropogenic black carbon’. In: *Journal of Geophysical Research-Atmospheres* 110 (2005).

[26] Petr Chylek and J. Wong. ‘Effect of absorbing aerosols on global radiation budget’. In: *Geophysical Research Letters* (1995).

[27] A. Clarke et al. ‘Biomass burning and pollution aerosol over North America: Organic components and their influence on spectral optical properties and humidification response’. In: *Journal of Geophysical Research: Atmospheres* 112.D12 (2007).

[28] James A. Coakley and Petr Chylek. ‘The Two-Stream Approximation in Radiative Transfer: Including the Angle of the Incident Radiation’. In: *Journal of the Atmospheric Sciences* 32.2 (1975), pp. 409–418.

[29] Aaron J Cohen et al. ‘Estimates and 25-year trends of the global burden of disease attributable to ambient air pollution: an analysis of data from the Global Burden of Diseases Study 2015’. In: *Lancet (London, England)* 389.10082 (2017), pp. 1907–1918.

[30] M. Collaud Coen et al. ‘Minimizing light absorption measurement artifacts of the Aethalometer: evaluation of five correction algorithms’. In: *Atmospheric Measurement Techniques* 3.2 (2010), pp. 457–474.

[31] J. Cozic et al. ‘Black carbon enrichment in atmospheric ice particle residuals observed in lower tropospheric mixed phase clouds’. In: *Journal of Geophysical Research: Atmospheres* 113.D15 (2008).

[32] P. Cristofanelli et al. 'Significant variations of trace gas composition and aerosol properties at Mt. Cimone during air mass transport from North Africa – contributions from wildfire emissions and mineral dust'. In: *Atmospheric Chemistry and Physics* 9.14 (2009), pp. 4603–4619.

[33] M. J. Cubison et al. 'The influence of chemical composition and mixing state of Los Angeles urban aerosol on CCN number and cloud properties'. In: *Atmospheric Chemistry and Physics* 8.18 (2008), pp. 5649–5667.

[34] F. Dahlkötter et al. 'The Pagami Creek smoke plume after long-range transport to the upper troposphere over Europe – aerosol properties and black carbon mixing state'. In: *Atmospheric Chemistry and Physics* 14.12 (2014), pp. 6111–6137.

[35] R. Duchi et al. *Summer report of the Italian Climate Observatory "O. Vittori" at Mt.Cimone – n.9.* Tech. rep. Institute of Atmospheric Science and Climate – National Research Council of Italy, 2015.

[36] Feingold and Graham. 'Modeling of the first indirect effect: Analysis of measurement requirements'. In: *Geophysical Research Letters* (2003).

[37] P. Forster et al. 'Changes in atmospheric constituents and in radiative forcing'. In: *Climate Change 2007 : The Physical Science Basis : Contribution of Working Group I to the Fourth Assessment Report of the Intergovernmental Panel on Climate Change.* Ed. by Susan Solomon et al. Cambridge; New York: Cambridge University Press, 2007. Chap. 2, pp. 129–234.

[38] J Genberg et al. 'Light absorbing carbon in Europe – measurement and modelling, with a focus on residential wood combustion emissions'. In: *Atmospheric Chemistry and Physics Discussions* 13 (2013), pp. 9051–9105.

[39] A. Hamed et al. 'Nucleation and growth of new particles in Po Valley, Italy'. In: *Atmospheric Chemistry and Physics* 7.2 (2007), pp. 355–376.

[40] G. Hänel. 'Optical properties of atmospheric particles: Complete parameter sets obtained through polar photometry and an improved inversion technique.' In: *Applied Optics* (1994).

[41] J. Hansen and L. Nazarenko. 'Soot climate forcing via snow and ice albedos'. In: *Proc. Natl. Acad. Sci.* (2004).

[42] J. Hansen, M. Sato and R. Ruedy. 'Radiative forcing and climate response'. In: *J. Geophys. Res.* (1997).

[43] J. M. Haywood and K. P. Shine. 'The effect of anthropogenic sulfate and soot aerosol on the clear sky planetary radiation budget'. In: *Geophysical Research Letters* 22.5 (1995), pp. 603–606.

[44] Jost Heintzenberg and R. J. Charlson. 'Design and Applications of the Integrating Nephelometer: A Review'. In: *Journal of Atmospheric and Oceanic Technology* (1996).

[45] Mark Z. Jacobson and Yoram J. Kaufman. 'Wind reduction by aerosol particles'. In: *Geophysical Research Letters* 33.24 (2006).

[46] N. A. Janssen et al. *Health effects of black carbon.* Tech. rep. World Health Organization, 2012.

[47] H. John Seinfeld and N. Spyros Pandis. *Atmospheric chemistry and physics, From Air Pollution to Climate Change.* JOHN WILEY and SONS, INC., 2006.

[48] A. Karanasiou et al. 'Thermal-optical analysis for the measurement of elemental carbon (EC) and organic carbon (OC) in ambient air a literature review'. In: *Atmos. Meas. Tech. Discuss.* (2015).

[49] Thomas W. Kirchstetter, T. Novakov and Peter V. Hobbs. ‘Evidence that the spectral dependence of light absorption by aerosols is affected by organic carbon’. In: *Journal of Geophysical Research: Atmospheres* 109.D21 (2004).

[50] A. Knox et al. ‘Mass Absorption Cross-Section of Ambient Black Carbon Aerosol in Relation to Chemical Age’. In: *Aerosol Science and Technology* 43.6 (2009), pp. 522–532.

[51] D. Koch and A.D. Del Genio. ‘Black carbon absorption effects on cloud cover: Review and synthesis’. In: *Atmos. Chem. Phys.* (2010).

[52] D. A. Lack and C. D. Cappa. ‘Impact of brown and clear carbon on light absorption enhancement, single scatter albedo and absorption wavelength dependence of black carbon’. In: *Atmospheric Chemistry and Physics* 10.9 (2010), pp. 4207–4220.

[53] D. A. Lack and J. M. Langridge. ‘On the attribution of black and brown carbon light absorption using the exponent’. In: *Atmospheric Chemistry and Physics* 13.20 (2013), pp. 10535–10543.

[54] J.-F. Lamarque et al. ‘Historical (1850-2000) gridded anthropogenic and biomass burning emissions of reactive gases and aerosols: Methodology and application’. In: *Atmos. Chem. Phys.* 10 (2010), pp. 7017–7039.

[55] J. Lelieveld et al. ‘The contribution of outdoor air pollution sources to premature mortality on a global scale’. In: *Nature* (2015).

[56] Kristin Lewis et al. ‘Strong spectral variation of biomass smoke light absorption and single scattering albedo observed with a novel dual-wavelength photoacoustic instrument’. In: *Journal of Geophysical Research* 113 (2008).

[57] V M. H. Lavanchy et al. ‘Historical record of carbonaceous particle concentrations from a European high-alpine glacier (Colle Gnifetti, Switzerland)’. In: *Journal of Geophysical Research* 1042 (1999), pp. 21227–21236.

[58] CA Magee Scientific Company Berkeley, ed. *The Aethalometer*. 2005.

[59] Natalie Mahowald et al. ‘Aerosol Impacts on Climate and Biogeochemistry’. In: *Annual Review of Environment and Resources* (2011).

[60] A. Marinoni et al. ‘Continuous measurements of aerosol physical parameters at the Mt. Cimone GAW Station (2165 m asl, Italy)’. In: *Science of The Total Environment* 391 (2008), pp. 241–251. ISSN: 0048-9697.

[61] C. A. Masiello et al. ‘Weathering controls on mechanisms of carbon storage in grassland soils’. In: *Global Biogeochemical Cycles* 18.4 (2004).

[62] Joseph R. McConnell et al. ‘20th-Century Industrial Black Carbon Emissions Altered Arctic Climate Forcing’. In: *Science* 317.5843 (2007), pp. 1381–1384.

[63] H.A. Michelsen et al. ‘Laser-induced incandescence: Particulate diagnostics for combustion, atmospheric, and industrial applications’. In: *Progress in Energy and Combustion Science* 51 (2015), pp. 2–48.

[64] Jing Ming et al. ‘Black Carbon (BC) in the snow of glaciers in west China and its potential effects on albedos’. In: *Atmospheric Research* 92 (2009).

[65] *Model 3550/3560 Series Integrating Nephelometer Instruction Manual*. TSI Incorporated, 2001.

[66] *Model 5012 Multi Angle Absorption Photometer (MAAP), Instructional Manual*. Thermo Electron Corporation, 2003.

[67] H. Moosmüller, R.K. Chakrabarty and W.P. Arnott. ‘Aerosol light absorption and its measurement: A review’. In: *Journal of Quantitative Spectroscopy and Radiative Transfer* 110.11 (2009), pp. 844–878.

[68] Nobuhiro Moteki and Yutaka Kondo. ‘Dependence of Laser-Induced Incandescence on Physical Properties of Black Carbon Aerosols: Measurements and Theoretical Interpretation’. In: *Aerosol Science and Technology* 44.8 (2010), pp. 663–675.

[69] T. Müller et al. ‘Characterization and intercomparison of aerosol absorption photometers: result of two intercomparison workshops’. In: *Atmospheric Measurement Techniques* 4.2 (2011), pp. 245–268.

[70] G. Myhre et al. ‘Radiative forcing of the direct aerosol effect from AeroCom Phase II simulations’. In: *Atmos. Chem. Phys.* (2013).

[71] G. Myhre et al. ‘Aerosols and their Relation to Global Climate and Climate Sensitivity’. In: *Nature Education Knowledge* (2013).

[72] T Nakayama et al. ‘Size-dependent correction factors for absorption measurements using filter-based photometers: PSAP and COSMOS’. In: *Journal of Aerosol Science* 41 (Apr. 2010), pp. 333–343.

[73] Tica Novakov and Hal Rosen. *The Black Carbon Story: Early History and New Perspectives.* Tech. rep. The Royal Swedish Academy of Science, 2013.

[74] T. B. Onasch et al. ‘Soot Particle Aerosol Mass Spectrometer: Development, Validation, and Initial Application’. In: *Aerosol Science and Technology* 46.7 (2012), pp. 804–817.

[75] World Health Organization. *Ambient air pollution: A global assessment of exposure and burden of disease.* Tech. rep. World Health Organization, 2016.

[76] Marco Pandolfi et al. ‘A European aerosol phenomenology - 6: Scattering properties of atmospheric aerosol particles from 28 ACTRIS sites’. In: *Atmospheric Chemistry and Physics* (2018).

[77] M.D. Petters and S. M. Kreidenweis. ‘A single parameter representation of hygroscopic growth and cloud condensation nucleus activity’. In: *Atmospheric Chemistry and Physics* (2007).

[78] Andreas Petzold and Markus Schonlinner. ‘Multi-angle absorption photometry—a new method for the measurement of aerosol light absorption and atmospheric black carbon’. In: *Journal of Aerosol Science* (2003).

[79] V Ramanathan and Gregory Carmichael. ‘Global and Regional Climate Changes Due to Black Carbon’. In: *Nat Geosci* 1 (2008).

[80] Jenny Rissler et al. ‘Physical properties of the sub-micrometer aerosol over the Amazon rain forest during the wet-to-dry season transition - comparison of modeled and measured CCN concentrations’. In: *Atmospheric Chemistry and Physics* (2004).

[81] H. Rosen et al. ‘Identification of the optically absorbing component in urban aerosols’. In: *Appl. Opt.* 17.24 (1978), pp. 3859–3861.

[82] M. Schnaiter et al. ‘UV-VIS-NIR spectral optical properties of soot and soot-containing aerosols’. In: *Journal of Aerosol Science* (2003).

[83] Magee Scientific. *Aethalometer Model AE33, User Manual.* Ed. by Aerosol d.o.o. 2016.

[84] Arthur J. Sedlacek et al. ‘Determination of and evidence for non-core-shell structure of particles containing black carbon using the Single-Particle Soot Photometer (SP2)’. In: *Geophysical Research Letters* 39.6 (2012).

[85] Manabu Shiraiwa et al. ‘Aerosol Health Effects from Molecular to Global Scales’. In: *Environmental Science & Technology* (2017).

[86] Jay G. Slowik et al. ‘An Inter-Comparison of Instruments Measuring Black Carbon Content of Soot Particles’. In: *Aerosol Science and Technology* 41.3 (2007), pp. 295–314.

[87] S. J. Smith and T. C. Bond. 'Two hundred fifty years of aerosols and climate: the end of the age of aerosols'. In: *Atmospheric Chemistry and Physics* 14.2 (2014), pp. 537–549.

[88] S. Solomon et al. *IPCC, 2007: Climate Change 2007: The Physical Science Basis.* Tech. rep. Cambridge University Press, 2007.

[89] Michelle Stephens, Nelson Turner and Jon Sandberg. 'Particle Identification by Laser-Induced Incandescence in a Solid-State Laser Cavity'. In: *Applied optics* 42 (2003), pp. 3726–36.

[90] P. Stier et al. 'The evolution of the global aerosol system in a transient climate simulation from 1860 to 2100'. In: *Atmospheric Chemistry and Physics* 6.10 (2006), pp. 3059–3076.

[91] T.F. Stocker et al. *IPCC, 2013: Climate Change 2013: The Physical Science Basis.* Tech. rep. Cambridge University Press, Cambridge, 2013.

[92] A. Stohl et al. 'Technical note: The Lagrangian particle dispersion model FLEXPART version 6.2'. In: *Atmospheric Chemistry and Physics* 5.9 (2005), pp. 2461–2474.

[93] Haolin Sun, Laura Biedermann and Tami C. Bond. 'Color of brown carbon: A model for ultraviolet and visible light absorption by organic carbon aerosol'. In: *Geophysical Research Letters* 34.17 (2007).

[94] I. Tegen and I. Fung. 'Modeling of mineral dust transport in the atmosphere: Sources, transport, and optical thickness'. In: *J. Geophys. Res.* 99 (1994), pp. 22897–22914.

[95] S. Twomey. 'The influence of pollution on the short wave albedo of clouds'. In: *J. Atmos. Sci.* 34 (1977), pp. 1149–1152.

[96] E. Weingartner et al. 'Absorption of light by soot particles: determination of the absorption coefficient by means of aethalometers'. In: *Journal of Aerosol Science* (2003).

[97] Ernest Weingartner et al. 'Aerosol emission in a road tunnel'. In: *Atmospheric Environment* 31 (1997), pp. 451–462.

[98] M. Yang et al. 'Attribution of aerosol light absorption to black carbon, brown carbon, and dust in China: interpretations of atmospheric measurements during EAST-AIRE'. In: *Atmospheric Chemistry and Physics* 9.6 (2009), pp. 2035–2050.

[99] M. Zanatta et al. 'A European aerosol phenomenology-5: Climatology of black carbon optical properties at 9 regional background sites across Europe'. In: *Atmospheric Environment* 145 (2016), pp. 346–364. ISSN: 1352-2310.